
Electronic Thesis and Dissertation Repository

12-10-2020 3:00 PM

Fabricating $\text{Cu}_2\text{ZnSnS}_4$, $\text{Cu}_2\text{ZnSn}(\text{S,Se})_4$ and $\text{CuIn}(\text{S,Se})_2$ light-absorbing thin films for low-cost solar devices.


Vaishnavi Raja, *The University of Western Ontario*

Supervisor: Ding, Zhifeng, *The University of Western Ontario*

A thesis submitted in partial fulfillment of the requirements for the Master of Science degree in Chemistry

© Vaishnavi Raja 2020

Follow this and additional works at: <https://ir.lib.uwo.ca/etd>

 Part of the [Analytical Chemistry Commons](#), [Materials Chemistry Commons](#), and the [Physical Chemistry Commons](#)

Recommended Citation

Raja, Vaishnavi, "Fabricating $\text{Cu}_2\text{ZnSnS}_4$, $\text{Cu}_2\text{ZnSn}(\text{S,Se})_4$ and $\text{CuIn}(\text{S,Se})_2$ light-absorbing thin films for low-cost solar devices." (2020). *Electronic Thesis and Dissertation Repository*. 7505.
<https://ir.lib.uwo.ca/etd/7505>

This Dissertation/Thesis is brought to you for free and open access by Scholarship@Western. It has been accepted for inclusion in Electronic Thesis and Dissertation Repository by an authorized administrator of Scholarship@Western. For more information, please contact wlsadmin@uwo.ca.

Abstract

In this thesis, $\text{Cu}_2\text{ZnSnS}_4$ (CZTS), $\text{Cu}_2\text{ZnSn}(\text{S},\text{Se})_4$ (CZTSSe) and $\text{CuIn}(\text{S},\text{Se})_2$ (CISSe) thin-films have been optimized to use as the key light-absorbing and conversion layer for solar cells. CZTS nanocrystals (NCs) were solvothermally synthesized, etched with acetic acid and structurally analyzed using synchrotron spectroscopy. Electrodeposited CZTSSe films showed a non-ideal increase in sulfur with lower selenization temperature and post-process etching. Compositional studies of electrodeposited CISSe films confirmed the decrease in selenium after the acetic acid etching. Through PECMs and other conventional characterization techniques, it was determined that non-etched CZTSSe and CISSe solar devices performed better than their etched counterparts, achieving efficiencies of 5.3% and 2.1%, respectively. In contrast, the results of the CZTS NCs achieved a higher efficiency for the etched device at 6.5%. In the end, electrodeposition proved to be a cheaper, more replicable technique, while CZTSSe demonstrated to be the most cost-effective light-absorber-layer for efficient solar cells.

Keywords

Photovoltaics, Solar cells, thin-films, light-absorber-layer, $\text{Cu}_2\text{ZnSnS}_4$ (CZTS), $\text{Cu}_2\text{ZnSn}(\text{S},\text{Se})_4$ (CZTSSe), $\text{CuIn}(\text{S},\text{Se})_2$ (CISSe), nanocrystals (NCs), electrodeposition, solvothermal synthesis, Photoelectrochemical measurements (PECMs), X-ray Absorption Fine Structure (XAFS), photovoltaic efficiency, heterojunction/ p-n junction, photoelectrochemistry

Summary for Lay Audience

Solar energy presents itself as an optimistic renewable source to meet increasing global energy demands. Sunlight is one of the cleanest and most abundant sources of energy available and can be harvested into thermal or electrical energy. The most common technology to convert the light into electricity are silicon-intensive photovoltaic (PV) devices. As a result, PV alternatives with lower material costs are being pursued.

Research has been devoted to developing thin-film solar cells to reduce manufacturing costs as they need less material. This type of device typically focuses on and employs *p*-type semiconducting materials to act as the light-absorbing and conversion layer. Nonetheless, thin-film solar cells are not yet widely commercialized due to their low power efficiencies and use of rare and expensive elements. The three light-absorbing layers that were studied in this thesis are $\text{Cu}_2\text{ZnSnS}_4$ (CZTS), $\text{Cu}_2\text{ZnSn}(\text{S},\text{Se})_4$ (CZTSSe) and $\text{CuIn}(\text{S},\text{Se})_2$ (CISSe) as they consist of earth-abundant elements.

On all light-absorber-layers, post process etching with acetic acid was employed and its effects were studied by photoelectrochemical measurements (PECMs). This technique involves a three-electrode electrochemical cell and an oxidizing agent in solution. The charge transfer from the film to the solution, upon illumination of the cell, defines the quality and performance of the film. Post-process etching has been shown to improve film performance and device efficiency as it removes surface impurities that inhibit current. Yet this was only true for the films comprised of CZTS nanocrystals (NCs).

In order to improve film reproducibility and lower production costs, electrodeposition was used to fabricate the light-absorber-layers. Selenium was introduced into the CZTSSe and CISSe films in hopes to further enhance the photoresponse. Using conventional techniques along with synchrotron spectroscopy, all three materials were characterized before and after etching to determine how this post-process structurally affected the film and why only some materials reap the benefits. This thesis is split into three parts, one for each of the light-absorbing layers studied. Full solar cells are fabricated and resulting device efficiencies are compared to determine the most cost-effective light-absorber-layer for future focus.

Acknowledgments

Firstly, I would like to thank my supervisor Dr. Zhifeng Ding for all his guidance, patience and support during my two years at Western. He has given me many opportunities to explore new and exciting techniques in pursuit of my ideas. I am grateful to have been part of his research group and will remember the experiences he has provided me throughout my research.

I appreciate all the facilities at which I have had opportunities and would like to express my gratitude to the staff at the Chemistry Electronic Shop and the X-ray Diffraction Facility. Special thanks to Aneta Borecki and Vinicius Martins dos Santos for running my XRD samples and taking the time to help me with the data.

My sincerest gratitude to the members of the Ding group for all their support and fun times. I would like to thank Dr. Mahdi Hesari, Jonathan Adsetts, Kenneth Chu, Brandon Yang and Jonathan Wong. In addition, I would like to especially thank Dr. Matthew Turnbull for guiding me through the start of this project and assisting me with the XAFS data. A big shout out to the members of the Lagugné-Labarthe group as well for their antics.

I need to thank my best friends, specifically Katilin McNeil and Yoojin Ro, who have been especially by my side since the pandemic began. Without them, working at home would have been a challenge. I always enjoy our morning routines and I thank you both for keeping me focused all this time.

Finally, I am grateful for my parents as they have given me guidance and support, not only during my master's but throughout my life. I could not have done this without their patience and belief in me.

Table of Contents

Abstract.....	ii
Summary for Lay Audience.....	iii
Acknowledgments.....	iv
Table of Contents.....	v
List of Tables.....	ix
List of Figures.....	xi
List of Abbreviations, Symbols and Nomenclature.....	xv
Chapter 1.....	1
1 Introduction.....	1
1.1 General Introduction.....	1
1.2 Principles behind photovoltaics.....	3
1.3 Thin film photovoltaics.....	5
1.3.1 CZTS & CZTSe.....	7
1.3.2 CIS & CISE.....	7
1.4 Characterization methods.....	8
1.4.1 Scanning electron microscopy & Energy-dispersive x-ray spectroscopy...	9
1.4.2 X-ray diffraction.....	9
1.4.3 X-ray photoelectron spectroscopy.....	9
1.4.4 Synchrotron based x-ray absorption spectroscopy.....	10
1.4.5 UV-VIS absorption spectroscopy.....	11
1.4.6 Photoelectrochemical measurements.....	12
1.4.7 Current – voltage measurements.....	13

1.5 Scope of thesis	14
1.6 References.....	15
Chapter 2.....	19
2 Fabrication and optimization of $\text{Cu}_2\text{ZnSnS}_4$ for low-cost solar devices.....	19
2.1 Introduction.....	19
2.2 Experimental.....	19
2.2.1 Nanocrystal layer fabrication.....	22
2.2.2 Buffer layer and full device fabrication.....	22
2.2.3 Characterization.....	23
2.2.4 Layer-by-layer fabrication.....	25
2.3 Results and Discussion.....	26
2.3.1 Photoelectrochemical measurements of CZTS NCs.....	26
2.3.2 X-ray absorption fine structure (XAFS).....	29
2.3.3 Energy band gap analysis.....	34
2.3.4 Synchrotron XPS of the CZTS/CdS interface.....	34
2.3.5 Formation of the P-N junction.....	40
2.3.6 Full device analysis.....	43
2.3.7 Characterization of ED CZTS layers.....	47
2.4 Conclusions.....	50
2.5 References.....	51
Chapter 3.....	56
3 Effect of selenium incorporation on the photoelectrochemical behavior of $\text{Cu}_2\text{ZnSn}(\text{S},\text{Se})_4$ films and their solar devices.....	56
3.1 Introduction.....	56

3.2	Experimental	58
3.2.1	Fabrication from absorber layer to full device.....	58
3.2.2	Characterization	60
3.3	Results and Discussion	61
3.3.1	Development of selenization criterion	61
3.3.2	Structural analysis via x-ray diffraction.....	68
3.3.3	Composition and morphology.....	77
3.3.4	Band gap energy analysis.....	79
3.3.5	Inclusion of buffer layer and full device analysis.....	80
3.4	Conclusions.....	85
3.5	References.....	85
Chapter 4	90
4	Fabricating and characterizing electrodeposited $\text{CuIn}(\text{S},\text{Se})_2$ thin film solar cells.....	90
4.1	Introduction.....	90
4.2	Experimental	92
4.2.1	Sequential electrodeposition, selenization & fabrication of full devices..	92
4.2.2	Characterization	93
4.3	Results and Discussion	94
4.3.1	Refining conditions for selenization via PECMs.....	94
4.3.2	Structure of CISE film via x-ray diffraction.....	99
4.3.3	Composition and morphology via SEM/EDX	105
4.3.4	Band gap energy analysis.....	107
4.3.5	Full device completion and analysis.....	108
4.4	Conclusions.....	112

4.5 References.....	113
Chapter 5.....	118
5 Concluding remarks and future work.....	118
5.1 Concluding remarks	118
5.2 Future work.....	121
5.3 References.....	123
Curriculum Vitae	125

List of Tables

Table 2.1: EXAFS fitting parameters for each sample metal center. Each bond length has an error of less than $\pm 0.02 \text{ \AA}$ and are consistent within the non-etched or etched sample category. Energy shifts (E_0) were held constant for all scattering paths and were less than 2.7 eV in all cases. The amplitude reduction factor was fixed at 0.70 for the Cu K-edge, 0.90 for the Zn K-edge, and 1.00 for the Sn K-edge EXAFS fitting, with each determined by measuring the metal reference foil and fitting the metal-metal bond distance. N is the degeneracy of the pathway, σ^2 is the mean squared displacement of half the path-length and r is the interatomic distance. 32

Table 2.2: Time study of the effect of prolonged atmospheric exposure time on the CZTS film along with the effect of etching with acetic acid. The rows of exposure time and etching processes are in chronological order and thus, the total exposure time of the films is two months. Atomic percentages of elements are listed with the primary focus being on the Cu 2p, Zn 2p, Sn 3d and O 1s..... 39

Table 2.3: Range of characteristic parameters of J-V curves, measured over ten full devices for non-etched CZTS NCs and etched CZTS NCs..... 46

Table 3.1: Range of photocurrent achieved in a PECM as a function of selenization temperature. 63

Table 3.2: Summary of maximum photocurrent achieved for each selenium concentration for both NE and E films..... 67

Table 3.3: XRD parameters evaluated for electrodeposited CZTSe Samples 1-4 through the (112) reflection for different selenization temperatures where standard CZTSe (112) peak is 27.16° 73

Table 3.4: Experimental lattice constants compared to standards 77

Table 3.5: Elemental ratios determined through EDX for both NE and E circumstances..... 79

Table 3.6: Range of characteristic J-V curve parameters, measured over ten working devices for non-etched CZTSSe and etched CZTSSe. 83

Table 4.1: Range of photocurrent as a function of selenization temperature determined by PECMs in Figure 4.1.....	96
Table 4.2: XRD parameters for Samples 5 – 8 through the (112) reflection peak for various selenization temperatures where the standard (112) peak for CISE is at 26.67°.....	102
Table 4.3: Chalcopyrite lattice constants for standard CIS, CISE and experimental CISSe films in both E and NE scenarios.....	104
Table 4.4: Relative molar ratios of NE and E CISSe films measured by EDX.....	106
Table 4.5: Measurement statistics of J-V curve parameters for ten working devices of both non-etched CISSe and etched CISSe.	111

List of Figures

Figure 1.1: A schematic of a p-n junction and the SCR after equilibrium is reached. Light exposure produces an e-h pair (in red).....	4
Figure 1.2: Energy band diagrams of a) an <i>intrinsic</i> semiconductor, b) an <i>n</i> -type semiconductor and c) a <i>p</i> -type semiconductor, where E_F is the Fermi level energy.....	5
Figure 1.3: Best solar cell efficiencies involving thin-film technologies as of 2020. ¹⁵	6
Figure 1.4: Schematic of a fabricated thin film solar cell.....	7
Figure 1.5: Schematic of a typical XAFS spectrum with the XANES and EXAFS region specified. ⁴⁵	11
Figure 2.1: PECMs of non-etched CZTS NC films a) before and b) after CdS coating as well as etched CZTS NC films c) before and d) after CBD of CdS. Etching was processed using glacial acetic acid for 30 min.....	27
Figure 2.2: Cu, Zn, and Sn K-edge XAFS – a), b), and c), respectively – comparing the primary oxidation state and coordination sphere of the etched and non-etched CZTS NCs. Insets of the white line peak are shown for clarity. The corresponding EXAFS fitting– for Cu (d), Zn (e), and Sn (f) displays the structural shifts in bond lengths of the nearest neighbor, and the relative disorder within the NCs.	30
Figure 2.3: Tauc plots of the UV-VIS absorbance showing the optical band gap for the etched, non-etched CZTS NC film as well as the CdS layer.	35
Figure 2.4: XPS plots of the valence band energy for the non-etched CZTS (a), etched CZTS (b), bulk CdS (c), non-etched CZTS NC/CdS interface (d) and the etched CZTS NC/CdS interface (e). Linear extrapolation of the leading edge marks the E_{VB}	37
Figure 2.5: Energy band diagram for the a) etched and b) non-etched CZTS-CdS interface; the relative fermi level has been marked as E_F . Both configurations resemble a spike-like barrier at the interface.....	41

Figure 2.6: J-V curve for a champion full device of a) an etched film and b) non-etched film. The current and voltage at maximum power are indicated by the dashed lines used to calculate Fill Factor.....	45
Figure 2.7: Efficiency histograms for: a) NE CZTS NCs and b) E CZTS NCs.	46
Figure 2.8: PECMs of non-etched ED CZTS films a) before and b) after CdS coating as well as etched ED CZTS films c) before and d) after CBD of CdS. Etching was processed using glacial acetic acid for 30 min.	48
Figure 3.1: Photoelectrochemical measurements of CZTSe films fabricated with 10 mg/cm ² of selenium at selenization temperatures of a) 400 °C, b) 450 °C, c) 500 °C and d) 525 °C.	62
Figure 3.2: PECMs showcasing films with various selenium concentrations, all selenized at 500 °C. a) NE scenario with 3, 5, & 10 mg/cm ² selenium and b) E scenario with 3, 5 & 10 mg/cm ² of selenium.	66
Figure 3.3: XRD diffractograms for Samples 1-4 of CZTSSe. Resulting secondary phases and defects are summarized in the legend within the figure.	70
Figure 3.4: XRD diffractograms for Samples 1-4 centered at a) (112) reflection kesterite peak ranging from 26.5° – 28.8°, b) (220/204) reflection kesterite peak ranging from 44.5° – 48.0° and c) (312/116) reflection kesterite peak ranging from 53.5° – 57.0°. The dashed lines in each figure represent the standard CZTSe and CZTS peaks.....	70
Figure 3.5: XRD diffractograms for CZTSSe in both NE and E scenarios. The blue and red dashed lines represent the standard CZTSe and CZTS peaks respectively. The secondary phases present are labeled in the legend while the three major crystallographic peaks are labeled on the standard CZTS spectrum.	75
Figure 3.6: Crystal structures for: a) standard CZTS, b) standard CZTSe and c) an estimate of CZTSSe with 12.5% sulfur incorporation.	76
Figure 3.7: Surface morphology of a) a NE and b) an E CZTSSe film. In each figure, the larger image has a scale of 50 μm while the inset has a scale of 10 μm.....	78

Figure 3.8: Tauc plot of an UV-VIS absorbance measurement. Linear extrapolation to the photon energy illustrates the band gap energy of NE CZTSSe.	80
Figure 3.9: PECMs of NE CZTSSe with and without the inclusion of the CdS buffer layer.	81
Figure 3.10: J-V curve for champion full devices of a) a NE CZTSSe film and b) an E CZTSSe film. The voltage and current density at maximum power, indicated by the dashed lines highlighted in green, are used to calculate the Fill Factor (FF).	82
Figure 3.11: Device efficiency histograms for: a) NE CZTSSe and b) E CZTSSe.	84
Figure 4.1: Photoelectrochemical measurements for CISE films fabricated with 5 mg/cm ² of selenium at selenization temperatures of a) 400 °C, b) 450 °C, c) 500 °C and d) 525 °C.	95
Figure 4.2: Photoelectrochemical measurements of CISE films fabricated with 5 mg/cm ² selenium at 500 °C in E and NE scenarios.	98
Figure 4.3: XRD diffractograms for CISE Samples 5 – 8. The three most characteristic peaks are labeled with a colour legend included within the figure. Red dashed lines indicate standard peaks for CISE and black dashed lines indicate standard peaks for CIS.	100
Figure 4.4: XRD diffractograms for CISSe in both NE and E scenarios. The red and black dashed lines represent the standard CISE and CIS peaks, respectively, while the three major crystallographic peaks are labeled.	103
Figure 4.5: Crystal structures for: a) standard CIS, b) standard CISE and c) an estimate of CISSe with 12.5% sulfur incorporation.	104
Figure 4.6: Surface SEM images of a) a NE and b) an E CISSe film. The larger image has a scale of 50 μm whereas the inset has a scale of 10 μm.	106
Figure 4.7: Tauc plot of the UV-VIS absorbance measurement showing the band gap for NE CISSe.	108
Figure 4.8: PECMs of NE CISSe with and without the addition of the CdS layer.	109

Figure 4.9: J-V curve of the a) champion NE CISSe full device and b) champion E CISSe full device. The current density and voltage at maximum power are indicated by the green dashed lines used to calculate the Fill Factor..... 110

Figure 4.10: Final device efficiency histograms of: a) NE CISSe and b) E CISSe..... 111

Figure 5.1: Range of device efficiencies of CZTS, CZTSSe and CISSe as a function of open-circuit potential in a) ten non-etched devices and b) ten etched devices. 120

Figure 5.2: PECMs of electrodeposited selenium on Mo-coated glass at various deposition potentials. Each deposition was held for 20 seconds..... 122

List of Abbreviations, Symbols and Nomenclature

α	Absorption coefficient
θ	Bragg diffraction angle
δ	Dislocation density
β	Full Width Half Maximum
ε	Lattice strain
σ^2	Mean squared displacement of half the path-length, in angstroms
$h\nu$	Photon energy
η	Power conversion efficiency
λ	Wavelength
ϕ	Work function
a	Lattice parameter a
A	Absorber layer
\AA	Angstrom
Ag/AgCl	Silver/silver chloride
ALD	Atomic Layer Deposition
AM 1	Air Mass 1
AM 1.5	Air Mass 1.5
APS	Advanced Photon Source
a.u.	Arbitrary units

AZO	Aluminum doped Zinc Oxide
b	Lattice parameter b
c	Lattice parameter c
CB	Conduction Band
CBD	Chemical Bath Deposition
CBO	Conduction Band Offset
CdS	Cadmium Sulfide
CIGS	$\text{Cu}(\text{In}_x\text{Ga}_{1-x})\text{S}(\text{e})_2$
CIS	CuInS
CISE	CuInSe_2
CISSe	$\text{CuIn}(\text{S},\text{Se})_2$
CZTS	$\text{Cu}_2\text{ZnSnS}_4$
CZTSe	$\text{Cu}_2\text{ZnSnSe}_4$
CZTSSe	$\text{Cu}_2\text{ZnSn}(\text{S},\text{Se})_4$
D	Crystallite/grain size
E	Etched
EB_{CB}	Energy difference between conduction bands
EB_{VB}	Energy difference between valence bands
E_{CB}	Energy from the fermi level energy to the conduction band
EDX	Energy Dispersive X-ray Spectroscopy

E_F	Fermi level energy
E_g	Band gap energy
$e - h$	Electron – hole
EPD	Electrophoretic deposition
ED	Electrodeposition/electrochemical deposition
eV	Electron Volt
E_{VB}	Energy gap between valence band and fermi level energy
EXAFS	Extended X-ray Absorption Fine Structure
FF	Fill Factor
FWHM	Full Width Half Maximum
H_2S	Hydrogen sulfide
ICDD	International Centre for Diffraction Data
I_{MP}	Current at maximum power
I_{SC}	Short circuit current
JCPDS	Joint Committee on Powder Diffraction Standards
J-V	Current density – voltage
KCl	Potassium chloride
KCN	Potassium cyanide
k_d	Rate of decay
k_{ET}	Rate of electron transfer

k_{PS}	Rate of product separation
k_R	Rate of recombination
KWh	Kilowatt hours
Mo	Molybdenum
MPP	2-mercapto-5-n-propylpyrimidine
MV^{2+}/MV^+	Methyl Viologen
N	Degeneracy of path
NC(s)	Nanocrystal(s)
NE	Non-Etched
<i>n</i> -type	Electron-rich semiconductor
PECM(s)	Photoelectrochemical measurement(s)
P_{max}	Maximum power
<i>p</i> -type	Electron-poor semiconductor
PV	Photovoltaic
<i>r</i>	Interatomic distance, in angstroms
SCE	Saturated Calomel Electrode
SCR	Space Charge Region
SEM	Scanning Electron Microscopy
SLG	Soda Lime Glass
SR	Synchrotron Radiation

TWh	Terawatt hours
UV-VIS	Ultraviolet -Visible
VB	Valence Band
VESTA	Visualization for Electronic and Structural Analysis
V_{MP}	Potential at maximum power
V_{OC}	Open circuit potential
XAFS	X-ray Absorption Fine Structure
XANES	X-ray Absorption Near Edge Structure
XAS	X-ray Absorption Spectroscopy
XPS	X-ray Photoelectron Spectroscopy
XRD	X-ray Diffraction
ZnO	Zinc Oxide

Chapter 1

1 Introduction

Solar energy is one of the most promising renewable energy sources however the challenge lies in harvesting it efficiently with low-cost methods. Thin film solar cells have been employed as way to reduce manufacturing costs of solar devices. However, the most important layer in the device, the light-absorber-layer, has typically involved the use of rare and expensive elements. This thesis will focus on addressing these challenges by exploring three alternative light-absorber-layers: $\text{Cu}_2\text{ZnSnS}_4$ (CZTS), $\text{Cu}_2\text{ZnSn}(\text{S},\text{Se})_4$ (CZTSSe) and $\text{CuIn}(\text{S},\text{Se})_2$ (CISSe). These materials have a direct band gap energy for light absorption and comprise of earth-abundant elements, making them ideal candidates for solar cell applications. Various fabrication techniques will also be explored to assist in determining the most cost-effective light-absorber-layer for efficient solar cells.

1.1 General Introduction

With the continual growth in the world's population, the consumption and demand of energy follows suit. Electricity is considered one of the most innate resources in society and the global demand for electricity is projected to increase 2.1% per year for the next 20 years.¹ This growth is set to be strongest in developing economies but requires a sustainable method of satisfying this demand. In 2019, total world consumption of energy was 162k terawatt hours (TWh) (or 583 exajoules).² For reference, Canadians pay their electricity bills in kilowatt hours (KWh) and 1 TWh is 10^9 KWh. In Canada alone, energy consumption was 3900 TWh (or 14.2 exajoules) in 2019.² Of which, fossil fuels and non-renewable sources of energy account for nearly 80% of energy production.³ While inexpensive, these resources are finite and generate harmful carbon dioxide (CO_2) and greenhouse gas emissions. In the last year alone, world CO_2 emissions reached 34169 million tonnes, of which Canada contributed 556 million tonnes.²

In order to reduce environmental damage as well as obtain a long-term solution to the demand in energy, research must be focused towards clean or renewable energy. Alternate resources such as wind, hydro, nuclear and solar have become increasingly popular and

have grown in production over the last few years. Nuclear energy is one of the most common alternative energy sources used today. Despite its success, this type of energy production is water intensive and produces great amounts of radioactive waste. Wind energy is a cleaner source of energy that has the potential to meet energy demands, however it is location dependent. Hydroelectric energy, like wind, have high startup costs in addition to its damage to the environment.⁴ The building of dams results in flooding and damage to the surrounding habitats.

Sunlight is a widely abundant, inexhaustible, free source of energy. In one hour, 173 thousand TWh of solar energy hits the earth.⁵ Thus, solar energy is one of the best energy sources that meets the demand with global availability.

Harvesting this energy divides solar power into two categories: thermal and electrical.⁶ Thermal solar power uses focused sunlight and converts it into heat for use. Electrical solar power refers to the use of photovoltaic (PV) devices which convert the light energy into electrical energy. In 2019, solar generation in the world was 724 TWh with Canada contributing 4.31 TWh.² The growth in Canadian solar generation from 2018 to 2019 was 0.46 TWh which is one of the biggest growths in the last decade, making it an increasingly attractive source of energy.²

PV devices make use of semiconductor materials that generate electricity from the absorption of photons. Since semiconductors can only absorb a specific range of energies, it is important that we look at the solar spectrum and define standards for artificial sunlight.

When defining solar irradiance in association with the earth, the path length which light takes through the atmosphere is considered. This path length is denoted as the Air Mass (AM) and when the sun is directly above the earth, the AM equals 1. However solar cells do not typically operate under AM 1 conditions since major population centers in the world lie at an angle to the sun.⁷ Thus when solar energy reaches the earth's surface at that angle, the AM in those regions equals 1.5 and is denoted as AM 1.5.⁷ Therefore, artificial sunlight with AM 1.5, operating at 100 mW/cm^2 , has been standardized to test terrestrial PV devices.⁸ The peak of solar radiation in AM 1.5, is in the visible part of the spectrum and so PV devices aim to absorb radiation in this range.

Challenges in harvesting solar energy revolve around developing cost-effective, highly efficient devices. Current commercialized photovoltaics typically use silicon wafer cells due to their high device efficiency. The highest recorded efficiency for single-junction crystalline silicon solar cells is 26.7%.⁸ However, the cost of production and installation are considered to be high. High silicon purity and a thickness of roughly 100 μm is needed for these kind of devices which can add to the cost.^{8,9} Therefore, thin-film technology is one of the promising replacements for delivering low-cost solar electricity. Very thin layers of semiconductor materials, ranging from nanometers to micrometers, are needed for thin-film devices to attain comparable efficiencies to that of silicon solar cells.¹⁰ By needing fewer materials, the cost of production is also reduced yet the challenge of obtaining high device efficiencies remain.

1.2 Principles behind photovoltaics

As aforementioned, PV devices employ semiconductor materials that enable the conversion of sunlight into electrical energy. The process of generating current in a material upon absorption of light is called the photovoltaic effect. Essentially, when light strikes the cell, a certain amount of light is absorbed into the semiconductor material. This energy from the light frees electrons from the material and an external electric field forces them to flow in a certain direction, generating current.

The distribution of electrons and holes in a material assist in explaining the types of semiconductors: *intrinsic*, *n*-type or *p*-type. An intrinsic semiconductor has an equal number of electrons and holes and thus are considered pure and do not require doping to act as a semiconductor. A good example of this is crystalline silicon. If an intrinsic semiconductor is doped with either electron-rich elements or electron-poor elements, one can create *n*-type and *p*-type semiconductors respectively. The majority charge carrier then in an *n*-type semiconductor is electrons as it is electron-rich. In a *p*-type semiconductor, the majority charge carrier is the “holes” or lack of electrons as it is electron-poor.

PV devices do not function on one semiconductor alone, instead they function on the connection of *p*-type and *n*-type semiconductors to form what is called a p-n junction.¹¹ When the two semiconductors come into contact, electrons from the *n*-type will diffuse

into the p -type. At the interface, this leaves the p -type to be electron-rich and the n -type to be electron-poor. The region in which this occurs is labeled as the Space Charge Region (SCR). This diffusion of charges occur until equilibrium is reached and an internal bias is created.

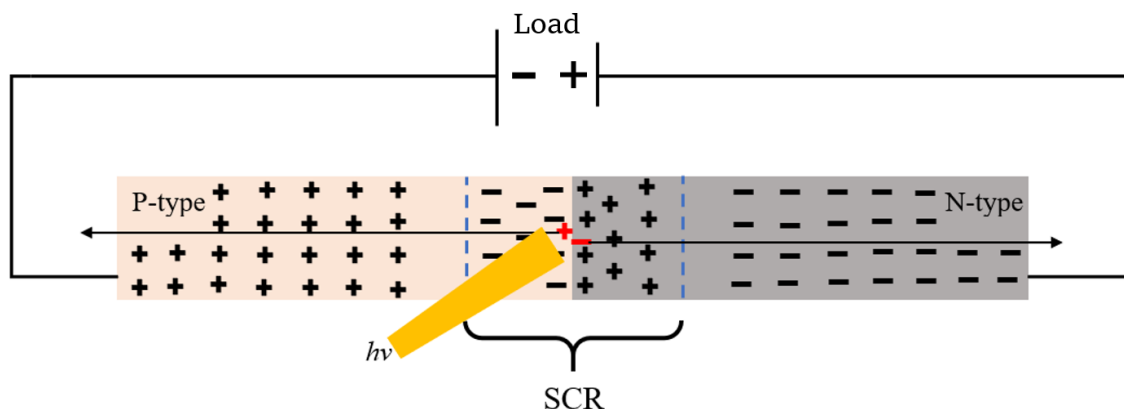


Figure 1.1: A schematic of a p-n junction and the SCR after equilibrium is reached. Light exposure produces an e-h pair (in red).

When photons from a light source are absorbed into the material, an electron-hole (e-h) pair is generated and one of two phenomena will occur. If the e-h pair is generated in the bulk p -type or n -type semiconductor, the charges will recombine, and no current is generated. However, if the e-h pair is generated within the SCR, the internal bias will cause the electron to move toward the n -type semiconductor and the hole to “move” toward the p -type semiconductor. The extraction of the e-h pair from the SCR drives current flow in the PV device. Thus, by applying an external bias in the reverse direction, with the anode connected to the p -type instead of the n -type, charge is pushed away and out of the SCR. Having the bias applied in the forward direction only encourages charge to stay within the SCR and generate no current.

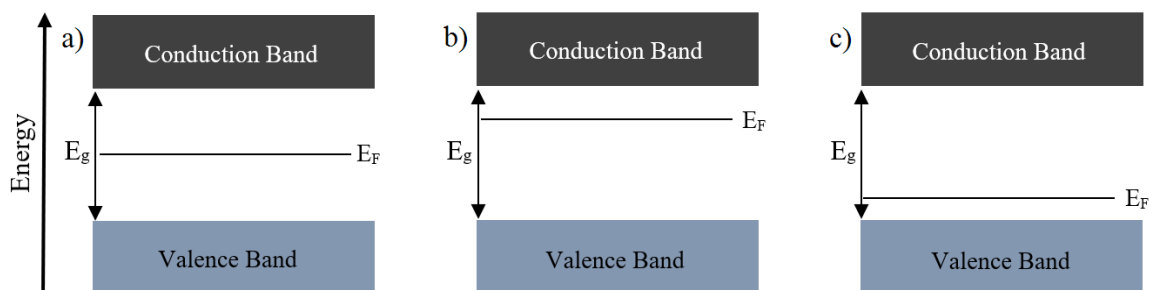


Figure 1.2: Energy band diagrams of a) an *intrinsic* semiconductor, b) an *n*-type semiconductor and c) a *p*-type semiconductor, where E_F is the Fermi level energy.

In a solid material, the abundance of energy forms continuous bands, unlike a single atom.¹² These bands known as the valence band (VB) and the conduction band (CB) are separated by a gap denoted as the band gap energy (E_g). The E_g , measured in electron volts (eV), is the minimum energy require in order to excite an electron from the VB to the CB. By doing this, electrons are free to move around in the material to potentially generate current. Light that strikes the semiconductors come in a wide range of energies but only photons with energy within the E_g can be absorbed. This leads to energy loss on the PV cell. The Shockley-Queisser limit considers energy losses by the cell and photons with energies outside the E_g and states that the optimal E_g for a single p-n junction PV cell is 1.4 eV. This translates to a maximum efficiency of 33.7%.^{13, 14}

1.3 Thin film photovoltaics

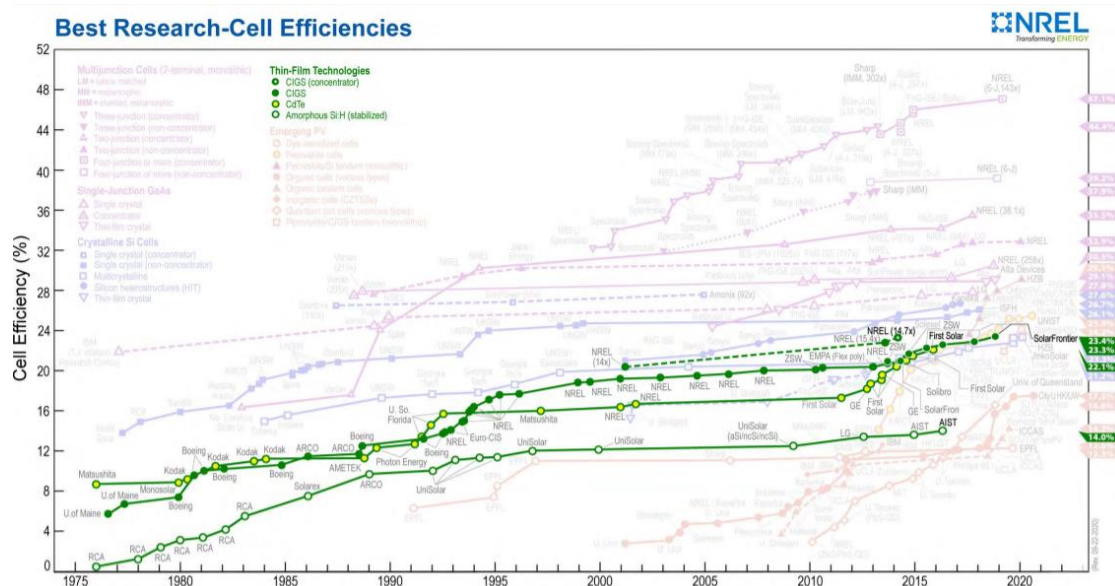


Figure 1.3: Best solar cell efficiencies involving thin-film technologies as of 2020.¹⁵

To fulfill the requirement of an ideal light-absorber-layer with the optimal band gap near 1.4 eV, $\text{Cu}(\text{In}_x\text{Ga}_{1-x})\text{Se}_2$ (CIGS) has attained interest due to its tunable E_g between 1.0 and 1.7 eV and high absorption coefficient.^{16, 17} The efficiency for CIGS solar cells has been steadily growing over the past 20 years as seen in Figure 1.3. The highest recorded efficiency for a CIGS solar cell is 23.4%, which is competitive with traditional silicon solar cell efficiencies.¹⁸ With efficiencies higher than 20%, CIGS is a successfully commercialized thin-film material in the PV market. Nevertheless, the biggest limitation of CIGS is its use of rare and expensive elements such as indium, selenium and gallium. The cost of the solar cell is then very high to produce, and alternatives must be pursued. Recent advancements to fabricate more environmentally friendly and cheap absorber materials involve the use of copper and zinc.

A typical structure of a thin-film PV device can be seen below in Figure 1.4. In this work, Mo-coated glass has been chosen as the back-contact due to its high conductivity. The next layer is the *p*-type light-absorber-layer that is responsible for light absorption. Cadmium sulfide (CdS) is a common buffer layer on top of the light-absorbing layer. It is an *n*-type semiconductor used to enhance photocurrent and charge flow in the device. The top two

layers are the window layers or as commonly known, the transparent conducting oxide (TCO) layers. In this work zinc oxide (ZnO) and aluminum-doped zinc oxide (AZO) were utilized. These layers protect the layers underneath from degradation, increase conductivity and form the p-n junction with the light-absorbing layer.¹⁹

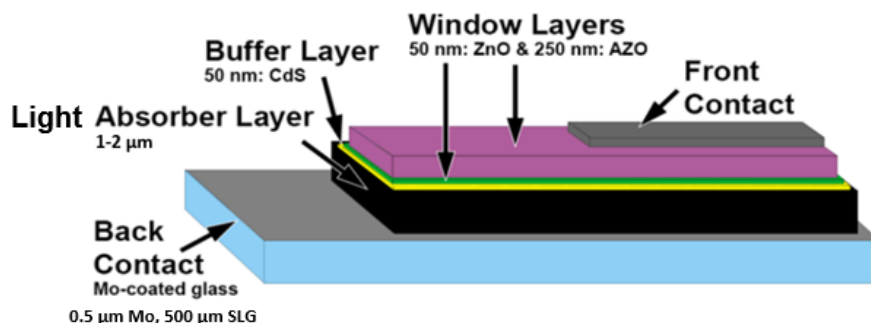


Figure 1.4: Schematic of a fabricated thin film solar cell.

In this thesis, the light absorbing layer was varied to study the absorption and photoresponse of each material. Later, the performance of each material is compared to its cost to determine which has the most promise for future thin-film PV devices.

1.3.1 CZTS & CZTSe

$\text{Cu}_2\text{ZnSnS}_4$ (CZTS) and $\text{Cu}_2\text{ZnSnSe}_4$ (CZTSe) have attracted attention as an ideal derivative to replace CIGS in photovoltaics as it reduces material costs. By replacing gallium and indium with zinc and tin, the resulting films comprise of earth-abundant, non-toxic elements. Both CZTS and CZTSe are quaternary chalcogenide *p*-type semiconductors. The Cu-on-Zn defect, known as the Cu_{Zn} antisites, is an acceptor that bears the lowest formation energy compared to other defects or donors that may form. Therefore, differing copper content can affect the electronic properties and the Cu_{Zn} antisites are the biggest contributor to the *p*-type conductivity of these two materials.^{20, 21, 22} Therefore, the of the *p*-type conductivity.

They have a tunable E_g of 1.4-1.5 eV and 1.0 eV for CZTS and CZTSe respectively which pairs well to the range of intensity for the AM1.5 solar spectrum.^{23, 24} These materials also have high absorption coefficients of $10^4 - 10^5 \text{ cm}^{-1}$.²⁴ Record laboratory efficiencies for

CZTS and CZTSe are currently 11% and 11.8%, respectively.^{25, 26} By incorporating a sulfo-selenide blend to create $\text{Cu}_2\text{ZnSn}(\text{S,Se})_4$ (CZTSSe), a maximum laboratory efficiency of 12.6% has been achieved.²⁷ Various deposition techniques have been explored such as electrodeposition, magnetron sputtering and co-evaporation techniques.^{28, 29} Ideal compositions for high efficiencies of these chalcogenides are not stoichiometric but are synthesized with Cu-poor, Zn-rich compositions. This however increases the possibility of formation for different crystal phases, defects and impurities which can result in current losses. Therefore, fabrication focuses on the control of conditions to ensure minimal current loss.

1.3.2 CIS & CISE

CuInS_2 (CIS) and CuInSe_2 (CISE) are ternary chalcopyrite semiconductors. Their production aims to overcome toxicity and cost issues of CIGS solar cells in a similar way to CZTS and CZTSe. The *p*-type conductivity in these materials stems from the acceptor copper vacancy defect, V_{Cu} , as it has a lower formation energy than antisites in CIS and CISE materials.^{21, 30} Copper, indium, sulfur and selenium are relatively non-toxic, and with the exception of indium, fairly inexpensive earth-abundant elements. The removal of gallium decreases the cost of PV device. Both CIS and CISE have gained interest due to their interesting optoelectronic properties and high absorption coefficient of $10^4 - 10^5 \text{ cm}^{-1}$.^{31, 32} Direct band gap energies of CIS and CISE are 1.54 eV and 1.0 eV respectively.^{31, 32}

Current laboratory efficiencies have reached up to 23% for CIS and 17% for CISE.^{33, 34} Using a combination of sulfur and selenium, a $\text{CuIn}(\text{S,Se})_2$ (CISSe) absorber layer has been created and achieved a maximum efficiency of 11.3% via an electrodeposition method.³⁵ Numerous deposition methods have been researched such as spin-coating, magnetron sputtering and electrodeposition. Highly efficient CIS or CISE devices were manufactured using techniques that are not easily scalable and often involve toxic conditions such as H_2S or hydrazine solutions.^{36, 37} Therefore, future fabrication focuses on low-cost, non-toxic conditions as the high efficiency easily compensates for the material price.

1.4 Characterization methods

1.4.1 Scanning electron microscopy & Energy-dispersive x-ray spectroscopy

Scanning electron microscopy (SEM) involves probing materials with a focused electron beam. While the beam scans the surface of the material, backscattered electrons and secondary electrons are created.³⁸ Secondary electrons are formed when electrons from the beam collide with valence electrons and detection of these electrons is used to form a surface image and provide morphological information. Backscattering is caused by reflection of the initial electrons and the detection of this provides the topographical contrast of the image. When the incident beam ejects an electron and creates a vacancy, x-rays are produced. Thus, an outer shell electron falls to a lower energy level to fill the vacancy and the difference in binding energies is emitted as an x-ray. The x-rays emitted from material can be collected for energy dispersive x-ray spectroscopy (EDX). EDX is generally integrated into SEM and is typically used for compositional analysis of the material.³⁸

1.4.2 X-ray diffraction

X-rays of a known wavelength are reflected from crystal planes of a material causing constructive and destructive interference. The x-rays are scattered but only the ones with constructive interference are observed. The sum of the angle of diffraction and angle of incidence is 2θ since the angles are equal. X-ray diffraction (XRD) correlates the patterns produced by x-ray scattering to the crystal structure using Bragg's law.³⁸

$$\lambda = 2d\sin\theta \quad (1.1)$$

Where λ is incident wavelength, d is spacing between planes and θ is Bragg angle. Each plane of a material, defined by miller indices h , k and l , is unique as it has a distinct Bragg angle. Therefore, a material can be identified, and its crystallinity can be characterized via an x-ray diffractogram.

1.4.3 X-ray photoelectron spectroscopy

X-ray photoelectron spectroscopy (XPS) is a surface spectroscopic technique based on the photoelectric effect. By using XPS, the elemental composition and the bonding of elements within a material can be determined. X-rays are focused onto a sample and when electrons absorb enough energy, they are ejected from sample with certain kinetic energy. The ejected electron energy is analyzed by detector and a plot of binding energy versus intensity is created. Electrons of different energies follow different paths through the detector, allowing differentiation of species. Atoms in compound being tested by XPS is determined by the following equation.³⁹

$$E_{\text{binding}} = E_{\text{photon}} - (E_{\text{kinetic}} + \phi) \quad (1.2)$$

E_{binding} is the binding energy of an electron attracted to nucleus. The E_{photon} is the energy of incident x-rays and E_{kinetic} is the energy of ejected electrons. Work function (ϕ) is a correction factor for the instrument and correlates to a minimum energy required to eject an electron.³⁹ Since the incident energy and work function are known and kinetic energy is measured, binding energy can be calculated. Electrons in orbitals farther from nucleus, less energy required to eject them, therefore binding is lower for higher orbitals. Chemical shifts can also be determined using XPS since binding energy depends on not only the electron shell but the environment of the electron.⁴⁰

1.4.4 Synchrotron based x-ray absorption spectroscopy

Synchrotron radiation (SR) is useful in providing detailed structural analysis of a material in question as it highly brilliant and collimated light. It is produced by accelerating electrons to near the speed of light, and by act of centripetal force on the particles, electromagnetic radiation is emitted.⁴¹ This radiation is tunable and can vary from x-rays to infrared energies. The use of SR in the solar cell field generally pertains to the detection of secondary phases and disordered atoms.⁴² X-ray Absorption Fine Structure (XAFS) is a measure of the absorption coefficient of a material at various energies. This technique is similar to UV-VIS absorption however the absorption of x-rays in XAFS, causes the ejection of a core-level electron.⁴³ Each element has its own specific absorption energy (E_0) and thus SR techniques can determine which elements are present. Any shift or change in

intensity of the E_0 is indicative of a change in oxidation state. The sharp rise in absorption coefficient occurs when the energy of the photon corresponds to the energy shell of the absorbing atom and is termed as the “white line” at E_0 .⁴⁴

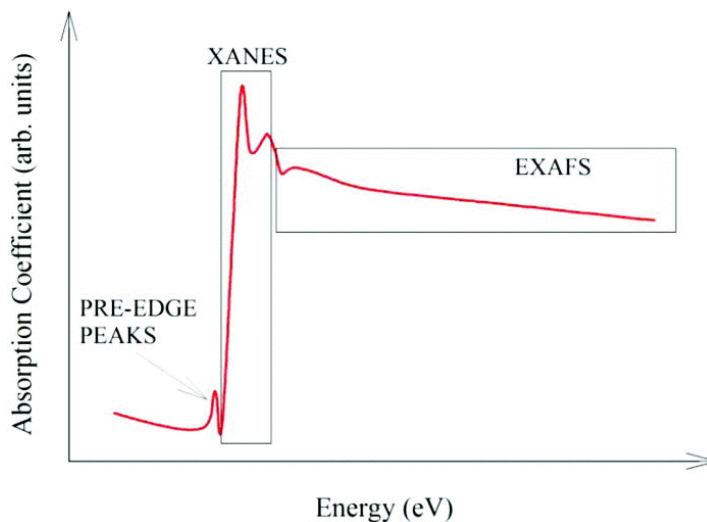


Figure 1.5: Schematic of a typical XAFS spectrum with the XANES and EXAFS region specified.⁴⁵

XAFS is broken down into X-ray Absorption Near Edge Structure (XANES) and Extended X-ray Absorption Fine Structure (EXAFS). XANES is defined as the region 10 eV below and 30 eV above the E_0 , which includes pre-edge features and probes the local region of the core level.⁴⁶ Pre-edge features investigate the transitions of excited electrons and any alterations reflect changes in local geometry, oxidation state and bonding.^{44, 47} XANES is used to probe local chemistry of the atom whereas EXAFS investigates the surrounding or extended environment of the atom and is defined as the region from 30 eV to 1000 eV after E_0 .⁴⁶ EXAFS involves transforming the absorption coefficient spectrum into a photoelectron momentum k -space spectrum. The result is an oscillating spectrum where elastic scattering is apparent and oscillations decay with respect to increasing wavenumber. K -space can be converted using a Fourier transform to provide radial distances or a r -space spectrum. From this spectrum, the distance between the absorbing atom and surrounding atoms can be obtained.⁴³ Deconvolution of these spectra yield structural information and combined with qualitative information from XANES, it can provide structural explanation for photoresponse seen in photoelectrochemical measurements (PECMs).

1.4.5 UV-VIS absorption spectroscopy

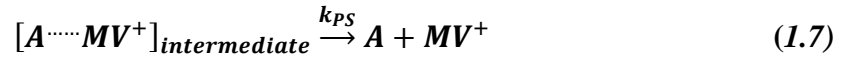
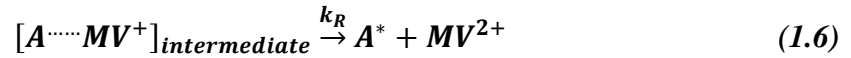
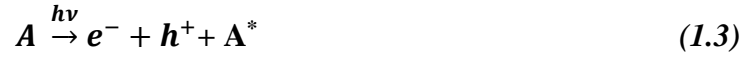
UV-VIS spectroscopy is used to determine the absorbance of a compound at various wavelengths with the Beer-Lambert Law being the principle behind absorbance spectroscopy. It states that absorbance can be measured or calculated knowing the concentration of the compound in solution, the molar absorptivity constant and the mean path length of the sample holder. An absorption spectrum can also undergo a Tauc plot conversion in order to determine the E_g of the material.⁴⁸

A typical Tauc plot displays the energy of light ($h\nu$) on the x-axis and the quantity $(\alpha h\nu)^{1/r}$ on the y-axis where α is the absorption coefficient of the material. There are four different type of electronic transitions for semiconductor materials and denoted by the exponent r . If $r = 1/2$, it is a direct allowed transition. If $r = 3/2$ it is a direct forbidden transition. If $r = 2$ it is an indirect allowed transition and finally if $r = 3$, it is an indirect forbidden transition.⁴⁹ The resultant Tauc plot attains a linear region that represents the onset of absorption and by extrapolation to the x-axis, E_g is obtained.^{50, 51}

1.4.6 Photoelectrochemical measurements

The complicated disposition of the many layers in a full PV device often makes it difficult to study and understand inefficiencies. A systematic approach is required to comb through defects and optimize layers. The light-absorbing-layer is the most important feature in any device. Therefore, it should be first appropriately characterized for its performance before continuing the manufacturing process. Photoelectrochemical measurements (PECMs) can ensure the film is photoactive and, in this work, makes use of an oxidant in solution phase within a three-electrode electrochemical cell. The absorber layer acts as the working electrode in this system to measure the transfer of charge across the film/solution interface. A saturated calomel electrode (SCE) is generally chosen as the reference electrode as it has a known potential to refer to. To complete the cell circuit, electrons are transferred from the working electrode to the counter electrode. Platinum is typically selected for its stability in electrolyte solutions and large surface area to compensate for the charge. In this work, methyl viologen (MV^{2+}) is the solution-phase oxidant as the reduction potential is within the E_g of the absorber to facilitate efficient charge transfer.^{52, 53} Current is measured upon

illumination of the absorber layer under an applied bias. The reactions that occur in solution can be summarized by the following equations where “A” stands for the absorber layer.



Upon illumination, a photon creates an e-h pair and an excited state of the absorber layer (*equation 1.3*). This photogenerated e-h pair can either decay (*equation 1.4*) or move on to create an intermediate species with the MV^{2+} (*equation 1.5*). This intermediate can then participate in one of two phenomena. The charges can recombine within the absorber film and no reduction of MV^{2+} is observed (*equation 1.6*) or the intermediate can undergo product separation to produce MV^{+} (*equation 1.7*). *Equations 1.4* and *1.6* result in no current, therefore, are not desired reactions. Progress from *equation 1.3* to *1.5* is considered favourable movement and measurable photocurrent can be collected from *equation 1.7*.

1.4.7 Current – voltage measurements

Current-voltage measurements are used to determine the efficiency of a PV device. Efficiency is defined as the ratio of energy output by the device to the energy input from the solar energy, where η is efficiency, P_{max} is the power output from the device and P_{in} is the input power.

$$\eta = \frac{P_{max}}{P_{in}} \quad (1.8)$$

Typical measurements operate under standard conditions of 100 mW/cm^2 at AM1.5. The quality of PV devices can also be determined by the Fill Factor (FF) as the P_{max} is dependent on it.⁵⁴

$$FF = \frac{I_{mp} * V_{mp}}{I_{sc} * V_{oc}} \quad (1.9)$$

The current and voltage at P_{max} are denoted as I_{MP} and V_{MP} respectively. While I_{SC} and V_{OC} are the short-circuit current and open-circuit potential respectively. These parameters affect the overall performance and are used to determine the efficiency of a PV device.

1.5 Scope of thesis

This thesis will focus on optimizing chalcogenide thin film PVs alongside debating which p -type material is the most efficient and remunerative deal for an absorber layer. The research presented is divided into three chapters, one for each p -type light-absorber-layer studied. Each chapter will begin with a brief introduction discussing relevant theory, followed by an experimental section in reference to the studies. The results will be presented along with conclusions about final devices produced with the absorber layer of focus for comparisons later. The initial hypothesis of this project focused on the effect of post-process etching to remove surface impurities, fabricating a more efficient film.

Chapter 2 deals with the solvothermal synthesis of CZTS nanocrystals (NCs) via a one-pot method. The effect of post-process etching with glacial acetic acid on the physical properties and performance on the film was studied. From this, an electron band structure of the p - n junction between the CZTS NCs and CdS layers was determined in order to ascertain the efficiency of this junction. The CZTS absorber layer was also fabricated using electrochemical deposition for controllable uniformity of the layer and was then compared to the CZTS NC based film.

The following next two chapters utilized the electrochemical deposition technique as it was found to be reproducible and result in increased film uniformity. In Chapter 3, CZT(S,Se) was produced and optimized via the use of PECMs. The photophysical and optical properties were studied after the incorporation of selenium. Post-process etching with glacial acetic acid was also tested to determine its result on the performance of both the CZT(S,Se) layer and the full device. In Chapter 4, a CI(S,Se) film was fabricated and the consequence of selenium and glacial acetic acid on the film was explored through PECMs and other conventional methods mentioned in Chapter 3.

The consequent layers needed to create a full device were not explored or optimized in this thesis and followed fabrication procedures from previous work. Chapter 5 consists of a summation and comparison of all the device findings from the earlier chapters. The range of device efficiency and parameters are discussed over the three materials and the pursuit for the most remunerative deal of the three is concluded. This last chapter also provides strategies to move forward in order to further improve fabrication and efficiency.

1.6 References

1. IEA *World Energy Outlook 2019*; 2019.
2. BP *Statistical Review of World Energy | 2020 69th Edition*; 2020; pp 1-68.
3. IEA *World Energy Balances: Statistics Report*; 2020.
4. Halkos, G. E.; Gkampoura, E.-C., Reviewing Usage, Potentials, and Limitations of Renewable Energy Sources, *Energies*, **2020**, *13*, 1-19.
5. Archer, D., *Global Warming: Understanding the Forecast*, 2nd ed.; Wiley, 2011.
6. Siksnylyte-Butkiene, I.; Zavadskas, E. K.; Streimikiene, D., Multi-Criteria Decision-Making (MCDM) for the Assessment of Renewable Energy Technologies in a Household: A Review, *Energies*, **2020**, *13*, 1-22.
7. Gueymard, C., The Sun's Total and Spectral Irradiance for Solar Energy Applications and Solar Radiation Models, *Sol. Energy*, **2004**, *76*, 423-453.
8. Andreani, L. C.; Bozzola, A.; Kowalczewski, P.; Liscidini, M.; Redorici, L., Silicon Solar Cells: Toward the Efficiency Limits, *Adv. Phys.*, **2019**, *4*, 125-148.
9. Flamant, G.; Kurtcuoglu, V.; Murray, J.; Steinfeld, A., Purification of Metallurgical Grade Silicon by a Solar Process, *Sol. Energy Mater. Sol. Cells*, **2006**, *90*, 2099-2106.
10. Muteri, V.; Cellura; Curto; Franzitta; Longo; Mistretta; Parisi, M. L., Review on Life Cycle Assessment of Solar Photovoltaic Panels, *Energies*, **2020**, *13*, 1-38.
11. Guo, K. W., Green Nanotechnology of Trends in Future Energy: A Review, *Int. J. Energy Res.*, **2012**, *36*, 1-17.
12. Bard, A. J.; Faulkner, L. R., *Electrochemical Methods : Fundamentals and Applications* 2nd ed.; John Wiley & Sons, Inc., 2001.
13. Shockley, W.; Queisser, H. J., Detailed Balance Limit of Efficiency of P-N Junction Solar Cells, *J. Appl. Phys.*, **1961**, *32*, 510-519.
14. Ehrler, B.; Alarcón-Lladó, E.; Tabernig, S. W.; Veeken, T.; Garnett, E. C.; Polman, A., Photovoltaics Reaching for the Shockley–Queisser Limit, *ACS Energy Letters*, **2020**, *5*, 3029-3033.

15. NREL Best Research-Cell Efficiencies: Thin Film Technologies. <https://www.nrel.gov/pv/assets/pdfs/cell-pv-eff-thinfilm.20200922.pdf>, (accessed November 5, 2020).
16. Li, H.; Qu, F.; Luo, H.; Niu, X.; Chen, J.; Zhang, Y.; Yao, H.; Jia, X.; Gu, H.; Wang, W., Engineering CIGS Grains Qualities to Achieve High Efficiency in Ultrathin $\text{Cu}(\text{In}_x\text{Ga}_{1-x})\text{Se}_2$ Solar Cells with a Single-Gradient Band Gap Profile, *Results Phys.*, **2019**, *12*, 704-711.
17. Mufti, N.; Amrillah, T.; Taufiq, A.; Sunaryono; Aripriharta; Diantoro, M.; Zulhadjri; Nur, H., Review of CIGS-Based Solar Cells Manufacturing by Structural Engineering, *Sol. Energy*, **2020**, *207*, 1146-1157.
18. Green, M. A.; Dunlop, E. D.; Hohl-Ebinger, J.; Yoshita, M.; Kopidakis, N.; Hao, X., Solar Cell Efficiency Tables (Version 56), *Prog. Photovolt.*, **2020**, *28*, 629-638.
19. Simya, O. K.; Balachander, K.; Dhanalakshmi, D.; Ashok, A., Performance of Different Anti-Reflection Coating and TCO Layers for Kesterite Based Thin Film Photovoltaic Devices Using Essential Macleod Simulation Program, *Superlattices Microstruct.*, **2020**, *145*, 1-12.
20. Zhang, S. B.; Wei, S.-H.; Zunger, A.; Katayama-Yoshida, H., Defect Physics of the CuInSe_2 Chalcopyrite Semiconductor, *Phys. Rev. B*, **1998**, *57*, 9642-9656.
21. Chen, S.; Yang, J.-H.; Gong, X.; Walsh, A.; Wei, S.-H., Intrinsic Point Defects and Complexes in the Quaternary Kesterite Semiconductor $\text{Cu}_2\text{ZnSnS}_4$, *Phys. Rev. B*, **2010**, *81*, 1-10.
22. Khoshmashrab, S.; Turnbull, M. J.; Vaccarello, D.; Nie, Y.; Martin, S.; Love, D. A.; Lau, P. K.; Sun, X.; Ding, Z., Effects of Cu Content on the Photoelectrochemistry of $\text{Cu}_2\text{ZnSnS}_4$ Nanocrystal Thin Films, *Electrochim. Acta*, **2015**, *162*, 176-184.
23. Mitzi, D. B.; Gunawan, O.; Todorov, T. K.; Wang, K.; Guha, S., The Path Towards a High-Performance Solution-Processed Kesterite Solar Cell, *Sol. Energy Mater. Sol. Cells*, **2011**, *95*, 1421-1436.
24. Katagiri, H.; Jimbo, K.; Maw, W. S.; Oishi, K.; Yamazaki, M.; Araki, H.; Takeuchi, A., Development of CZTS-Based Thin Film Solar Cells, *Thin Solid Films*, **2009**, *517*, 2455-2460.
25. Yan, C.; Sun, K.; Huang, J.; Johnston, S.; Liu, F.; Puthen Veetil, B.; Sun, K.; pu, A.; Zhou, F.; Stride, J.; Green, M.; Hao, X., Beyond 11% Efficient Sulfide Kesterite $\text{Cu}_2\text{Zn}_x\text{Cd}_{1-x}\text{SnS}_4$ Solar Cell: Effects of Cadmium Alloying, *ACS Energy Lett.*, **2017**, *2*, 930-936.
26. Kumar, V.; Singh, U. P., Effect of Selenization Temperature on the Formation of CZTSe Absorber Layer, *Appl. Phys. A*, **2019**, *125*, 1-8.
27. Wang, W.; Winkler, M. T.; Gunawan, O.; Gokmen, T.; Todorov, T. K.; Zhu, Y.; Mitzi, D. B., Device Characteristics of CZTSSe Thin-Film Solar Cells with 12.6% Efficiency, *Adv. Energy Mater.*, **2014**, *4*, 1-5.
28. Zoppi, G.; Forbes, I.; Miles, R. W.; Dale, P. J.; Scragg, J. J.; Peter, L. M., $\text{Cu}_2\text{ZnSnSe}_4$ Thin Film Solar Cells Produced by Selenisation of Magnetron Sputtered Precursors, *Prog. Photovolt.*, **2009**, *17*, 315-319.

29. Kim, Y.-C.; Jeong, H.-J.; Lee, S. K.; Kim, S.-T.; Jang, J.-H., The Effect of S/(S+Se) Ratios on the Formation of Secondary Phases in the Band Gap Graded $\text{Cu}_2\text{ZnSn}(\text{S},\text{Se})_4$ Thin Film Solar Cells, *J. Alloys Compd.*, **2019**, 793, 289-294.
30. Wei, S.-H.; Zhang, S. B., Defect Properties of CuInSe_2 and CuGaSe_2 , *J. Phys. Chem. Solids*, **2005**, 66, 1994-1999.
31. Tuttle, J.; Albin, D.; Goral, J.; Kennedy, C.; Noufi, R., Effects of Composition and Substrate Temperature on the Electro-Optical Properties of Thin-Film CuInSe_2 and CuGaSe_2 , *Sol. Cells*, **1988**, 24, 67-79.
32. Scheer, R., Open Questions after 20 Years of CuInS_2 Research, *Prog. Photovolt.*, **2012**, 20, 507-511.
33. Hutchins, M. Solar Frontier Hits New CIS Cell Efficiency Record. <https://www.pv-magazine.com/2019/01/21/solar-frontier-hits-new-cis-cell-efficiency-record/>, 2019 (accessed November 5, 2020).
34. Adurodija, F.; Carter, M. J.; Hill, R., Novel Method of Synthesizing P- CuInSe_2 Thin Films from the Stacked Elemental Layers Using a Closed Graphite Box, *IEEE Photovoltaic Specialists Conference (PVSC)*, **1995**, 1, 186-189
35. Li, W.; Wang, M.; Pan, Y.; Han, L.; Lai, Y.; Jiang, Y.; jiang, L.; Zhang, K.; Liu, F., Effect of Sulfurization Temperature on the Properties of $\text{CuIn}(\text{S},\text{Se})_2$ Thin Films Fabricated from Electrodeposited CuInSe_2 Precursors, *Superlattices Microstruct.*, **2018**, 122, 614-623.
36. Gunawan; Haris, A.; Widiyandari, H.; Widodo, D. S., Effect of Potentials and Electric Charges for Copper and Indium Depositions to the Photocurrent Responses of CuInS_2 Thin Films Fabricated by Stack Electrodeposition Followed by Sulfurization, *IOP Conference Series: Materials Science and Engineering*, **2018**, 349, 1-7.
37. Lee, S.; Ikeda, S.; Yagi, T.; Harada, T.; Ennaoui, A.; Matsumura, M., Fabrication of CuInS_2 Films from Electrodeposited Cu/in Bilayers: Effects of Preheat Treatment on Their Structural, Photoelectrochemical and Solar Cell Properties, *Phys. Chem. Chem. Phys.*, **2011**, 13, 6662-6669.
38. Skoog, D. A.; Holler, F. J.; Crouch, S. R., *Principles of Instrumental Analysis*, 6th ed.; Thomson Brooks/Cole, 2007.
39. Brandon, D.; Kaplan, W. D., *Microstructural Characterization of Materials*, 2nd ed.; John Wiley & Sons, 2013.
40. Moulder, J. F.; Chastain, J., *Handbook of X-Ray Photoelectron Spectroscopy: A Reference Book of Standard Spectra for Identification and Interpretation of XPS Data*, Physical Electronics Division, Perkin-Elmer Corporation, 1992.
41. Willmott, P., *An Introduction to Synchrotron Radiation*, 2nd ed.; Wiley, 2011; p 39-86.
42. Mendis, B. G.; Shannon, M. D.; Goodman, M. C.; Major, J. D.; Claridge, R.; Halliday, D. P.; Durose, K., Direct Observation of Cu, Zn Cation Disorder in $\text{Cu}_2\text{ZnSnS}_4$ Solar Cell Absorber Material Using Aberration Corrected Scanning Transmission Electron Microscopy, *Prog. Photovolt.:Res. Appl.*, **2014**, 22, 24-34.

43. Zhang, P., X-Ray Spectroscopy of Gold–Thiolate Nanoclusters, *J. Phys. Chem. C*, **2014**, *118*, 25291-25299.
44. Liu, X.; Weng, T.-C., Synchrotron-Based X-Ray Absorption Spectroscopy for Energy Materials, *MRS Bull.*, **2016**, *41*, 466-472.
45. Oguz Er, A.; Chen, J.; Rentzepis, P. M., Ultrafast Time Resolved X-Ray Diffraction, Extended X-Ray Absorption Fine Structure and X-Ray Absorption near Edge Structure, *J. Appl. Phys.*, **2012**, *112*, 1-17.
46. Teo, B. K., *EXAFS: Basic Principles and Data Analysis*, 1st ed.; Springer-Verlag, 1986.
47. Lamberti, C.; Bordiga, S.; Bonino, F.; Prestipino, C.; Berlier, G.; Capello, L.; D'Acapito, F.; Llabrés i Xamena, F. X.; Zecchina, A., Determination of the Oxidation and Coordination State of Copper on Different Cu-Based Catalysts by Xanes Spectroscopy in Situ or in Operando Conditions, *Phys. Chem. Chem. Phys.*, **2003**, *5*, 4502-4509.
48. Tauc, J., Optical Properties and Electronic Structure of Amorphous Ge and Si, *Mater. Res. Bull.*, **1968**, *3*, 37-46.
49. Davis, E. A.; Mott, N. F., Conduction in Non-Crystalline Systems V. Conductivity, Optical Absorption and Photoconductivity in Amorphous Semiconductors, *Philos. Mag.*, **1970**, *22*, 0903-0922.
50. Escobedo-Morales, A.; Ruiz-López, I. I.; Ruiz-Peralta, M. d.; Tepech-Carrillo, L.; Sánchez-Cantú, M.; Moreno-Orea, J. E., Automated Method for the Determination of the Band Gap Energy of Pure and Mixed Powder Samples Using Diffuse Reflectance Spectroscopy, *Heliyon*, **2019**, *5*, 1-9.
51. Jubu, P. R.; Yam, F. K.; Igba, V. M.; Beh, K. P., Tauc-Plot Scale and Extrapolation Effect on Bandgap Estimation from UV–VIS–NIR Data – a Case Study of B-Ga₂O₃, *J. Solid State Chem.*, **2020**, *290*, 1-8.
52. Jiang, T.; Xie, T.; Yang, W.; Chen, L.; Fan, H.; Wang, D., Photoelectrochemical and Photovoltaic Properties of P–N Cu₂O Homojunction Films and Their Photocatalytic Performance, *J. Phys. Chem. C*, **2013**, *117*, 4619-4624.
53. Bennett, T.; Niroomand, H.; Pamu, R.; Ivanov, I.; Mukherjee, D.; Khomami, B., Elucidating the Role of Methyl Viologen as a Scavenger of Photoactivated Electrons from Photosystem I under Aerobic and Anaerobic Conditions, *Phys. Chem. Chem. Phys.*, **2016**, *18*, 8512-8521.
54. Rauschenbach, H., *Solar Cell Array Design Handbook: The Principles and Technology of Photovoltaic Energy Conversion*, 1st ed.; Van Nostrand Reinhold Company, 1980.

Chapter 2

2 Fabrication and optimization of $\text{Cu}_2\text{ZnSnS}_4$ for low-cost solar devices

$\text{Cu}_2\text{ZnSnS}_4$ (CZTS) nanocrystals (NCs) were synthesized using a one-pot solvothermal method with a copper-poor stoichiometry and deposited using electrophoretic deposition. Resultant films were etched post-process with acetic acid in order to remove surface impurities inhibiting current. Using photoelectrochemical measurements (PECMs), initial photocatalytic behaviour was assessed before and after post-process etching. Synchrotron-based (SR) x-ray absorption fine structure (XAFS) was used to analyze structural abnormalities in the CZTS NCs. SR-XPS measured interfacial valence band structures of the p-n junction between the CZTS NC film and CdS. A full band diagram of the p-n junction was created before and after post-process etching to study the charge-carrier efficiency. CZTS was also electrodeposited onto Mo-coated glass and preliminary photoresponse of the film, with and without etching, was tested.

2.1 Introduction

Though inexpensive, fossil fuels are damaging to the environment and are quickly being depleted. As a result, an alternative renewable energy source is much needed and long overdue. Solar energy is a promising alternative as it is a readily available, renewable source of energy. However, the problem lies within harvesting solar energy in an efficient and effective manner. A great deal of research is currently focused around developing suitable material candidates in an attempt to build efficient solar cells and bridge this gap.

Presently, crystalline silicon is the leading material used in photovoltaic devices due to their high efficiencies, however, the caveat is their high cost of manufacturing. As a result, the need for high performance, low-cost photovoltaic devices turns research towards sustainable thin film technology as it is dependent on the quality of the light-absorber-layer.¹ Thin-film solar cells manufactured from $\text{CuIn}_x\text{Ga}_{(1-x)}\text{Se}_2$ (CIGS) were investigated and reached a maximum efficiency of 23.4%.² More recently, the development of kesterite $\text{Cu}_2\text{ZnSnS}_4$ (CZTS) has provided a better candidacy for thin-film solar devices due to their low-cost and earth-abundancy in comparison to its CIGS counterparts.

Current fabrication methods of the CZTS layer entails low-cost, minimally toxic procedures that increase the tunability of the P-N junction. As a result, long-terms goals in increasing charge-carrier flow are achieved. Past studies focusing on the structural control of the CZTS layer, examine the formation of defects such as antisites and secondary phases. These studies analyzing low-cost thin film deposition methods such as spray-deposition have found these methods to require annealing at high temperatures.^{3,4} In addition to the annealing processes, harsh post-process treatments using KCN or H₂S can result in unwanted surface impurities and should therefore be avoided.¹ In contrast, etching in glacial acetic acid provides a milder method to remove insulator layers and create for favourable conditions to extract charge-carriers.^{5,6}

To date the highest efficiency for CZTS solar cells is 11%, lower than that of a CIGS one.⁷ The low conversion efficiency is mainly attributed to recombination of charges at the CZTS/CdS interface. The addition of a layer changes the local environment of the CZTS and results in a possible increase or decrease in effectiveness of the layers in contact. As a result, this junction is important in facilitating electron transfer across the interface, which is the main focus to control device efficiency.⁴ Photoresponse is one of essential techniques used to evaluate the effectiveness of the light-absorbing layer in a device.

In the presence of light, charge- carrier flow rapidly increases in the film and can be collected by methyl viologen (MV²⁺) in solution and measured electrochemically. Ideally, device fabrication would yield higher photoresponse with each subsequent layer, however every layer can introduce defects and impurities on the surface or into the interface of the films which is detrimental to the performance. The effect on the films after post-process etching or the addition of CdS can be measured by the catalytic conversion from MV²⁺ to MV⁺ using photoelectrochemical measurements (PECMs), where greater amount of catalytic conversion is indicative of higher photoresponse.⁴ This can be associated with a greater current density difference between the light on and light off conditions.

Furthermore, it should be noted that structural components in the CZTS layer contribute greatly to the p-type character of the semiconductor.^{8, 9} In particular, the type of semiconductor reveals information of how charge-carriers flow through materials.⁴ When

the CZTS NC layer and CdS layer come into contact, the fermi level equilibrates between the two layers. When in contact, the conduction bands of the individual layers overlap and create a conduction band offset (CBO) in the overall electronic band structure. A charge imbalance then results between the uncompensated electrons and holes in the n-type and p-type lattice respectively, referred to as the Space Charge Region (SCR). The SCR creates an electric field to transfer electrons across the film interface.¹⁰

The use of synchrotron radiation is beneficial for structural analysis and accuracy of measurements in the band structure. These high energy x-rays are tunable and of high brilliance that is useful for probing materials. For materials used in solar energy, synchrotron radiation is generally used for the detection of secondary phases in a crystalline film.¹¹ However, the use of X-ray Absorption Fine Structure (XAFS) allows for the investigation of local and extended environments of a target atom through X-ray Absorption Near Edge Structure (XANES) and Extended X-ray Absorption Fine Structure (EXAFS) respectively.¹² The XAFS spectra is a measure of the change in absorption coefficient relative to the absorption of an isolated atom.¹³ This is important for detecting structural changes in various stoichiometric configurations that yield an in a high photoresponse. Synchrotron radiation is also able to detect atomic alignment of local regions and thus through X-ray Photoelectron Spectroscopy (XPS), valence band energies can be measured.^{13, 14, 15}

The work in this chapter investigates the alignment of the interfacial electronic band structure before and after removing insulator layers via post-process etching. This provides for a better understanding in how the SCR is structured. The goal is to then form a strong p-n junction that will lead to a stronger internal bias for improved device efficiency. To produce a working device with comparable efficiencies to literature, the reproducibility and control of the CZTS light-absorber-layer become the primary concerns throughout. Unless otherwise stated, all procedures were conducted in an open-air environment to keep fabrication costs low.

2.2 Experimental

2.2.1 Nanocrystal layer fabrication

CZTS NCs were fabricated solvothermally as previously reported with minor changes^{16,17}; ratios of the precursor salts were maintained at 0.9 and 1.0 for Cu/(Zn+Sn) and Zn/Sn respectively to avoid zinc antisites in the kesterite structure. By preserving these compositions, minor disparities in the ratios are produced and a maximum photoresponse is upheld. Copper (II) acetylacetonate (Sigma-Aldrich, 97%), zinc(II) chloride (Sigma-Aldrich, 98%) and tin(II) chloride (Alfa Aesar, 98%) metal precursor salts were dissolved in benzyl alcohol at 180 °C for 2 minutes then a mixture of 0.2 M thiourea and 0.097 M 1-methyl-4-phenylpyridinium (MPP) was added to the solution that was held at the same temperature for 10 minutes. Thiourea was used as the sources for sulfur in the nanocrystals as thiourea decomposes to release sulfur and MPP as a suitable capping ligand to prevent overgrowth and aggregation of nanoparticles.¹⁸

The resultant NCs were cooled down, washed with isopropanol and transferred into centrifuge tubes for separation. They were centrifuged at 14.0×10^3 times gravity for 2 minutes and repeated three times. The obtained NCs were dispersed in isopropanol to a concentration of 2 g/L using a 1510 Branson Sonicator at 40 kHz for a minimum of 30 minutes. Molybdenum-coated glass substrates were bought from University Wafer (Boston, MA) with a thickness of 0.5 μm and 500 μm , for the Molybdenum and soda-lime glass (SLG) respectively. These substrates were cut into pieces of 1 cm by 2 cm areas, etched for 10 minutes in glacial acetic acid and utilized as the back contact for devices. The above NC dispersion was then electrophoretically deposited on to the substrates using a Keithly 2400 source meter at a constant current in a range of 0.24 - 0.33 mA/cm^2 for 3.0 minutes to result in roughly a 1 μm thick film of CZTS as published elsewhere.¹⁰ Please note that these films could be etched once again in glacial acetic acid for an additional 30 minutes to remove copper oxides from the surface and edges of the film.

2.2.2 Buffer layer and full device fabrication

A buffer layer of cadmium sulfide (CdS) was deposited onto the CZTS films via chemical bath deposition (CBD). The bath was prepared by stirring a mixture of 103.5 mg of

cadmium acetate (Sigma-Aldrich, 99.99%), 4.5 mL ammonium hydroxide (Caledon, >99%) and 3 mL of 1 M ammonia acetate in a volume of 142.5 mL of MilliQ water at a temperature of 65 °C for 30 minutes. After temperature stabilization at 30 minutes, 1.5 mL of 0.5 M thiourea was added and the bath was stirred for an additional 30 minutes; the CZTS filmed substrate were then dipped into the solution immediately and the reaction was left to transpire for 7.5 minutes resulting in a 50 nm layer of CdS. Resultant CZTS/CdS films were then placed in the Ultratech/Cambridge NanoTech Savannah S200 Atomic Layer Deposition (ALD) workstation reaction chamber for 10 minutes at 150 °C under vacuum to remove water intercalation. Photoelectrochemical measurements were then taken of etched and non-etched films at this point.

For full devices, after the CBD, samples were put into the ALD instrument and heated to 200 °C for 1 hour. The deposition of both window layers, zinc oxide (ZnO) and aluminum doped zinc oxide (AZO) follows the procedures as reported by *Turnbull et al.*¹⁰ to result in layer thickness of 50 and 250 nm respectively.

2.2.3 Characterization

PECMs were carried out for the half-devices, before and after the CdS deposition in order to assess the photovoltaic quality of the films. The back contact of the device was connected to an electrode and the films were immersed in an electrolyte solution of 0.05 M MV^{2+} and 0.1 M KCl. Using a 3-electrode system with the film on Mo-coated glass, a saturated calomel electrode and a platinum wire as the working, reference and counter electrode, respectively, the potential is scanned and PECMs were taken. A linear potential sweep from 0.0 to -0.40 V at a scan rate of 5 mV/s was applied to measure the current density generated by photocatalytic conversion of MV^{2+} to MV^+ .^{19, 20} A Xenon-lamp ‘light source’ produced illumination in 3 second intervals. The resultant photocurrent as a function of the applied potential was measured using a CHI 832B electrochemical analyzer.

XAFS measurements of the Cu, Zn, and Sn K-edges were performed at the CLS@APS 20-BM beamline at the Advanced Photon Source (APS) in the Argonne National Laboratory, Argonne, IL. The beam was set in focus mode, and the wavelengths set using a Si (111) monochromator. A 400 μm vertical slit was used over 8.78 to 9.52 keV for the Cu K-edge,

9.46 to 10.4 keV for the Zn K-edge, and 29.004 to 30.069 keV for the Sn K-edge. Samples were placed 45° to the incident photons, and the 13-element Canberra detector was placed perpendicular to the beam. Detector saturation was set to 50,000 cps, and replicates were taken to a sum of 2 million total counts per element.

Synchrotron data processing was carried out using the Athena and Artemis software packages.²¹ Using Athena, spectra were normalized to the incident photon flux, I_0 , and calibrated against a standard reference foil (EXAFS Materials Inc.).¹³ The standards used for this energy calibration included a 7.5 μm thick copper foil, 10 μm zinc foil, and 50 μm tin foil. Treated data were then fit using the Artemis software package, running FEFF8.2 computational software.²¹ Fittings were based around a kesterite-phase CZTS unit cell (JCPDS card 26-0575) at room temperature, as calculated from the crystallographic information file generated using VESTA.²² Coordination number was fixed according to the theoretical value from the kesterite crystal structure. The amplitude reduction factor was fixed for each metal, with each determined by measuring the metal reference foil and fitting the metal-metal bond distance.²³

Synchrotron XPS (SR-XPS) was carried out at the Canadian Light Source on the Variable Line Spacing Plane Grating Monochromator (VLS-PGM, 11ID-2) beamline. Measurements were taken at a flux $> 1 \times 10^{11}$ on a $500 \times 500 \mu\text{m}$ spot size. Incoming photons were set at 160 eV. The beam energy was calibrated using gold foil at the Au Fermi level emission. The fermi level of a clean Mo film in good electrical contact was used in reference when measuring the valence band energies.

CZTS NC band gaps were determined through UV-VIS absorption via a Varian Cary 50 spectrometer with a 2 mM NC dispersion in isopropanol. The scans were carried out at a rate of 60 nm/s from 1100 to 400 nm. The resulting absorption spectra was transformed to create a Tauc plot which associates the absorption coefficient with the wavelength energy.

Efficiency of the final devices were measured using a 150 W Xenon Newport lamp with 100 mW/cm² and a 1.5D filter to mimic 1 sun shining. An electrode with indium was attached to the back contact as well as on to the cell area that was being tested in order to complete the circuit. Current vs. potential measurements were taken as the potential was

scanned from 1.0 to -0.2 V using an IVIUM CompactStat; this was later converted into a J-V curve to assess the photoresponse of the cell.

2.2.4 Layer-by-layer fabrication

CZTS films were fabricated using galvanostatic electrodeposition of metallic precursors with an EG&G PAR 363 potentiostat, followed by high-temperature sulfurization. A three-electrode system was employed to deposit the precursors with the Mo-coated glass as the working and a platinum mesh as the counter electrode. The reference for the copper precursor was a saturated calomel electrode while the reference for both tin and zinc precursors was an Ag/AgCl electrode. Copper was first deposited using a constant current density of 2.5 mA/cm² on the working electrode immersed in a solution containing 25 g/L CuSO₄•5H₂O (Sigma-Aldrich, 99.995%), 120 g/L NaOH (Sigma-Aldrich, 97% pellets), and 37.5 g/L D-sorbitol (Sigma-Aldrich, ≥98%). Tin was deposited on top of the copper layer with a constant current density of 6.0 mA/cm²; the electrochemical bath was comprised of 100 g/L Methane sulfonic acid, 130 g/L Tin methanesulfonate, 8 g/L Empigen BB Degerent and 3 g/L of Hydroquinone. Finally, a constant current density of 3.0 mA/cm² was applied to deposit the zinc on top of the copper and tin layers. The bath was comprised of 8 g/L ZnCl₂ (Sigma-Aldrich, 99.999%), 150 g/L KCl (Sigma-Aldrich, ≥99.0%), and 12.9 g/L poly[bis(2-chloroethyl) ether-alt-1,3-bis[3-(dimethylamino)propyl]urea] (Sigma-Aldrich, 62% wt% in H₂O).

The stacked film samples were then placed in a Thermo Scientific Lindberg Blue M Tube Furnace with a quartz tube for vacuum and argon purges. For the sulfurization of the films, a ratio of 10 mg/cm² was used for sulfur powder mass-to-sample surface area. The tube was purged three times via vacuum pump to -100 kPa then filled with argon gas to a pressure of 40 kPa. The furnace was held at a temperature of 275 °C for 20 minutes, followed by 30 minutes at 525 °C. The furnace was shut off and purged to remove any excess sulfur vapour from the system. The fabricated films were etched with acetic acid to remove copper oxides and any surface impurities.

The performance of the electrodeposited (ED) CZTS layer was characterized using PECMs in the same manner as done for the CZTS NC films.

2.3 Results and Discussion

2.3.1 Photoelectrochemical measurements of CZTS NCs

Figure 2.1 demonstrates the photoelectrochemical measurements (PECMs) of the intrinsic CZTS NC films, before (Figure 2.1a) and after (Figure 2.1b) the addition of the CdS buffer layer as well as acetic acid etched CZTS NC films before (Figure 2.1c) and after (Figure 2.1d) the CdS coating. PECMs characterize the light-absorbing quality of the film where the photoresponse is vital in determining the effectiveness of the CZTS NC and CZTS NC/CdS films.^{19, 24}

Under illumination, the minority charge carriers or photogenerated electrons within the NC film flow from the film into the MV^{2+} solution. This photo-injection that yields in absorption is described by *equation 1.3* in *Section 1.4.6*. Figure 2.1a displays an increase in current density to 1.7 mA/cm^2 as a result of this preferential electron transfer and interfacial reduction of MV^{2+} to MV^+ at the CZTS film, described by *equation 1.5*. Through electron flow from illumination, the electron transfer leads into the product separation of the CZTS and MV^+ , depicted by *equation 1.7*. However, what is observed is a gradual increase in current density instead of an instantaneous one, suggesting a recombination of charges under illumination – expressed by *equation 1.6*.

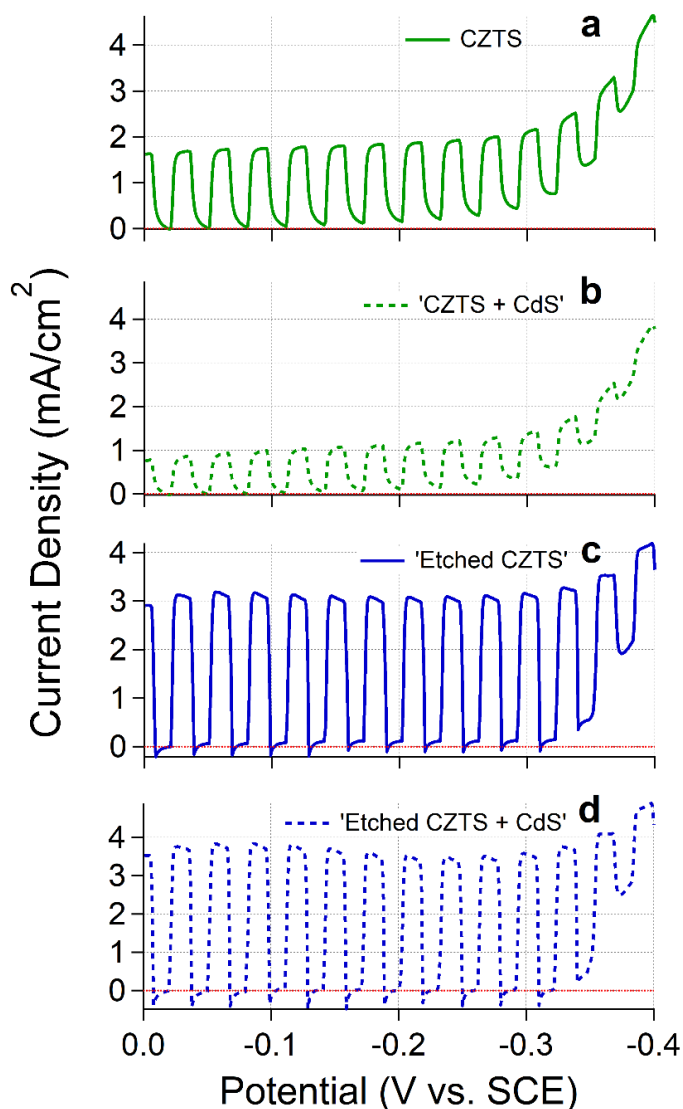


Figure 2.1: PECMs of non-etched CZTS NC films a) before and b) after CdS coating as well as etched CZTS NC films c) before and d) after CBD of CdS. Etching was processed using glacial acetic acid for 30 min.

In the absence of light in Figure 2.1a, a gradual decay is observed in the PECMs when the light is off. However, without light, the flow of electrons is stopped and thus, the current density is expected to instantaneously decrease due to recombination of charges (*equation 1.6*). This discrepancy suggests that there is continued product separation of the CZTS and MV^{2+} even after illumination of the film has stopped (*equation 1.7*). Another thing to note is that at -0.30 V, there is a shift from a Schottky junction to an Ohmic junction as the dark

current begins to increase depicted by the upwards slope of the scan.²⁵⁻²⁶ At this point, shunt resistance is reduced as electrons begin to flow freely throughout the film via alternative pathways.

When the CdS buffer layer was added, in Figure 2.1b, the maximum photoresponse upon illumination, is significantly lower than the original CZTS NC film (Figure 2.1a) at only 1.1 mA/cm^2 , as shown by the gradual increase in current density. In the absence of light, the gradual decay at 'light off' is also more prominent and shows less of an instantaneous decrease in electron flow due to product separation. A possible reason for the overall dampened photoresponse is that a resistance layer on the CZTS hindered reduction of the methyl viologen solution.²⁷ This is confirmed earlier in the scan by the larger shift to an Ohmic junction at less negative potentials.

To combat this problem, the etching post-process step with acetic acid was added. Films were etched with glacial acetic acid before (Figure 2.1c) and after (Figure 2.1d) the CdS deposition. Etching proved to be beneficial to the photoresponse as depicted by Figure 2.1c, as the maximum photoresponse almost doubled to 3.0 mA/cm^2 from the original 1.7 mA/cm^2 (Figure 2.1a) upon illumination. When the CdS buffer layer was added onto the etched film, the photoresponse in Figure 2.1d, increased even further to 3.6 mA/cm^2 indicating efficient electron transfer between the layers. Having said this, note that in Figure 2.1c and d, there is negative overshoot in the films meaning reduction is still favoured over recombination in the absence of light. In addition, there is slight recombination activity in both Figure 2.1c and d during illumination – as indicated by the gradual decrease in current density. Nevertheless, the overall photoresponse in either etched films (Figure 2.1 c or d) is higher than those of the non-etched films (Figure 2.1 a and b), until the -0.30 V potential.

The buffer layer of CdS is an n-type semiconductor to facilitate electron transfer from the p-type CZTS NC layer. This buffer layer should theoretically protect the CZTS NC layer from the following fabrication steps to yield a greater charge flow and an increase in photoresponse. However, from Figure 2.1b, it is indicative that an additional layer without etching enhances the insulator layer on the surface which results in a reduced

photoresponse. It was found that the CZTS NC film is not stable in an open-air environment which causes the surface of the film to oxidize and produce impurities which inhibit photoresponse. Therefore by etching the film's surface, the photoresponse was reported to increase after CdS deposition which follows the initial hypothesis of adding the buffer layer.^{28, 29-30} The implication of this is that etching the films before and after deposition is necessary for a smooth transfer of electrons across the CZTS/CdS interface.

2.3.2 X-ray absorption fine structure (XAFS)

The etching process is known to remove a resistive surface layer from the CZTS NC film. The degree to which etching alters the structural properties of the CZTS film was examined by means of both XANES and EXAFS at each metal K-edge, as shown in Figure 2.2.

As shown in Figure 2.2, the XANES spectra give insight into the chemistry environment changes around the absorbing metal center.^{13, 31} The Cu-center XANES spectra in Figure 2.2a displays an increased amplitude in the oscillation of the etched sample, which is clearly visible in the first trough after the white line peak in the Figure 2.2a inset. This is propagated throughout the Cu absorbance spectra in Figure 2.2a, with the etched sample (black) showing higher peak maximums, and lower minimums, than the non-etched sample (purple). This can be attributed to increased uniformity of the NCs that comprise the film, and would then indicate the removal of an insulator from the pseudo-surface of the film, possibly metal oxides.¹⁰ As previously reported, NC-based films typically display deep surface features as a result of the looser packing during deposition.²⁷ It is expected that the etching process removes surface oxides and impurities which leads to the more pronounced features seen in Figure 2.2a. We will return to this point in *Section 2.3.4*. Despite this, there are no significant changes in the overall Cu oxidation state or geometry within the film.

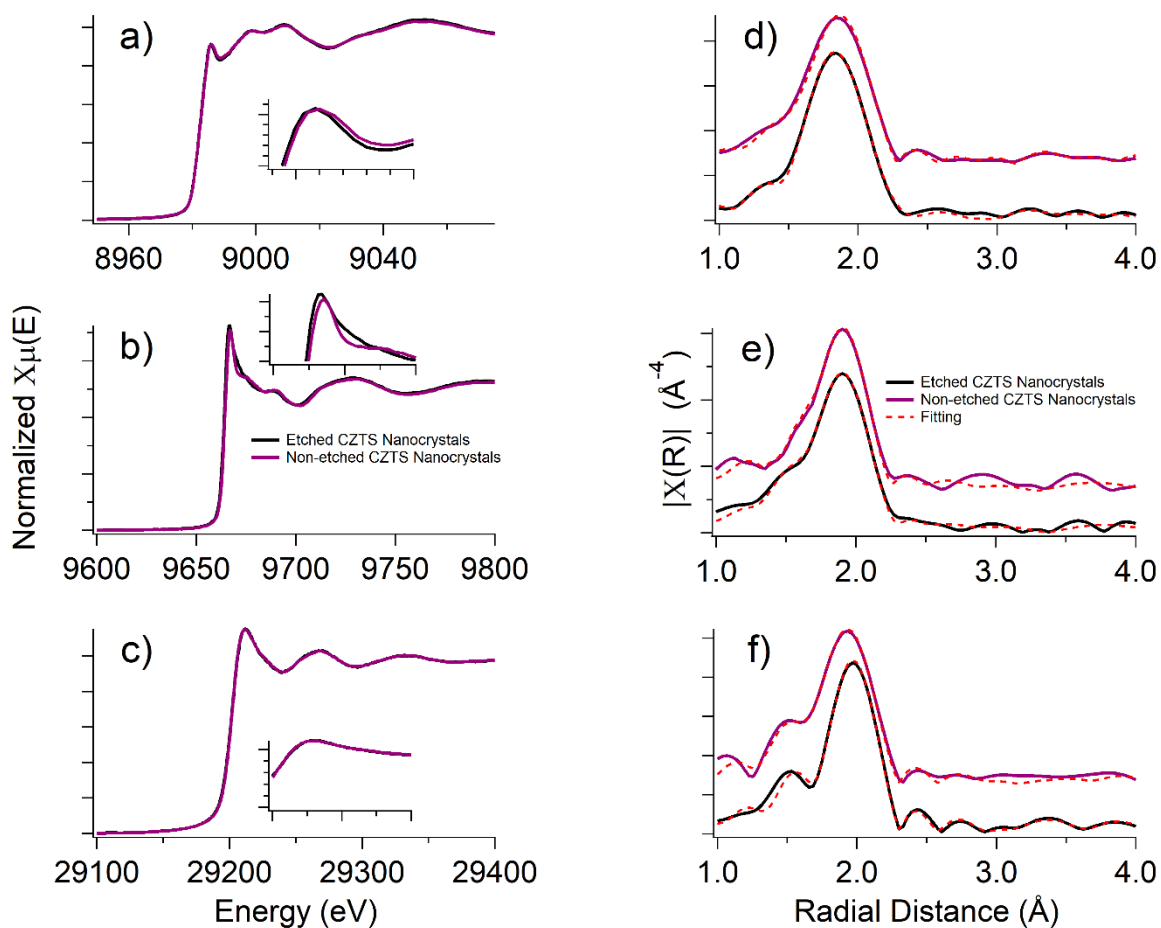


Figure 2.2: Cu, Zn, and Sn K-edge XAFS – a), b), and c), respectively – comparing the primary oxidation state and coordination sphere of the etched and non-etched CZTS NCs. Insets of the white line peak are shown for clarity. The corresponding EXAFS fitting– for Cu (d), Zn (e), and Sn (f) displays the structural shifts in bond lengths of the nearest neighbor, and the relative disorder within the NCs.

The features of the Zn K-edge XANES in Figure 2.2b display a change in the white line peak as it shifts back by 1.0 eV after etching. This suggests higher electron density on the Zn centers. This shift is clearly visible in the Figure 2.2b inset, despite the onset of the absorption being identical in both samples. This along with the fact that the Cu-center shows an increased strength in signal when etched, would manifest in a reduction in the p-type nature of the etched film, and can be confirmed through XPS in *Section 2.3.4*.

As with the Cu XANES (Figure 2.2a), the etched sample shows similar features as the non-etched yet contains more definition in the form of deeper troughs, and sharper peaks in the extended regions. This implies a close association between the Cu and Zn within the crystal structure. This relationship between these atoms forms the foundation of many of the defect structures that determine the effectiveness of the film³², and control the electronic structure of the bands.⁴ Etching is therefore an effective way of tuning the band structure of the device, cleaning the surface of the CZTS, all without altering the general chemical structure of the film.

The Sn XANES in Figure 2.2c shows much broader oscillations than either the Cu (Figure 2.2a) or Zn (Figure 2.2b) XANES, and no change in the absorbance signals, with both the etched and non-etched lines overlapping throughout. The core-hole lifetime of the Sn K-edge is most likely contributing to the observed broadness, preventing extremely fine details, such as those observed on the XANES of Cu and Zn centers.^{15, 31} The core-hole lifetimes are usually shorter in heavier elements and thus result in spectral broadening that blur out fine details in the XANES spectra.³³ Nevertheless, the conserved Sn spectra confirm the lack of oxidative, or major change in the CZTS crystal structure as a result of the etching process.

The above features were examined in finer detail by fitting the EXAFS region using a standard CZTS kesterite crystal model.^{13, 34} This is done by converting the extended region oscillations to the k-space plot of the EXAFS, and the radial distance plots through Fourier transforms. Where the k-space is the wave vector or momentum of the corresponding absorbance with respect to the background absorbance. The EXAFS fitting parameters are presented in Figure 2.2d-f.^{12, 13} The parameters of the fitting for each of the resulting plots have been tabulated in Table 2.1.

Table 2.1: EXAFS fitting parameters for each sample metal center. Each bond length has an error of less than ± 0.02 Å and are consistent within the non-etched or etched sample category. Energy shifts (E_0) were held constant for all scattering paths and were less than 2.7 eV in all cases. The amplitude reduction factor was fixed at 0.70 for the Cu K-edge, 0.90 for the Zn K-edge, and 1.00 for the Sn K-edge EXAFS fitting, with each determined by measuring the metal reference foil and fitting the metal-metal bond distance. N is the degeneracy of the pathway, σ^2 is the mean squared displacement of half the path-length and r is the interatomic distance.

Edge	Neighbor	Non-etched Sample			Etched Sample		
		N	σ^2 (Å ²)	r (Å)	N	σ^2 (Å ²)	r (Å)
Cu	S (short)	0.0	---	---	0.7	0.00459	2.286
	S (long)	4.0	0.00668	2.312	3.3	0.00459	2.332
	Cu/Zn	4.0	0.00840	3.799	4.0	0.00795	3.801
	Sn	4.0	0.01302	3.905	4.0	0.01163	3.900
Zn	S (short)	0.1	0.00255	2.270	0.6	0.00255	2.269
	S (long)	3.9	0.00255	2.321	3.4	0.00255	2.324
	Cu/Zn	4.0	0.01013	3.817	4.0	0.00896	3.797
	Sn	4.0	0.00952	3.929	4.0	0.01330	3.885
Sn	S (short)	0.6	0.00844	2.259	0.6	0.00413	2.256
	S (long)	3.4	0.00844	3.309	3.4	0.00413	2.337
	Cu/Zn	4.0	0.01041	3.872	4.0	0.00951	3.830
	Sn	4.0	0.01672	4.007	4.0	0.01348	3.919

The Cu EXAFS (Figure 2.2d) of both etched and non-etched samples share many of the same features as the XANES spectra and have a similar fit. The only major difference comes in the disorder observed in the first nearest neighbor peak, which corresponds to the Cu-S bond. In the non-etched sample, this peak is weaker, and slightly broader than that of the etched sample. The additional broadening in the peak leads to a far better fit with a single Cu-S bond length. The etched sample can be broken down more effectively and determine both a short and long Cu-S bond as seen in Table 2.1. This could be due to the two distinct Cu sites of the film.

Very interestingly, two different metal-sulfur bond lengths yield better fits for both the Zn (Figure 2.3e), and Sn (Figure 2.2f) metal centers, that do not have two distinct lattice positions. The two-bond length feature suggests that the different bond lengths represent a range into which the various NCs in the film fall. The narrower this gap, the more uniform the film, and thus the higher the expected efficiencies. If the disorder is high, the EXAFS will show a singular broadness in the peak, as has been reported in the past, obscuring this difference.³⁵ The above observation also explains the Cu-S bond distance of the non-etched sample being nearly right between the two distances reported for the etched sample.

The Zn fits (Figure 2.2e) follow much of the same trend as Cu fits, with high similarity between the bond distances reported in the non-etched and etched samples. The non-etched Zn-S can be broken down into the short and long distance; however, the association is very weak, and the associated ratio of long to short bonds is much less pronounced, at 3.9 : 0.1, than in the etched, which shows a similar ratio to the Cu spectra, at 3.4 : 0.6. Despite the discrepancy, the delineation is still clearer than in the Cu spectra. The increased Cu signal in the non-etched film is indicative of a decrease in p-type character, further confirming that the etching process predominantly affects the Cu environments as it decreases the Cu signal to increase the p-type character.

The Sn fits (Figure 2.2f) do not show much deviation between the etched and non-etched samples, due to the previously noted core-hole lifetime broadening of the K-edge signal. The fits are therefore highly similar between the non-etched and etched samples. Despite this, it should be noted that the reported bond distances of the etched sample more closely

resemble the values suggested by the Cu and Zn fitting, and therefore offers additional support to the assertion that the etched samples have additional uniformity in addition to the removal of unwanted surface insulator states.

2.3.3 Energy band gap analysis

Figure 2.3 shows a Tauc Plot conversion of UV-VIS absorption where the charge transfer through a film can be examined and from this, the energy band gap can be extrapolated. These plots were made for bulk CdS, etched and non-etched CZTS NCs. Linear extrapolation of the plot shown in Figure 2.3 provides the energy band gap for the material being measured.

The non-etched CZTS NCs, outlined in purple, has a larger band gap energy at 1.52 eV which is above the excitation energies of the intense region. Once the insulator layer is etched from the surface of the film, the CZTS NCs, outlined in black in Figure 2.3, decreases to an optimal band gap of 1.45 eV resembling excitation energies of the solar spectrum where it is the most intense.³⁶ The bulk CdS, outlined in blue, has an optimal band gap energy of 2.21 eV which is quite large, however beneficial to the interface. By having a larger band gap energy for the buffer layer, photons will be able to reach the NC light-absorbing layer and prevent backflow of charges, thereby increasing the shunt resistance to prevent the loss of electrons to alternate pathways within the device.

This is the result of an ideal energy gap between the valence band of CZTS and CdS to facilitate the transfer of electrons without loss.¹⁴ The final device efficiency is determined by how effective the transfer of electrons is across the CZTS/CdS interface as well as the charge flow through each layer of the device. Hence, alignment of conduction bands is essential, especially at the interface to avoid large energy barriers and any decrease in the device performance. Obtaining a tunable band gap energy is thus important to control an ideal conduction band offset (CBO) between the interface to in turn enhance device performance.³⁷

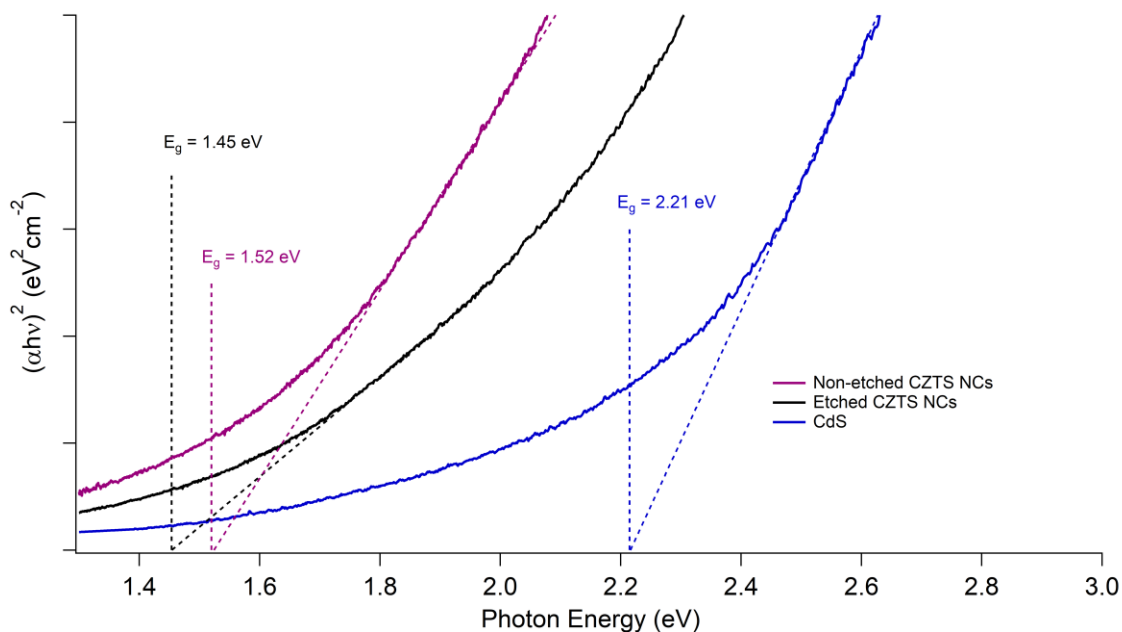


Figure 2.3: Tauc plots of the UV-VIS absorbance showing the optical band gap for the etched, non-etched CZTS NC film as well as the CdS layer.

2.3.4 Synchrotron XPS of the CZTS/CdS interface

A similar trend to the Tauc plots in Figure 2.3 can be seen in Figure 2.4 for the valence band energies where etching the films decreases the energies measured. In order to create a band diagram for the interface, the valence band energies must also be obtained to calculate the CBO as demonstrated by the *Green* and *Hao* groups in their investigations on co-sputtered CZTS solar cells and solution precursor processed cells on flexible substrates.^{4,38} The valence band binding energies were measured relative to the fermi level of a clean molybdenum film.

Referring back to Figure 2.1, the PECMs had an enhanced photoresponse if the films were etched (Figure 2.1c and d). This was also shown to have structural implications, seen in the XANES (Figure 2.2 a-c) and in the EXAFS (Figure 2.2 d-f). As such, the etching creates a beneficial structure at the film surface. To further characterize this structure, synchrotron XPS was used. This technique can examine the valence band structure, as well identify insulator layer inhibiting conductive properties. The advantage of SR-XPS over Ultraviolet Photoelectron Spectroscopy (UPS) is the capability of ionizing core electrons and can be

both bulk and surface sensitive. SR has a higher brilliance than desktop UPS and therefore, due to the higher density of photons, the signal-to-noise ratio is enhanced. Figure 2.4 shows the onset valence band energy for non-etched CZTS, etched CZTS, bulk CdS, non-etched as well as etched CZTS NC/CdS interface. The linear extrapolation to the binding energy edge for the valence band energy onset follows the method of *Chambers et al.*^{39,40} Linear extrapolation is more accurately done on SR-XPS data rather than UPS due to its higher signal-to-noise ratio.

The interfaces were carefully fabricated by only depositing a 2 nm thick CdS film, instead of the 50 nm on the CZTS NC films, to assure probing into the CZTS NC/CdS NCs. The etched bulk CZTS layer shown in Figure 2.4a has valence band energy onset of 0.63 eV whereas, the non-etched bulk CZTS layer has the lowest energy onset at 0.55 eV show in Figure 2.4b. Similarly, the non-etched CZTS NC/CdS interface in Figure 2.4d, has a higher energy onset at 0.94 eV compared to the etched interface at 0.88 eV displayed in Figure 2.4e. The bulk CdS valence band energy (E_{VB}) (Figure 2.4c), is the highest among the measured films at 1.44 eV which is 0.50 eV more than the non-etched CZTS NC/CdS interface and 0.56 eV more than the etched CZTS NC/CdS interface. This generates a shallow valence band energy for CdS which, as previously mentioned, is beneficial in facilitating electron transfer and alignment of the conduction and valence bands at the film interface.⁶

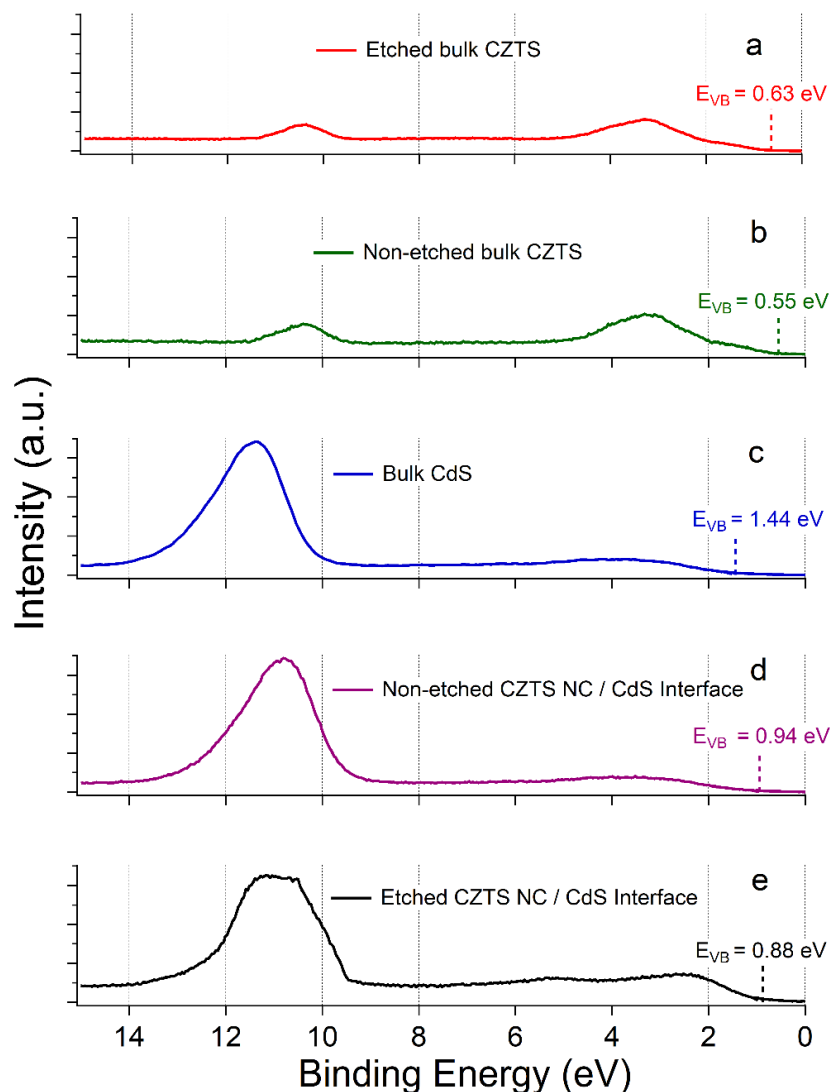


Figure 2.4: XPS plots of the valence band energy for the non-etched CZTS (a), etched CZTS (b), bulk CdS (c), non-etched CZTS NC/CdS interface (d) and the etched CZTS NC/CdS interface (e). Linear extrapolation of the leading edge marks the E_{VB} .

If there is a large gap between the valence bands, the back flow of charges is reduced and thus capacitance is increased – this will further increase band bending at the film’s interface as reported on MoS₂ interfaced with other materials.²⁶ In an ideal solar cell, a charge is released once a photon hits the p-n junction; however, for CZTS, any impurity or defect in the lattice is capable of holding a charge hence, it not being conductive. Similarly, the band

structures were established as shown in Figure 2.5, where the difference in conduction bands (EB_{CB}) and valence bands (EB_{VB}) were measured at the interface using synchrotron XPS.

The E_{VB} for the interface with etched bulk CZTS (Figure 2.4e) shifts to a lower energy with greater resolution of peaks than the one with non-etched CZTS (Figure 2.4d) thanks to the removal of the surface insulator layer by post-process etching. This lower energy shifts in the bulk CZTS (Figure 2.4b) and interface after etching is indicative of a film with more p-type character, and once again proves that etching the substrates and films is beneficial to the structure of the crystalline film. This is further exemplified in the band structure, where several peaks are able to be distinguished from 2 to 5 eV, unlike the non-etched interface and non-etched bulk CZTS (Figure 2.4a).

In Figure 2.4, the etched interface indicates that this film has the most ordered structure and is likely to favour the transfer of charge across the interface instead of other inhibiting processes. The improvement in the interface clarifies why there was an increase in photoresponse in Figure 2.1c and d. In addition, etching proves to be beneficial in returning the amount of copper and reducing the amount of oxygen present in the bulk CZTS film in prolonged atmospheric exposure time. This was also calculated by desktop XPS; the atomic percentages of the elements over time can be found in Table 2.2.

Table 2.2: Time study of the effect of prolonged atmospheric exposure time on the CZTS film along with the effect of etching with acetic acid. The rows of exposure time and etching processes are in chronological order and thus, the total exposure time of the films is two months. Atomic percentages of elements are listed with the primary focus being on the Cu 2p, Zn 2p, Sn 3d and O 1s.

	Non-etch %	Etch %	1 week out %	3 weeks out %	Etch %	1 week out %	3 weeks out %
C 1s	64.79	52.22	76.93	72.06	53.39	77.87	74.02
N 1s	4.26	3.53	1.44	2.00	3.26	2.50	2.04
O 1s	9.11	10.05	14.58	21.08	10.23	11.96	18.64
S 2p	12.81	12.87	4.03	2.45	12.31	5.12	2.30
Cu 2p	3.81	9.84	1.18	0.90	10.23	0.79	1.18
Zn 2p	2.24	7.94	0.83	0.71	7.06	0.74	0.93
Sn 3d	2.98	3.54	1.00	0.80	3.53	1.02	0.89

The effects of etching can be observed by the atomic percentages of copper, zinc and oxygen over time, which were measured by a desktop XPS instrument. The amount of copper in a non-etched film starts at 3.8%; when etched the amount of copper returns to 9.8%. When the film is left in ambient conditions over time, the amount of oxygen on the surface starts to increase while the copper decreases— noted by the increase from 9.1% to 10.1% in oxygen and the decrease from 9.8% to 14.6% in copper in one week. This trend continues as the copper reduces to 0.9% while the oxygen increases to 21.1% when left out for a cumulative three weeks. When the film is then etched with acetic acid, many of the oxides that produce the insulator layer were greatly reduced. This is seen by the drastic return of copper and reduction of oxygen to both 10.2%. It is important to note that this has

returned to same amount copper and oxygen after a month of fabrication. A similar trend between zinc and oxygen can be seen as the zinc returns to its non-etched amount after a month of fabrication. The time study continued for another month confirming the downwards trend in metals and increase in oxygen when left out in ambient conditions. This proves that up to two months after fabrication, etching proves to be beneficial in returning metals to their original atomic percentages within the film.

2.3.5 Formation of the P-N junction

In an effective p-n junction, the conduction band of the CdS must lie slightly above that of the CZTS within the SCR, creating a small energy barrier for the electrons to overcome. This is referred to as a spike-like energy barrier which ensures maximum charge-carrier flow, avoids electron-hole recombination at the interface and maintains a high open-circuit V_{OC} .^{14, 38} Additionally, the valence band of the buffer layer must not be in proximity to that of the CZTS to further prevent backflow of charges and recombination.⁴¹ The measurements for the band structure are done through the cooperative use of UV-VIS spectroscopy and synchrotron x-ray spectroscopies.²⁷

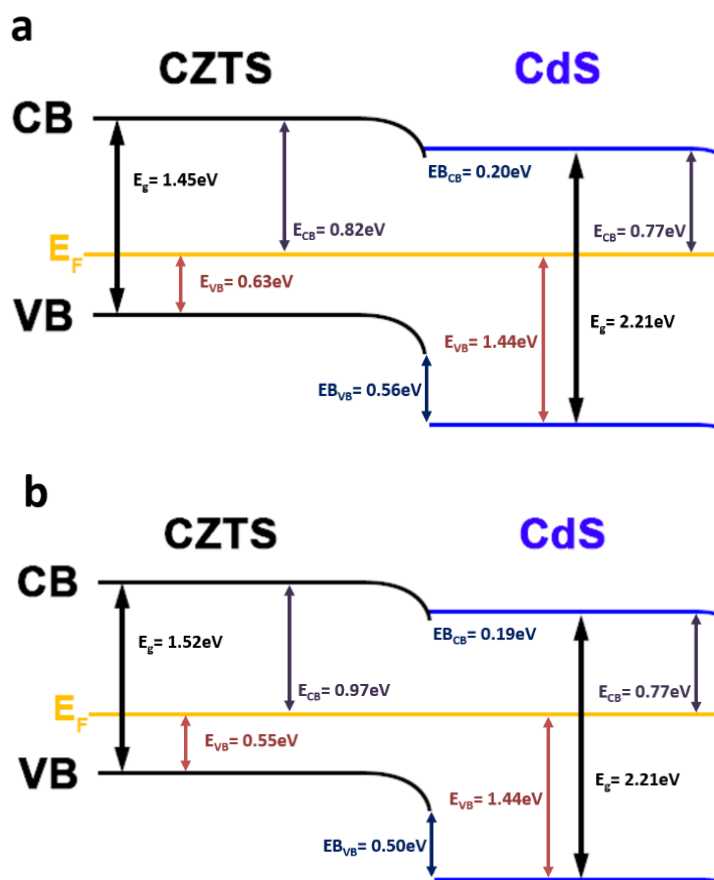


Figure 2.5: Energy band diagram for the a) etched and b) non-etched CZTS-CdS interface; the relative fermi level has been marked as E_F . Both configurations resemble a spike-like barrier at the interface.

A band diagram of the etched versus non-etched CZTS and CdS semiconductors at the interface is shown in Figure 2.5, which was constructed using the energy values from Figures 2.3 and 2.4. It was determined that the CZTS NC layer has a band gap of 1.45 eV with the E_{VB} 0.63 eV below the fermi level and the E_{CB} 0.88 eV above the fermi level in the etched sample. The non-etched CZTS NC layer has a band gap of 1.52 eV with the E_{VB} 0.55 eV below and the E_{CB} 0.97 eV above the fermi level. The energy band gap for the CdS layer was 2.21 eV with the E_{VB} 1.44 eV below and the E_{CB} 0.77 eV above the fermi level respectively. As such, both etched and non-etched CZTS layers display p-type character, and the CdS displays n-type character. This results in a reduced CBO in the space charge region.

$$EB_{CB} = |E_g^{CZTS} - E_g^{CdS} + EB_{VB}| \quad (2.1)$$

A space charge region of a p-n junction was formed with the CZTS and CdS films once in contact. Figure 2.5 shows a spike-like barrier thanks to the reduced CBO in both the etched and non-etched cases which creates an ideal space charge region. There are two configurations for the gap between the conduction bands: spike-like barrier and cliff-like barrier in CZTSe and CZTS solar cells that are prepared in varied conditions.^{32, 42} Using *equation 2.1*, the configuration for the gap between conduction bands (EB_{CB} or CBO) can be determined where EB_{VB} is the gap between the valence bands and E_g is the band gap energy for the CZTS or CdS layer.⁴ As illustrated in Figure 2.5, there is a spike-like barrier of 0.20 eV and 0.19 eV in both cases of the etched and non-etched films respectively.

The small energy barrier must be overcome by the promoted electron for it to flow from the CZTS conduction band into the CdS one. These barrier values are ideal since a barrier greater than 0.40 eV would be too large for the electron to overcome as summarized in a report on CZTSSe/CdS interfaces grown via vacuum-based and solution-based deposition methods.⁴³ Obtaining a CBO value between 0 and 0.40 eV yields the most apt band alignment for the absorber layer/ buffer layer interface.^{44, 45} A spike-like barrier prevents electron-hole recombination at the interface, increases open circuit potential and short circuit current. A cliff-like barrier simply drops down electrons from one conduction band into the other. This is undesirable as it causes the electrons to undergo an energy decay in order for it to drop down from one CB into the other, which will also reduce the potential generated across the different layers. This results in a decrease in the space charge region and thus also a decrease in the open circuit potential.^{46, 47}

In previous studies where the light-absorber-layer was electrodeposited, the non-etched interface displayed a CBO larger equal to or larger than 0.40 eV, a cliff-like barrier, and needed to be tuned by other means first.²⁸ NC films provide benefits in this important aspect as it always creates a spike-like barrier within the 0-0.4 eV range. This type of barrier also indicates that there is an ideal CBO at the interface. Therefore, both setups maintain a strong electric field, and as aforementioned, produce high open circuit photopotentials and larger short circuit currents. The increased photopotentials and currents are due to the high

density of charges in the space charge region, which creates a larger internal bias, and thus enhances charge-carrier flow from the CZTS NC layer to the CdS layer.

This benefits the effectiveness of charge flow, counter to what is mentioned in other studies.⁴ From Figure 2.5, the spike-barrier values (EB_{CB}) and conduction band energies (E_{CB}) are 0.20 eV and 0.82 eV respectively for the etched sample which is similar to the non-etched sample with an EB_{CB} and E_{CB} of 0.19 eV and 0.97 eV respectively. Due to the similarity in energies, it is not evident how etching provides benefit to the electronic configuration. However, referring to the PECMs in Figure 2.1, the photoresponse without etching is significantly lower. This is hypothesized to be a result of an air barrier created with the addition of CdS during deposition without the removal of oxides.⁴⁸ The importance of nanocrystals is the fact that configuration of the interface is always a spike-like barrier, but etching is still beneficial to the performance as the electron density is increased at the surface. This is consistent with metal ion loss.

2.3.6 Full device analysis

Solar devices were completed after the deposition of both window layers, 50 nm of ZnO and 250 nm of AZO via ALD. J-V curves were measured on a 0.10 cm² area scribed by a razor blade to test the performance of full devices, with the champion cells shown below in Figure 2.6a and b. The full device with etched CZTS NC film in Figure 2.6a shows an open circuit potential (V_{OC}) of 0.85 V which is significantly higher than any reported to date for CZTS and CdS nanocrystal film devices.^{7, 49} This is due to the etching of the insulator layer as proven by the band diagram in Figure 2.5a. In contrast, the non-etched device in Figure 2.6b shows a much lower open circuit potential at 0.17 V. This is likely due to charge traps and recombination by oxides at the CZTS/CdS interface.

The observation was predicted by the band diagram in Figure 2.5 as well as the PECMs in Figure 2.1, since effective charge carrier flow at the interface was dependent on whether the film was etched or not. In a band offset model, when the CBO is more negative, the electric field at the junction relaxes and in turn can reduce the V_{OC} . However, if the CBO is more positive the internal bias can expand the depletion region, thereby the V_{OC} is predicted to increase.⁵⁰ As etching reduced the CZTS NC energy band gap, the CBO

resulted in being more positive and lead to a more “spike-like” barrier at the interface. This validates the fact that a good alignment between the two conduction bands results in a higher V_{OC} to the condition of less charge-carrier recombination.

The short-circuit current (I_{SC}) for the etched device shows to be 20.0 mA/cm^2 , with a Fill Factor (FF) of 0.46. This is fairly high for NC film devices and is confirmed by the predicted results of the PECMs whereas the short circuit current for the non-etched device is considerably lower at 5.10 mA/cm^2 with a FF of 0.34. Two parameters that efficiency is dependent on are the I_{SC} and V_{OC} at the maximum current and voltage respectively. At each of these points, the power is zero, hence, the Fill Factor (FF) is calculated to determine the maximum power as a product of V_{OC} and I_{SC} and is defined as the maximum “squareness” achieved in a J-V curve for a solar cell.^{22, 29, 51}

The slope in the curve that leads from the V_{OC} and I_{SC} to the maximum power is suggestive of shunt and series resistance, respectively. It has usually been a problem for the V_{OC} as the slope should be minimal. A low shunt resistance proposes that electrons are flowing through alternative pathways through the film instead of through the fabricated circuit and thus current bleeds from different areas of the device causing I_{SC} to decrease.^{29, 52} The series resistance might be caused by lack of interaction with the metal back-contact of the device during fabrication and thus altering the conducive properties of the metal which ultimately lead to a decrease in FF.¹³

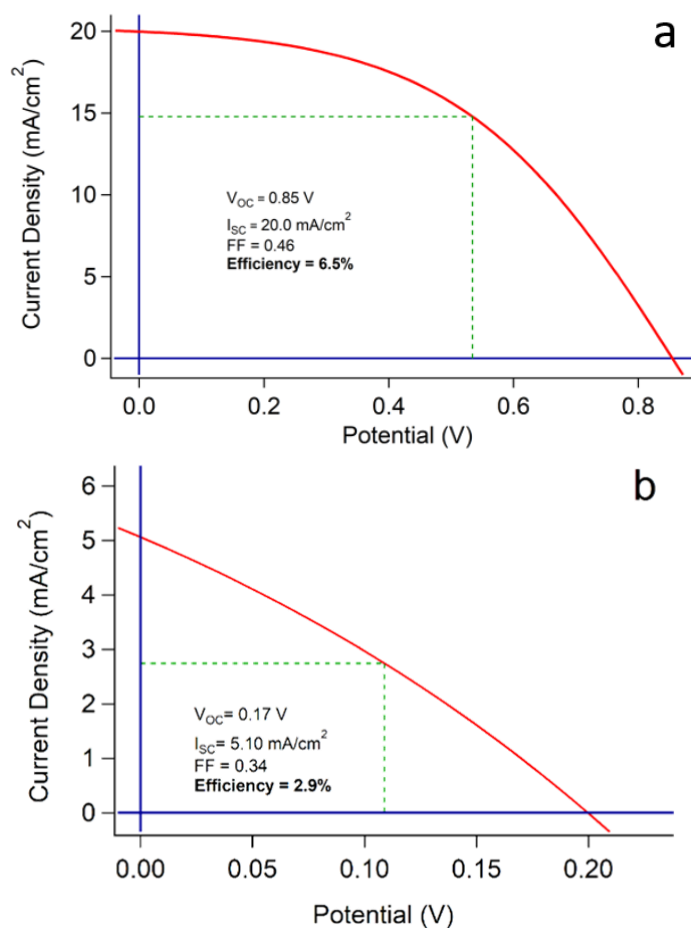


Figure 2.6: J-V curve for a champion full device of a) an etched film and b) non-etched film. The current and voltage at maximum power are indicated by the dashed lines used to calculate Fill Factor.

In previous studies for CZTS based films, shunt resistance – the slope of the line leading from the I_{SC} point – was very high, and thus did not detract from the power output of the device. In the NC-based devices herein, there is a decreased shunt resistance relative to the ideal, which causes a considerable loss of power. In the non-etched devices, the slope leading from I_{SC} to V_{OC} almost resembles a straight line, which suggests that most of the problem results from reduced shunt resistance, and not high series resistance. This indicates that there are alternate pathways for electrons to take within the non-etched films, counter to the desired one, leading to a decreased efficiency. When the CZTS NC film is etched, this improves noticeably, but there is still much of a curve from the I_{SC} to the P_{max} point,

where the dashed green lines meet the red J-V curve in Figure 2.6. This is a result of the lack of uniformity in the NC film and thus current would not be continuous between each cluster of crystals.

Solar cell efficiency is dependent on the I_{SC} , V_{OC} and FF in a non-resistive film. The above values led to a substantially increased efficiency of the working device based on etched CZTS NCs at 6.5% which is high for CZTS NC film devices, whereas, the efficiency for non-etched device is about half that at 2.9%. It can then be concluded that non-etched CZTS NCs are prone to defects at the interface which lead to a decrease in photoresponse and shunt resistance, ultimately lowering the device performance and efficiency.

Table 2.3: Range of characteristic parameters of J-V curves, measured over ten full devices for non-etched CZTS NCs and etched CZTS NCs.

	Efficiency (%)	Voc (V)	FF	Jsc (mA/cm ²)
Non-etched CZTS NCs	0.42 – 2.9	0.17 – 0.84	0.26 – 0.35	0.96 – 5.6
Etched CZTS NCs	1.6 – 6.5	0.48 – 0.85	0.34 – 0.46	6.1 – 20.0

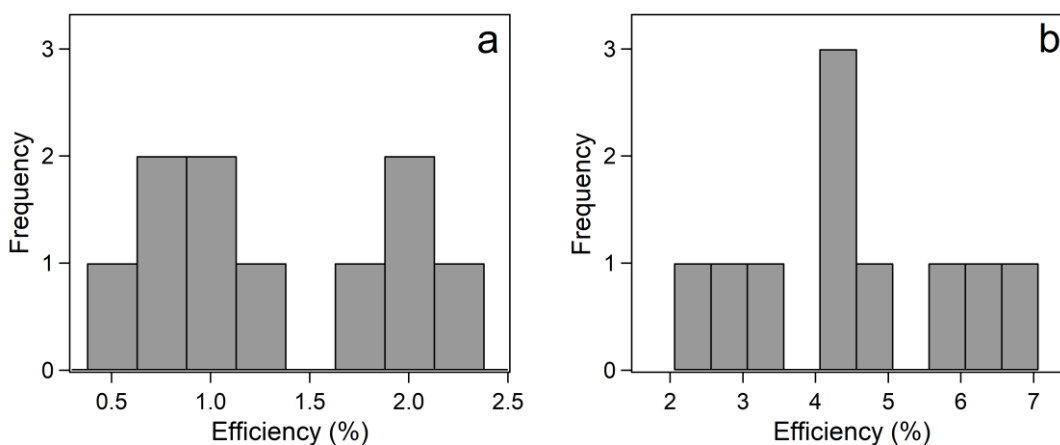


Figure 2.7: Efficiency histograms for: a) NE CZTS NCs and b) E CZTS NCs.

Characteristic parameters for J-V curves of ten full devices for both non-etched and etched devices were measured, and the statistics of each parameter were summarized in Table 2.3 and shown in Figure 2.7. The performances of the champion devices are lower than laboratory efficiencies for CZTS. Disparity in device efficiency may lay in the deposition method of the CZTS light-absorber-layer. Many studies with highly efficient devices in literature, involve magnetron or co sputtering precursors.^{4, 5, 7, 52} In literature, many studies also do not involve surface treatments other than DIW preferential etching or KCN for removal of surface impurities.^{5, 53} However, the champion etched device in Table 2.3 is more efficient than devices in literature comprised of CZTS nanocrystals.^{54, 55-56} The synthesis of the nanocrystals and deposition of the nanoparticle ink still vary from this study which speaks well to the electrophoretic deposition technique applied in this chapter.

Despite the etched champion device surpassing the nanocrystal efficiencies in literature, the range of efficiencies over ten devices is broad. A wide range for both etched and non-etched devices expresses a concern in reproducibility of devices from light-absorber-layers comprised of nanocrystal ink. Additionally, the same concern with the range of V_{OC} over ten devices is apparent. As reproducibility is lowered, so is the scalability of these devices which is important for future devices. Many studies that incorporate nanocrystals into the absorbing film also include high temperature selenization to anneal the film as selenium is shown to be more efficient than pure sulfide films.^{17, 36} A pure sulfide nanocrystal film without any annealing step has shown to struggle in high device efficiency due to low grain growth and so an alternative technique may be needed to advance a CZTS solar cell.^{49, 57} Another technique that has been successful in producing a highly efficient CZTS based device is electrodeposition as studied by *Ahmed et al.*³⁴

2.3.7 Characterization of ED CZTS layers

Until now, nanocrystals for the absorbing film have proven to be thermodynamically favourable and beneficial to the energy band diagram. However, issues arise with scalability for future devices as it is not as easily reproducible as other deposition techniques. Electrodeposition is still an inexpensive deposition technique, as well as an easily reproducible and scalable technique for future devices. Thus, it is a technique worth exploring and improving upon compared to the nanocrystal-based layer. In previous work,

the CBO between the interface was found to be naturally cliff-like but etching the devices proved to tune it to a spike-like barrier.¹⁰ Annealing with heat after the addition of CdS or the post-process etching was done to remove any water intercalation that may have occurred. Modifications to this procedure involve varying times and temperatures for the sulfurization and CdS procedures.

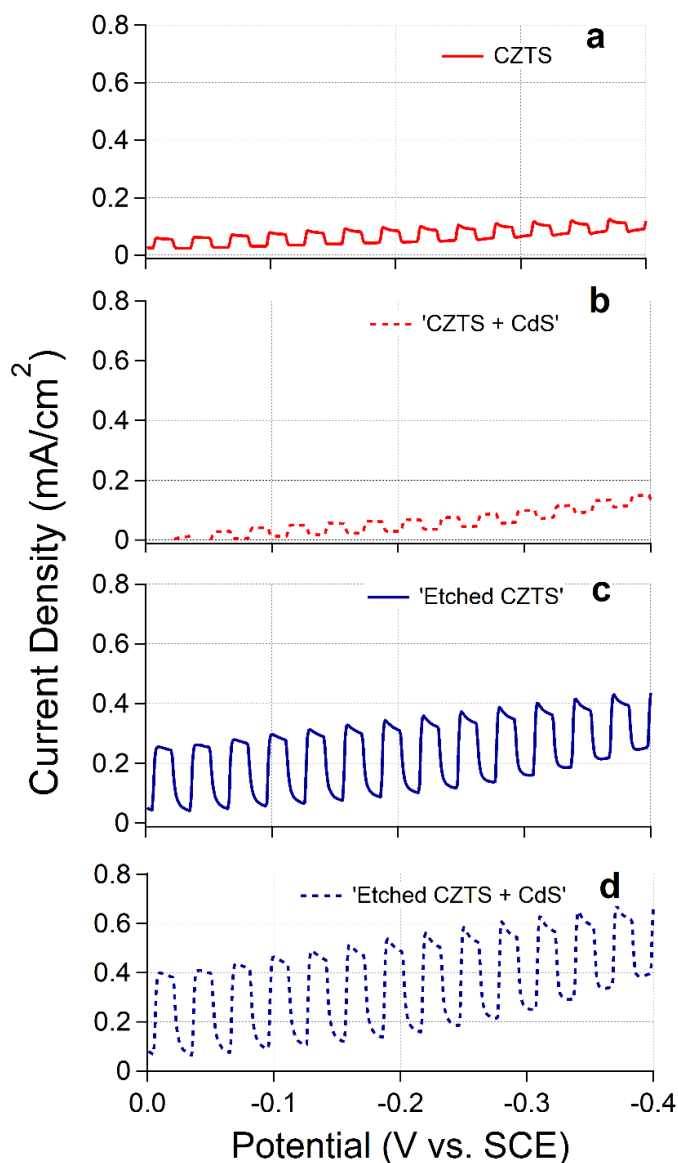


Figure 2.8: PECMs of non-etched ED CZTS films a) before and b) after CdS coating as well as etched ED CZTS films c) before and d) after CBD of CdS. Etching was processed using glacial acetic acid for 30 min.

Figure 2.8 demonstrates preliminary PECMs of intrinsic ED CZTS film before (Figure 2.8a) and after (Figure 2.8b) the addition of the CdS buffer layer as well as acetic acid etched ED CZTS films before (Figure 2.8c) and after (Figure 2.8d) the CdS coating. Similar to the CZTS NCs, there is an increase in current density upon illumination to 0.07 mA/cm^2 in Figure 2.8a. This is much lower than the champion film for the CZTS NC but has not been optimized as of yet. The gradual decrease in current density before the ‘light off’ scenario suggest that while there is primarily product separation of the charges, recombination under illumination still occurs. In the absence of light, recombination of charges should occur, and the current density is observed to drop instantaneously, meaning there is no continued product separation. Once again similar to the NCs, there is a shift from a Schottky junction to an Ohmic one over the course of the scan as there is a gradual increase in the dark current.

Once the buffer CdS layer is added (Figure 2.8b), the maximum photoresponse decreases significantly to an average of 0.04 mA/cm^2 . Recombination of charges is also less prominent in the ‘light on’ situation as the current is held steady. The dark current continues to increase as the scan progresses and the amplitude of the photogenerated current is reduced once the buffer layer is added, which follows the same trend as the nanocrystals. Acetic acid was then used to etch the surface of the cells to enhance charge-carrier flow. This proved to be beneficial as the current density increased to a maximum of 0.25 mA/cm^2 (Figure 2.8c) from the original 0.07 mA/cm^2 upon illumination.

When the buffer layer was added upon the etched film, the photoresponse amplified to a maximum of 0.45 mA/cm^2 (Figure 2.8d). For both Trace c and d, there is still recombination of charges in the light and continued product separation in the absence of it but due to the enhanced amplitude of photoresponse we can conclude that post-process etching is beneficial to electron transfer between the layers. This is now true for both CZTS NCs and ED CZTS for the light-absorber-layer. The maximum photoresponse for all four samples of the ED CZTS is significantly lower than the champion CZTS NCs, therefore, a great deal of optimization is required to refine the fabrication process and enhance the performance of the cell.

2.4 Conclusions

The CZTS NC/CdS p-n junction was explored through the use of photoelectrochemistry and x-ray absorption spectroscopy. CZTS NCs were synthesized via a solvothermal method and electrophoretically deposited on to Mo-coated substrates. It was discovered that films etched with glacial acetic acid enhanced charge-carrier flow and photoresponse due to the removal of insulating oxides on the surface. XANES displayed a reduction in p-type character of the NCs after post-process etching and through EXAFS, it was determined that Cu_xS impurities were less present in etched films. The addition of the CdS layer on an etched CZTS layer yielded an increase in photoresponse as a result of reduced E_{VB} which prevented the backflow of charges.

Post-process etching of the CZTS NC film also displayed a shift in band gap energy towards the most intense region of the solar spectrum. The p-n junction in both the etched and non-etched scenario attained a spike-like barrier and similar E_{BCB} values. The importance of a spike-like barrier is the insurance of a strong internal bias that favours the movement of charge carriers across the films. The etched CZTS NC device had a high V_{OC} of 0.85 V and an I_{SC} of 20.0 mA/cm^2 , whereas the V_{OC} and I_{SC} in non-etched devices were reduced significantly to 0.17 V and 5.10 mA/cm^2 respectively. In agreement with the PECMs, these resulted in device efficiencies of 6.5% and 2.9% respectively.

Due to the wide range in device efficiencies, another deposition technique was sought out. Electrochemical deposition of stacked metallic layers followed by high-temperature sulfurization was explored as another low-cost method to produce CZTS films. PECMs of ED CZTS showed similar trends to that of CZTS NCs as photoresponse was enhanced when the film was etched and CdS was added. The absolute value of photoresponse for ED CZTS is lower than that for CZTS NCs, however, this low-cost method would allow for controllable formation of the layer that may increase homogeneity of the film. Further enhancements of this technique should focus on reducing series resistance, thereby increasing film performance and device efficiency.

2.5 References

1. Gao, S.; Jiang, Z.; Wu, L.; Ao, J.; Zeng, Y.; Sun, Y.; Zhang, Y., Interfaces of High-Efficiency Kesterite $\text{Cu}_2\text{ZnSnS}_4$ Thin Film Solar Cells, *Chinese Phys. B*, **2018**, *27*, 1-49.
2. Green, M. A.; Dunlop, E. D.; Hohl-Ebinger, J.; Yoshita, M.; Kopidakis, N.; Hao, X., Solar Cell Efficiency Tables (Version 56), *Prog. Photovolt.:Res. Appl.*, **2020**, *28*, 629-638.
3. Rakhshani, A.; Thomas, S., $\text{Cu}_2\text{ZnSnS}_4$ Films Grown on Flexible Substrates by Dip Coating Using a Methanol-Based Solution: Electronic Properties and Devices, *J. Electron. Mater.*, **2015**, *44*, 4760-4768.
4. Sun, K.; Yan, C.; Liu, F.; Huang, J.; Zhou, F.; Stride, J.; Green, M.; Hao, X., Over 9% Efficient Kesterite $\text{Cu}_2\text{ZnSnS}_4$ Solar Cell Fabricated by Using $\text{Zn}_{1-x}\text{Cd}_x\text{S}$ Buffer Layer, *Adv. Energy Mater.*, **2016**, *6*, 1-6.
5. Katagiri, H.; Jimbo, K.; Yamada, S.; Kamimura, T.; Maw, W. S.; Fukano, T.; Ito, T.; Motohiro, T., Enhanced Conversion Efficiencies of $\text{Cu}_2\text{ZnSnS}_4$ -Based Thin Film Solar Cells by Using Preferential Etching Technique, *Appl. Phys. Express*, **2008**, *1*, 1-2.
6. Mitzi, D. B.; Gunawan, O.; Todorov, T. K.; Wang, K.; Guha, S., The Path Towards a High-Performance Solution-Processed Kesterite Solar Cell, *Sol. Energy Mater. Sol. Cells*, **2011**, *95*, 1421-1436.
7. Yan, C.; Sun, K.; Huang, J.; Johnston, S.; Liu, F.; Puthen Veetil, B.; Sun, K.; pu, A.; Zhou, F.; Stride, J.; Green, M.; Hao, X., Beyond 11% Efficient Sulfide Kesterite $\text{Cu}_2\text{Zn}_x\text{Cd}_{1-x}\text{SnS}_4$ Solar Cell: Effects of Cadmium Alloying, *ACS Energy Lett.*, **2017**, *2*, 930-936.
8. Ansari, M. Z.; Khare, N., Structural and Optical Properties of CZTS Thin Films Deposited by Ultrasonically Assisted Chemical Vapour Deposition, *J. Phys. D: Appl. Phys.*, **2014**, *47*, 1-6.
9. Chen, S.; Walsh, A.; Gong, X. G.; Wei, S. H., Classification of Lattice Defects in the Kesterite $\text{Cu}_2\text{ZnSnS}_4$ and $\text{Cu}_2\text{ZnSnSe}_4$ Earth-Abundant Solar Cell Absorbers, *Adv. Mater.*, **2013**, *25*, 1-18.
10. Turnbull, M. J., Layer-by-Layer Construction Strategies Towards Efficient CZTS Solar Cells. University of Western Ontario, Electronic Thesis and Dissertation Repository, 2018.
11. Mendis, B. G.; Shannon, M. D.; Goodman, M. C. J.; Major, J. D.; Claridge, R.; Halliday, D. P.; Durose, K., Direct Observation of Cu, Zn Cation Disorder in $\text{Cu}_2\text{ZnSnS}_4$ Solar Cell Absorber Material Using Aberration Corrected Scanning Transmission Electron Microscopy, *Prog. Photovolt.*, **2014**, *22*, 24-34.
12. Zhang, P., X-Ray Spectroscopy of Gold-Thiolate Nanoclusters, *J. Phys. Chem. C*, **2014**, *118*, 25291-25299.
13. Teo, B. K., *EXAFS: Basic Principles and Data Analysis*, 1st ed.; Springer-Verlag, 1986.
14. Santoni, A.; Biccari, F.; Malerba, C.; Valentini, M.; Chierchia, R.; Mittiga, A., Valence Band Offset at the $\text{CdS}/\text{Cu}_2\text{ZnSnS}_4$ Interface Probed by X-Ray Photoelectron Spectroscopy, *J. Phys. D: Appl. Phys.*, **2013**, *46*, 1-5.

15. Stöhr, J., *NEXAFS Spectroscopy*, 1st ed.; Springer - Verlag 1992.
16. Vaccarello, D.; Tapley, A.; Ding, Z., Optimization of the $\text{Cu}_2\text{ZnSnS}_4$ Nanocrystal Recipe by Means of Photoelectrochemical Measurements, *RSC Adv.*, **2013**, *3*, 3512-3515.
17. Cao, Y.; Denny, M. S.; Caspar, J. V.; Farneth, W. E.; Guo, Q.; Ionkin, A. S.; Johnson, L. K.; Lu, M.; Malajovich, I.; Radu, D.; Rosenfeld, H. D.; Choudhury, K. R.; Wu, W., High-Efficiency Solution-Processed $\text{Cu}_2\text{ZnSn}(\text{S},\text{Se})_4$ Thin-Film Solar Cells Prepared from Binary and Ternary Nanoparticles, *J. Am. Chem. Soc.*, **2012**, *134*, 15644-15647.
18. Turnbull, M. J.; Khoshmashrab, S.; Wang, Z.; Harbottle, R.; Sham, T.-K.; Ding, Z., Controlling $\text{Cu}_2\text{ZnSnS}_4$ Photocatalytic Ability through Alterations in Sulfur Availability, *Catal. Today*, **2016**, *260*, 119-125.
19. Ong, K. H.; Agileswari, R.; Maniscalco, B.; Arnou, P.; Kumar, C. C.; Bowers, J. W.; Marsadek, M. B., Review on Substrate and Molybdenum Back Contact in CIGS Thin Film Solar Cell, *Int. J. Photoenergy*, **2018**, *2018*, 1-14.
20. Tapley, A.; Hart, C.; Vaccarello, D.; A. Love, D.; Ding, Z., Effect of Annealing on the Photoelectrochemical Behavior of CuInS_2 Nanocrystal Films, *J. Electrochem. Soc.*, **2014**, *161*, H725-H729.
21. Ravel, B.; Newville, M., Athena, Artemis, Hephaestus: Data Analysis for X-Ray Absorption Spectroscopy Using IFEFFIT, *J. Synchrotron Radiat.*, **2005**, *12*, 537-541.
22. Momma, K.; Izumi, F., Vesta 3 for Three-Dimensional Visualization of Crystal, Volumetric and Morphology Data, *J. Appl. Crystallogr.*, **2011**, *44*, 1272-1276.
23. Koningsberger, D. C.; Prins, R., *X-Ray Absorption: Principles, Applications, Techniques of EXAFS, SEXAFS, and XANES*, 1st ed.; Blackwell, 1988.
24. Katagiri, H.; Jimbo, K.; Maw, W. S.; Oishi, K.; Yamazaki, M.; Araki, H.; Takeuchi, A., Development of CZTS-Based Thin Film Solar Cells, *Thin Solid Films*, **2009**, *517*, 2455-2460.
25. Saha, S. K.; Guchhait, A.; Pal, A. J., $\text{Cu}_2\text{ZnSnS}_4$ (CZTS) Nanoparticle Based Nontoxic and Earth-Abundant Hybrid PN-Junction Solar Cells, *Phys. Chem. Chem. Phys.*, **2012**, *14*, 8090-8096.
26. McDonnell, S.; Addou, R.; Buie, C.; Wallace, R. M.; Hinkle, C. L., Defect-Dominated Doping and Contact Resistance in MoS_2 , *ACS Nano*, **2014**, *8*, 2880-2888.
27. Turnbull, M. J.; Vaccarello, D.; Wong, J.; Yiu, Y. M.; Sham, T.-K.; Ding, Z., Probing the CZTS/CdS Heterojunction Utilizing Photoelectrochemistry and X-Ray Absorption Spectroscopy, *J. Chem. Phys.*, **2018**, *148*, 1-9.
28. Bard, A. J.; Faulkner, L. R., *Electrochemical Methods : Fundamentals and Applications* 2nd ed.; John Wiley & Sons, Inc., 2001.
29. Zhuk, S.; Kushwaha, A.; Wong, T. K. S.; Masudy-Panah, S.; Smirnov, A.; Dalapati, G. K., Critical Review on Sputter-Deposited $\text{Cu}_2\text{ZnSnS}_4$ (CZTS) Based Thin Film Photovoltaic Technology Focusing on Device Architecture and Absorber Quality on the Solar Cells Performance, *Sol. Energy Mater. Sol. Cells*, **2017**, *171*, 239-252.

30. Lie, S.; Sandi, M. I.; Tay, Y. F.; Li, W. J.; Tan, J. M. R.; Bishop, D. M.; Gunawan, O.; Wong, L. H., Improving the Charge Separation and Collection at the Buffer/Absorber Interface by Double-Layered Mn-Substituted CZTS, *Sol. Energy Mater. Sol. Cells*, **2018**, *185*, 351-358.
31. Newville, M., Fundamentals of XAFS, *Rev. Mineral. Geochem.*, **2014**, *78*, 33-74.
32. Schelhas, L. T.; Stone, K. H.; Harvey, S. P.; Zakhidov, D.; Salleo, A.; Teeter, G.; Repins, I. L.; Toney, M. F., Point Defects in $\text{Cu}_2\text{ZnSnSe}_4$ (CZTSe): Resonant X-Ray Diffraction Study of the Low-Temperature Order/Disorder Transition, *Phys. Status Solidi B*, **2017**, *254*, 1-7.
33. D'Angelo, P.; Migliorati, V.; Persson, I.; Mancini, G.; Longa, S. D., Quantitative Analysis of Deconvolved X-Ray Absorption near-Edge Structure Spectra: A Tool to Push the Limits of the X-Ray Absorption Spectroscopy Technique, *Inorg. Chem.*, **2014**, *53*, 9778-9784.
34. Ahmed, S.; Reuter, K.; Gunawan, O.; Guo, L.; Romankiw, L.; Deligianni, L., A High Efficiency Electrodeposited $\text{Cu}_2\text{ZnSnS}_4$ Solar Cell, *Adv. Energy Mater.*, **2012**, *2*, 1-7.
35. Turnbull, M. J.; Vaccarello, D.; Yiu, Y. M.; Sham, T.-K.; Ding, Z., Identifying Barriers to Charge-Carriers in the Bulk and Surface Regions of $\text{Cu}_2\text{ZnSnS}_4$ Nanocrystal Films by X-Ray Absorption Fine Structures (XAFSs), *J. Chem. Phys.*, **2016**, *145*, 1-11.
36. Guo, Q.; Ford, G. M.; Yang, W.-C.; Walker, B. C.; Stach, E. A.; Hillhouse, H. W.; Agrawal, R., Fabrication of 7.2% Efficient CZTSSe Solar Cells Using CZTS Nanocrystals, *J. Am. Chem. Soc.*, **2010**, *132*, 17384-17386.
37. Khoshmashrab, S.; Turnbull, M. J.; Vaccarello, D.; Nie, Y.; Martin, S.; Love, D. A.; Lau, P. K.; Sun, X.; Ding, Z., Effects of Cu Content on the Photoelectrochemistry of $\text{Cu}_2\text{ZnSnS}_4$ Nanocrystal Thin Films, *Electrochim. Acta*, **2015**, *162*, 176-184.
38. Sun, K.; Huang, J.; Yan, C.; Pu, A.; Liu, F.; Sun, H.; Liu, X.; Fang, Z.; Stride, J. A.; Green, M.; Hao, X., Self-Assembled Nanometer-Scale ZnS Structure at the CZTS/ZnCdS Heterointerface for High-Efficiency Wide Band Gap $\text{Cu}_2\text{ZnSnS}_4$ Solar Cells, *Chem. Mater.*, **2018**, *30*, 4008-4016.
39. Chambers, S. A.; Droubay, T.; Kaspar, T. C.; Gutowski, M., Experimental Determination of Valence Band Maxima for SrTiO_3 , TiO_2 , and SrO and the Associated Valence Band Offsets with Si(001), *J. Vac. Sci. Technol., B*, **2004**, *22*, 2205-2215.
40. Scott, J.; Martinez-Gazoni, R.; Allen, M.; Reeves, R., Optical and Electronic Properties of High Quality Sb-Doped SnO_2 Thin Films Grown by Mist Chemical Vapor Deposition, *J. Appl. Phys.*, **2019**, *126*, 1-8.
41. Bard, A. J.; Faulkner, L. R., *Electrochemical Methods: Fundamentals and Applications*, 2nd Edition, Wiley Textbooks, 2000.
42. Jewell, L.; Rocco, S.; Bridges, F.; Carter, S. A., Local Structure Studies of as-Made $\text{Cu}_2\text{ZnSnS}_4$ Nanoparticles, *Phys. Rev. Applied*, **2017**, *7*, 1-12.
43. Haight, R.; Barkhouse, A.; Gunawan, O.; Shin, B.; Copel, M.; Hopstaken, M.; B. Mitzi, D., Band Alignment at the $\text{Cu}_2\text{ZnSn}(\text{S},\text{Se})_4/\text{CdS}$ Interface, *Appl. Phys. Lett.*, **2011**, *98*, 1-3.

44. Khemiri, N.; Chamekh, S.; Kanzari, M., Properties of Thermally Evaporated CZTS Thin Films and Numerical Simulation of Earth Abundant and Non Toxic CZTS/Zn(S,O) Based Solar Cells, *Solar Energy*, **2020**, *207*, 496-502.
45. Tripathi, S.; Sadanand; Lohia, P.; Dwivedi, D. K., Contribution to Sustainable and Environmental Friendly Non-Toxic CZTS Solar Cell with an Innovative Hybrid Buffer Layer, *Solar Energy*, **2020**, *204*, 748-760.
46. Wang, W.; Winkler, M. T.; Gunawan, O.; Gokmen, T.; Todorov, T. K.; Zhu, Y.; Mitzi, D. B., Device Characteristics of CZTSSe Thin-Film Solar Cells with 12.6% Efficiency, *Adv. Energy Mater.*, **2014**, *4*, 1-5.
47. Liu, B.; Guo, J.; Hao, R.; Wang, L.; Gu, K.; Sun, S.; Aierken, A., Effect of Na Doping on the Performance and the Band Alignment of CZTS/CdS Thin Film Solar Cell, *Solar Energy*, **2020**, *201*, 219-226.
48. Chavez, K. L.; Hess, D. W., A Novel Method of Etching Copper Oxide Using Acetic Acid, *J. Electrochem. Soc.*, **2001**, *148*, G640-G643.
49. Zhou, H.; Hsu, W.-C.; Duan, H.-S.; Bob, B.; Yang, W.; Song, T.-B.; Hsu, C.-J.; Yang, Y., CZTS Nanocrystals: A Promising Approach for Next Generation Thin Film Photovoltaics, *Energy Environ. Sci.*, **2013**, *6*, 1-17.
50. Yamada, A.; Matsubara, K.; Sakurai, K.; Ishizuka, S.; Tampo, H.; Fons, P. J.; Iwata, K.; Niki, S., Effect of Band Offset on the Open Circuit Voltage of Heterojunction $\text{CuIn}_{1-x}\text{Ga}_x\text{Se}_2$ Solar Cells, *Appl. Phys. Lett.*, **2004**, *85*, 5607-5609.
51. Yu, S.-H.; Shu, L.; Yang, J.; Han, Z.-H.; Qian, Y.-T.; Zhang, Y.-H., A Solvothermal Decomposition Process for Fabrication and Particle Sizes Control of Bi_2S_3 Nanowires, *J. Mater. Res.*, **1999**, *14*, 4157-4162.
52. Dalapati, G. K.; Zhuk, S.; Masudy-Panah, S.; Kushwaha, A.; Seng, H. L.; Chellappan, V.; Suresh, V.; Su, Z.; Batabyal, S. K.; Tan, C. C.; Guchhait, A.; Wong, L. H.; Wong, T. K. S.; Tripathy, S., Impact of Molybdenum out Diffusion and Interface Quality on the Performance of Sputter Grown CZTS Based Solar Cells, *Sci. Rep.*, **2017**, *7*, 1-12.
53. Ye, H.; Park, H. S.; Akhavan, V. A.; Goodfellow, B. W.; Panthani, M. G.; Korgel, B. A.; Bard, A. J., Photoelectrochemical Characterization of CuInSe_2 and $\text{Cu}(\text{In}_{1-x}\text{Ga}_x)\text{Se}_2$ Thin Films for Solar Cells, *J. Phys. Chem. C*, **2011**, *115*, 234-240.
54. Mkawi, E. M.; Al-Hadeethi, Y.; Shalaan, E.; Bekyarova, E., Fabricating Chalcogenide $\text{Cu}_2\text{ZnSnS}_4$ (CZTS) Nanoparticles Via Solvothermal Synthesis: Effect of the Sulfur Source on the Properties, *Ceram. Int.*, **2020**, *46*, 24916-24922.
55. Zhang, X.; Fu, E.; Wang, Y.; Zhang, C., Fabrication of $\text{Cu}_2\text{ZnSnS}_4$ (CZTS) Nanoparticle Inks for Growth of CZTS Films for Solar Cells, *Nanomaterials*, **2019**, *9*, 1-10.
56. Ananthoju, B.; Mohapatra, J.; Bahadur, D.; Medhekar, N. V.; Aslam, M., Influence of the $\text{Cu}_2\text{ZnSnS}_4$ Nanoparticles Size on Solar Cell Performance, *Sol. Energy Mater. Sol. Cells*, **2019**, *189*, 125-132.

57. Altowairqi, Y.; Alsubaie, A.; Stroh, K. P.; Perez-Marin, I. G.; Bowen, L.; Szablewski, M.; Halliday, D. P., The Effect of Annealing Conditions: Temperature, Time, Ramping Rate and Atmosphere on Nanocrystal $\text{Cu}_2\text{ZnSnS}_4$ (CZTS) Thin Film Solar Cell Properties, *Mater. Today*, **2019**, *18*, 473-486.

Chapter 3

3 Effect of selenium incorporation on the photoelectrochemical behavior of $\text{Cu}_2\text{ZnSn}(\text{S},\text{Se})_4$ films and their solar devices

$\text{Cu}_2\text{ZnSn}(\text{S},\text{Se})_4$ (CZTSSe) was fabricated via sequential electrodeposition of metallic layers followed by selenization. Electrodeposition was found to be a reproducible fabrication technique that allowed for easy control of the composition and morphology of the light-absorbing film. Selenization parameters, such as the temperature and amount of elemental selenium, were varied. Resulting films were etched post-process with acetic acid as well in hopes to remove surface defects. The photocatalytic behaviour of the film variations was tested using photoelectrochemical measurements (PECMs) in order to optimize the light-absorber-layer. XRD and EDX were used to study the structural and compositional differences in films as well as correlate the deviations to the PECM performance. Full devices were manufactured using the most efficient light-absorber-layer. The effect of post-process etching on device efficiencies was discussed and compared to that of the CZTS NCs in Chapter 2.

3.1 Introduction

There exists a global drive to advance research on renewable energy as fossil fuels continue to dominate energy production. Fossil fuels and other non-renewable energy sources cause numerous environmental issues. Among the potential renewable resources, solar energy is deemed one of the most promising and strongest candidates due to its abundance and availability. Thin film solar cells have been employed in latest research as means to effectively and efficiently harvest solar energy. In order to research commercial manufacturing, solar cells must be cost effective and have a photoconversion efficiency of over 18% for small-area devices.^{1,2}

This led to the development and increasing popularity of $\text{CuIn}_x\text{Ga}_{(1-x)}\text{Se}_2$ (CIGS) solar cells on account of its high efficiency. However, gallium being a rare and expensive element, efforts are devoted to generating an alternate, more cost-efficient light-absorbing material. $\text{Cu}_2\text{ZnSnSe}_4$ (CZTSe) has gained attention as a promising material to replace CIGS as it is

comprised of earth abundant, cheap and non-toxic elements.^{3,4} CZTSe and its related alloy $\text{Cu}_2\text{ZnSn}(\text{S},\text{Se})_4$ (CZTSSe) are favourable *p*-type semiconductors with high absorption coefficients and an adjustable band gap energy from 1.0 to 1.5 eV. Highest recorded efficiency for CZTSe and CZTSSe is 11.8% and 12.6% respectively.^{5,6} Due to the lower-than-desired device efficiency, this material is not yet available for commercial use. Many factors contribute to poor device efficiency, the most poignant being open circuit potential (V_{OC}) deficit.^{1,7,8}

The underperformance and deficit can factor from defect phases in the film and the deposition technique.⁹ An innate trait of high-efficiency CZTSe solar cells is its non-stoichiometric, generally Cu-poor and Zn-rich, composition.¹⁰ Yet this alludes to the issue of the narrow stable region of pure phase CZTSe and easy formation of defects.^{9,11} Many secondary phases such as CuSe, Cu_2Se and ZnSe are anticipated to form due to the intolerance in composition variance.^{10,12} Better understanding of the secondary phases and methods to remove them need to be developed in order to decrease the V_{OC} deficit. Surface impurity removal methods have been explored and are generally achieved by post-process KCN etching.¹² This chemical etchant however is highly toxic and does not align with environmentally friendly goals.

Typical deposition methods of CZTSe and CZTSSe include sol-gel, spray pyrolysis and vacuum-based techniques. The maximum efficiency of 12.6% for CZTSe was achieved by films fabricated with hydrazine-based solutions.^{6,13} It is not currently in extensive use due to the toxic nature of hydrazine and other solution-based techniques.¹⁴ Electrochemical deposition is an advantageous method to prepare films due to low-cost, high deposition per area and easy control of film composition.² The quality of the light-absorber-layer is a key aspect to high efficiency as a high concentration of lattice defects or impurities lead to reduced performance. In order to obtain a phase-controlled film, increased grain size is desired.¹⁵ This promotes investigations into annealing temperature as it has an important role in the formation of large grain size in single phase CZTSe. The effects of annealing in a selenium-rich atmosphere, or selenization, have not been methodically studied and could result in increasing grain size and in turn reduce recombination in the film.

Herein, the CZTSSe films were fabricated by serial electrochemical deposition of metallic layers followed by an annealing and selenization process. The work in this chapter focuses on selenization parameters and post-process etching and their effects on the morphological, compositional and optical properties of the light-absorber-layer. Optimization of selenization parameters will occur by photoelectrochemical measurements (PECMs) of the catalytic conversion of MV^{2+} to MV^+ in solution. PECMs are an invaluable technique to measure performance of the light-absorbing-layer before full device manufacturing, thereby saving costs. Results were obtained for CZTSe with residual sulfur from the furnace tube during the annealing process, producing CZTSSe.

Compositional analysis was conducted to validate the formation of CZTSSe and study the effect of $S/(S+Se)$ ratio on performance. It has been shown that kesterite solar cells with high efficiencies were achieved with lower $S/(S+Se)$ ratios.^{5, 7} Glacial acetic acid was selected as the chemical etchant to remove surface impurities. The effectiveness of post-process etching was explored and compared to the success of its use on CZTS nanocrystals. Full devices, with CZTSSe as the light-absorbing-layer, were manufactured and analyzed to determine best photoconversion efficiency for non-etched and etched devices. Unless specified, procedures were conducted in an open-air environment to keep fabrication low-cost.

3.2 Experimental

3.2.1 Fabrication from absorber layer to full device

CZTSe films were fabricated using galvanostatic electrodeposition of metallic precursors with a Solartron 1287 Potentiostat, followed by high temperature selenization. Soda-lime glass (SLG) with a thickness of 500 μm , with 0.5 μm of Molybdenum sputtered on top, was purchased from University Wafer (Boston, MA). A three-electrode system was employed to deposit the precursors with the Mo-coated glass as the working electrode and a platinum mesh as the counter electrode. The reference for the copper precursor was a SCE while the reference for both tin and zinc precursors was an Ag/AgCl electrode. Copper was first deposited using a constant current density of 2.5 mA/cm^2 on the working electrode immersed in a solution containing 25 g/L $\text{CuSO}_4 \cdot 5\text{H}_2\text{O}$ (Sigma-Aldrich, 99.995%), 120

g/L NaOH (Sigma-Aldrich, 97% pellets), and 37.5 g/L D-sorbitol (Sigma-Aldrich, $\geq 98\%$). A tin sulfate plating bath was purchased from Technic Incorporation (Cranston, RI) and deposited on top of the copper layer using a constant current density of 6.0 mA/cm^2 . Finally, a constant current density of 3.0 mA/cm^2 was applied to deposit the zinc on top of the copper and tin layers. The zinc bath was comprised of 8 g/L ZnCl_2 (Sigma-Aldrich, 99.999%), 150 g/L KCl (Sigma-Aldrich, $\geq 99.0\%$), and 12.9 g/L poly[bis(2-chloroethyl)ether-alt-1,3-bis[3-(dimethylamino)propyl]urea] (Sigma-Aldrich, 62% wt% in H_2O).

The stacked film samples were then placed in a Thermo Scientific Lindberg Blue M Tube Furnace with a quartz tube for vacuum and argon purges. For the selenization of the films, the temperature and ratio of selenium to surface area were varied to determine the best combination of parameters. The annealing temperature was held at $275 \text{ }^\circ\text{C}$ for 20 minutes while selenization temperatures varied from $400 \text{ }^\circ\text{C}$ to $500 \text{ }^\circ\text{C}$ in $50 \text{ }^\circ\text{C}$ increments with a final temperature of $525 \text{ }^\circ\text{C}$. The tube was purged three times via vacuum pump to -100 kPa then filled with argon gas to a pressure of 40 kPa . The furnace was shut off and purged to remove any excess selenium vapour from the system. The starting mass-to-area ratio of 10 mg/cm^2 was used for selenium powder to first optimize the selenizing temperature. This procedure was then repeated for starting ratios of 3 and 5 mg/cm^2 in addition to the 10 mg/cm^2 of selenium powder to determine which amount enhanced the photoresponse the most. Additionally, the fabricated films were etched with acetic acid for 30 minutes and tested in tandem to varying the selenium amount. This was done to determine if etching reaped similar benefits to the photoresponse as in *Section 2.3.1*.

A buffer layer of cadmium sulfide (CdS) was deposited onto the CZTSe films via chemical bath deposition (CBD). The bath was prepared by stirring a mixture of 103.5 mg of cadmium acetate (Sigma-Aldrich, 99.99%), 4.5 mL ammonium hydroxide (Caledon, $>99\%$) and 3 mL of 1 M ammonia acetate in a volume of 142.5 mL of MilliQ water at a temperature of $65 \text{ }^\circ\text{C}$ for 30 minutes. 1.5 mL of 0.5 M thiourea was added and heated for an additional 30 minutes, followed by the submersion of samples for 7.5 minutes yielding a 50 nm layer of CdS.

Resultant CZTSe/CdS films were then placed in the Ultratech/Cambridge NanoTech Savannah S200 Atomic Layer Deposition (ALD) workstation reaction chamber for 10 minutes at 200 °C under vacuum to remove water intercalation. The deposition of both 50 nm ZnO and 250 nm AZO follows the procedure detailed elsewhere.¹⁶

3.2.2 Characterization

Photoelectrochemical measurements (PECMs) were obtained with a CH Instruments electrochemical analyzer model CHI 832B. This method was carried out before and after the deposition of CdS as it is used to determine the photovoltaic quality of the light-absorbing-layer. The measurements were done via a 3-electrode system in an aqueous solution of 0.05 M MV^{2+} and 0.1 M KCl with the working, reference and counter electrodes being the film, a SCE and platinum coil respectively. The light source was a 150 W Newport lamp with an AM 1.5 D filter. A ThorLabs SC10 shutter was used to produce the square-wave light stimulus system in 3 second intervals. A linear potential sweep was applied from 0.0 to - 0.4V at a scan rate of 5 mV/s using the CHI 832B electrochemical analyzer.

Fabricated films were removed from the Mo-coated substrate through physical abrasion and were then dispersed in isopropanol to 0.5 g/L for band gap measurements. Absorption measurements were obtained using a Cary 50 UV-VIS instrument. The energy band gap was determined through a Tauc plot conversion of the resultant absorption spectra.

The electrochemical characteristics of the film were then correlated to its elemental composition and crystal structures using Scanning Electron Microscopy (SEM) and Powder X-ray Diffraction (P-XRD) respectively. SEM was performed on etched (E) and non-etched (NE) CZTSe films using a Hitachi TM3030 Plus Tabletop microscope with an EDX system at 15.0 kV. P-XRD patterns were collected using an Inel CPS Powder Diffractometer with an Inel XRG 3000 Cu X-ray generator an Inel CPS 120 detector. Resulting patterns were compared to standard diffractograms using the ICDD Database and PDF4+ software (ICDD, PA). Crystal structures were simulated with VESTA ver. 3.5.5.¹⁷

Final device power conversion efficiencies were measured via J-V curves. These were produced by the IVIUM CompactStat coupled with a 150 W Newport lamp with an AM 1.5 D filter. A power meter measured the illumination power to be 0.69 “suns”.

3.3 Results and Discussion

3.3.1 Development of selenization criterion

The optimal temperature along with the mass-to-area ratio of selenium for selenization were determined via PECMs. The behaviour of the film under chopped illumination provided information of the MV^{2+}/MV^+ reaction kinetics with respect to the photoresponse of each film. The PECMs for CZTSe films made with selenization temperatures of 400 °C, 450 °C, 500 °C and 525 °C are shown below in Figure 3.1. Each of these films were produced with a starting mass to area ratio of 10 mg/cm² of selenium and the range of photocurrent obtained for the variety of temperatures are summarized in Table 3.1. Films were also produced at temperatures lower than 400 °C but no PECMs were obtained as the temperature was not hot enough to deposit the selenium onto the substrate, and instead remained beaded on the graphite boat in the furnace.

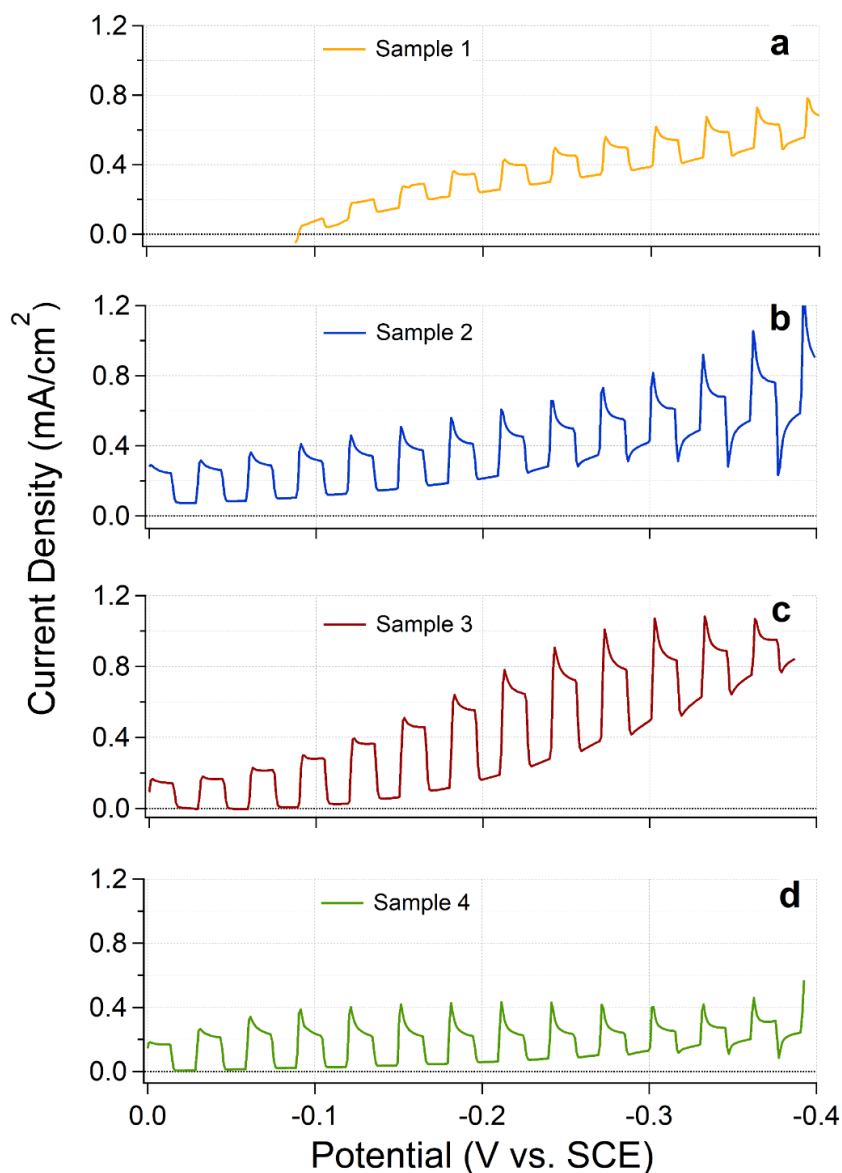


Figure 3.1: Photoelectrochemical measurements of CZTSe films fabricated with 10 mg/cm² of selenium at selenization temperatures of a) 400 °C, b) 450 °C, c) 500 °C and d) 525 °C.

In each case, the current density increases rapidly when the light is initially turned on and dropped to a near zero value when the light is turned off. The difference in current densities between light-on and light-off scenarios is referred to as the maximum current density or photocurrent achieved. This change in current density upon illumination establishes the electron transfer to reduce MV^{2+} to MV^{+} in solution as stated in *equation 1.7*. These

measurements can also give insight into the relative rates of the reactions occurring in solution upon illumination, described by *equations 1.3 - 1.7* in *Section 1.4.6*.¹⁶

When the bias is close to zero, a square wave is observed in almost every trace at the beginning of the scan, however at more negative biases, there is an exponential decay before a plateau in either the light-off or light-on scenarios. This indicates that the rate of recombination dominates over the product separation at light-on scenarios and vice versa for light-off scenarios. In each case, there is also a gradual increase of dark current with more negative bias, indicated by the increase in scan slope at more negative potentials. This illustrates a shift from the p-type rectifying Schottky junction to a non-rectifying Ohmic junction and will ultimately result in lower open circuit potentials for full devices.^{18,}
19

Table 3.1: Range of photocurrent achieved in a PECM as a function of selenization temperature.

	Selenization temperature	Photocurrent range
a): Sample 1	400 °C for 30 min.	0 - 0.20 mA/cm ²
b): Sample 2	450 °C for 30 min.	0.25 - 0.53 mA/cm ²
c): Sample 3	500 °C for 30 min.	0.20 - 0.65 mA/cm ²
d): Sample 4	525 °C for 30 min.	0.20 - 0.40 mA/cm ²

Figure 3.1a displays the PECM for the CZTSe film selenized at 400 °C which resulted in having the poorest and most unstable photoresponse out of the four samples. As current densities start below zero, the film shows no stability in the Schottky barrier due to the continual increase in dark current. In addition, this sample showcases very little increase upon illumination as the maximum photocurrent achieved by the PECM was only 0.20 mA/cm². The film did however prove to have the lowest amount of recombination as the

rate of product separation dominated at almost all potentials and the scan was almost continually a square-wave. For the instance of a film selenized at 450 °C, an increase in photocurrent achieved was observed in Figure 3.1b and reached a final maximum current density of 0.53 mA/cm².

CZTSe is a *p*-type semiconductor and so a negative bias must be applied to allow electron transfer from the film to the MV²⁺ in solution upon photoexcitation.^{20, 21} Now as the bias become more negative, more electrons will transfer with ease to restore the charge balance in solution displaying an increase in photocurrent at these negative biases. This occurrence continues until the film itself is saturated with electrons so that a more negative bias does not result in an increase in photocurrent.²² In the case of Figure 3.1b, the semiconductor film has not been saturated with electrons yet as it is seen to continually increase in photocurrent until the end of the scan. Moving towards negative potentials of the scan, there is also a rapid increase of recombination at the light-on scenarios and enhanced product separation at the light-off scenarios due to excess charges on the surface of the film, described by *equation 1.6* and *1.7* in *Section 1.4.6*.

Figure 3.1c presents the PECM for the CZTSe film selenized at 500 °C and demonstrates similarities to Figure 3.1b in photoresponse and shape of the curve but achieves a higher maximum photocurrent of 0.65 mA/cm². This PECM for Sample 3 shifts faster to an Ohmic junction as the dark current is observed to rapidly increase from -0.20 V onwards. Nevertheless, there is reduced recombination in the light-on scenarios with increasingly negative biases and little to no continuous product separation at light-off scenarios; thus, indicative of a higher quality film. Another major difference between Sample 2 and 3 is that the former becomes saturated with electrons earlier on at -0.30 V as the photoresponse slightly decreases towards the end of the scan. This showcases that progressively negative biases do not continue to increase the photocurrent.

Sample 4 is the CZTSe film selenized at 525 °C which does not follow the trend of a 50 °C increase in temperature. This was done as a temperature of 525 °C proved to be beneficial with electrodeposited CZTS films.²³ Temperatures above this showed a reduction in photoresponse and increase in elemental tin loss.²⁴ Figure 3.1d displays the

PECM for Sample 4 and showcases the lowest amount of dark current of the four samples as there is no sharp increase in scan slope. Therefore, suggesting that the formed Schottky junction, is maintained longer before shifting towards an Ohmic junction. Nonetheless, Sample 4 recorded a lower photocurrent achieved than both Sample 2 and 3. It displays a similar amount of recombination as in Figure 3.1b, signifying that the rate of recombination dominates over the rate of product separation at progressively negative potentials. Based on the results from Figure 3.1 and Table 3.1, further fabrication will utilize a selenization temperature of 500 °C for 30 minutes.

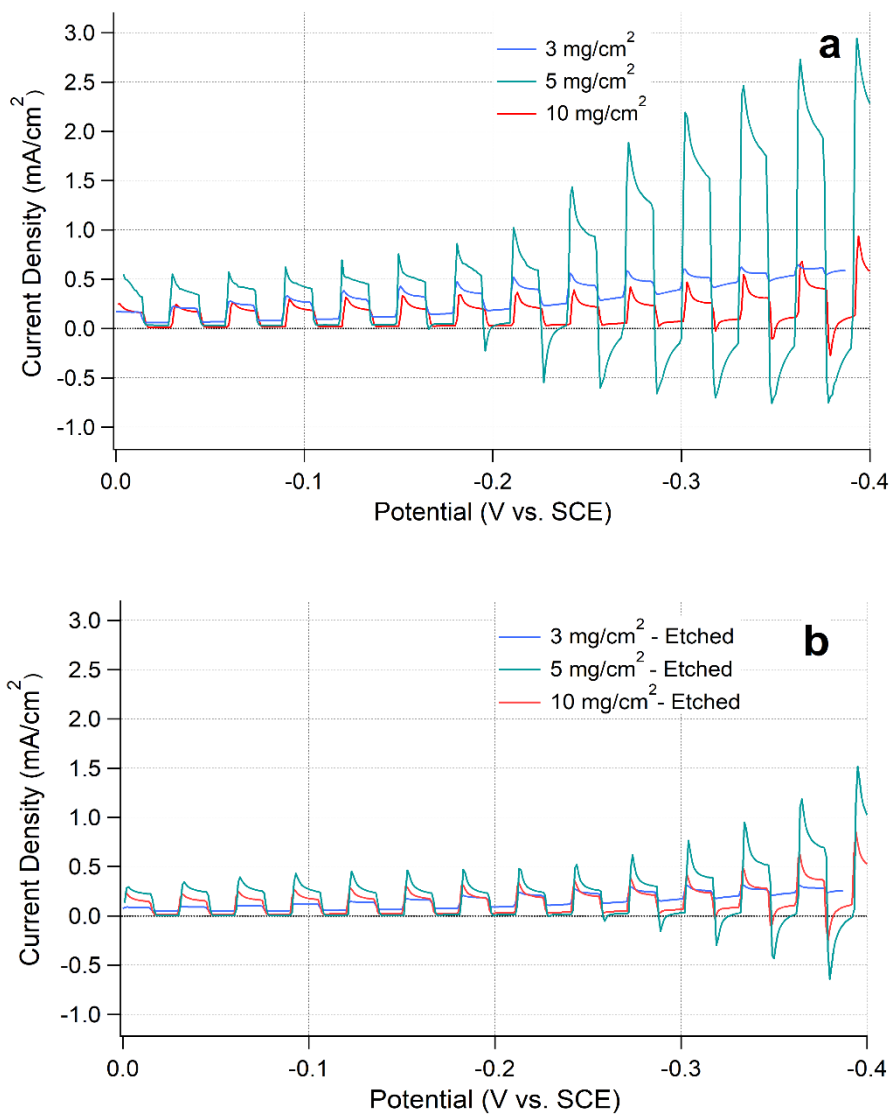


Figure 3.2: PECMs showcasing films with various selenium concentrations, all selenized at 500 °C. a) NE scenario with 3, 5, & 10 mg/cm² selenium and b) E scenario with 3, 5 & 10 mg/cm² of selenium.

Additionally, the selenium concentration in the CZTSe layer was optimized by testing three different amounts of selenium mass to area ratios: 3, 5 and 10 mg/cm². These values were chosen based on previous treatments for CZTS where 10 mg/cm² of sulfur produced the highest photoresponse.¹⁶ An increase in selenium could produce enhanced secondary phases or defects as it is already in excess at a ratio of 10 mg/cm². Hence from the 10 mg/cm² ratio, shown in Figure 3.2, the selenium was reduced to 5 mg/cm² and once more

to 3 mg/cm^2 to determine the effect on the photoelectrochemical behaviour. Furthermore, the etching process described in *Section 2.2.1*, was investigated at this stage of fabrication to determine its success of enhancing photoresponse as it proved beneficial for the CZTS NCs.

Figure 3.2 features PECMs of all three selenium concentrations with Figure 3.2a exhibiting a NE scenario and Figure 3.2b exhibiting an E scenario. The range of photocurrent achieved for the three concentrations in both NE and E situations are summarized in Table 3.2. The traces for both scenarios bring understanding to the rates of reaction in solution; these are similar to that of the PECMs at different temperatures in Figure 3.1 and have been discussed extensively in *Section 2.3.1*. In both Figure 3.2a and b, the traces for 5 and 10 mg/cm^2 of selenium increase in photocurrent. With increasingly negative bias, the films have not yet been saturated with electrons unlike the trace for 3 mg/cm^2 which decreases in photocurrent from -0.20 V onwards. Moreover, only the trace for 3 mg/cm^2 of selenium in both NE and E situations shift towards an Ohmic junction at progressively negative potentials. This may be on account of poor selenium incorporation to create binary selenide phases that react to form CZTSe.^{4, 14} Thus, resulting in inadequate conductivity and a poor performing film as only a maximum current density of 0.35 mA/cm^2 and 0.15 mA/cm^2 was reached in the NE and E scenarios respectively.

Table 3.2: Summary of maximum photocurrent achieved for each selenium concentration for both NE and E films.

	Non-Etched	Etched
3 mg/cm^2	0.35 mA/cm^2	0.15 mA/cm^2
5 mg/cm^2	2.80 mA/cm^2	1.50 mA/cm^2
10 mg/cm^2	0.75 mA/cm^2	0.55 mA/cm^2

For the NE film with 5 mg/cm² of selenium, the rate of recombination dominates over the rate of product separation at the light-on event while the opposite is true for the light-off event from -0.20 V onwards. For the E film with 5 mg/cm² of selenium, the rate of product separation dominates over recombination later from only -0.30 V onwards. The films that used 5 mg/cm² of selenium consistently demonstrated higher photocurrent than the other two concentrations as it reached maximums of 2.80 mA/cm² and 1.50 mA/cm² in the NE and E conditions respectively. Nevertheless, the photocurrent is more pronounced in the NE case and decreases significantly after etching with acetic acid. This is in contrast to what has been proved for sulfide-based films such as the CZTS NCs in Chapter 2. The reduction in photoresponse after etching could be by cause of selenium residing on the surface rather than adhering to the back contact, therefore negatively affecting the photoresponse once etched off.

A similar trend in the shape of the transients at light-on and light-off events is seen at a lesser extent for the E and NE films made with 10 mg/cm² of selenium. When 10 mg/cm² is used, the maximum photocurrent is reduced to 0.75 mA/cm² and 0.55 mA/cm² in the NE and E cases respectively. This decrease in photoresponse may be from an excess of selenium which can cause incomplete reaction of the selenide phases that form CZTSe or cause poor adhesion to the back contact, both of which lessen the current throughout the film.²⁵ From the results of Figure 3.2 and Table 3.2, full device fabrication will utilize NE films made with 5 mg/cm² of selenium at a temperature of 500 °C.

3.3.2 Structural analysis via x-ray diffraction

Forming a pure phase of CZTSe with the optimal composition can be difficult as the material has a very narrow range for stability under thermodynamic growth conditions.^{26,}
¹⁵ In addition, secondary phases and defects are prone to easy formation during high temperature fabrication. Figure 3.3 shows the XRD patterns of CZTSe films selenized at various temperatures. These diffractograms were analyzed to study how crystal size and defect growth varied in order to decide the best temperature to further fabricate with. These films were fabricated with 10 mg/cm² of selenium and therefore, the diffractograms will reveal the amount of selenium incorporation at each temperature along with the phases it is being incorporated into. Each sample exhibited presence of Mo (JCPDS# 00-004-0809)

and diffraction peaks of a chalcopyrite structure with favored orientation to the (112) direction. However, they also all exhibited secondary phases due to possible contamination during the selenization process. The furnace at this fabrication step had introduced sulfur into the system thus causing additional secondary phases or shifts in peaks. Since there is a lack of dual peaks corresponding to both selenium and sulfur, it is proposed that sulfur is substituted into sites where selenium is expected.^{27, 28} Secondary phases such as Cu_2Se (JCPDS# 00-004-0839), MoSe_2 (JCPDS# 00-029-0914) and MoS_2 (JCPDS # 00-037-1492) can be seen in Samples 1-4 with varying intensities dependent on temperature.

As the temperature increases, the (111) reflection for Cu_2Se located at 26.4° becomes prominent and increases in intensity from Sample 3 onwards. This is also true for the Cu_2Se (311) reflection peak located at 51.1° , suggesting that selenium is residing on the surface of the film to bind with the copper. The MoSe_2 (100) reflection peak located at 31.8° in Samples 1 and 2 are quite intense but reduce in intensity with increasing temperature. However, that is when the (200) and (108) reflection peaks for MoSe_2 present themselves at $65.0 - 66.0^\circ$ in Samples 3 and 4. This increase proposes that there is a strong selenium bond with the back contact in all four samples, although more prominent in the first two. It is presumed that sulfur has been introduced into all four samples and what phases it creates becomes clear as the temperature increases.

A predominant feature in the diffractograms of Sample 3 and 4 is the MoS_2 (101) reflection peak located at 33.8° . These molybdenum secondary phases then indicate that there is a stronger back contact bond with selenium at lower temperatures and with sulfur at higher temperatures. These secondary phases with the back contact in either case are not ideal as they can provide recombination sites and reduce performance.²⁹ No binary phases such as CuSe and SnSe are seen, suggesting that the precursor reaction went to completion to form the CZTSe layer.¹⁰ Other secondary phases such as ZnSe and Cu_2SnSe_3 are not able to be distinguished from the diffractograms as the Bragg's peak of those overlap with that of stoichiometric CZTSe.

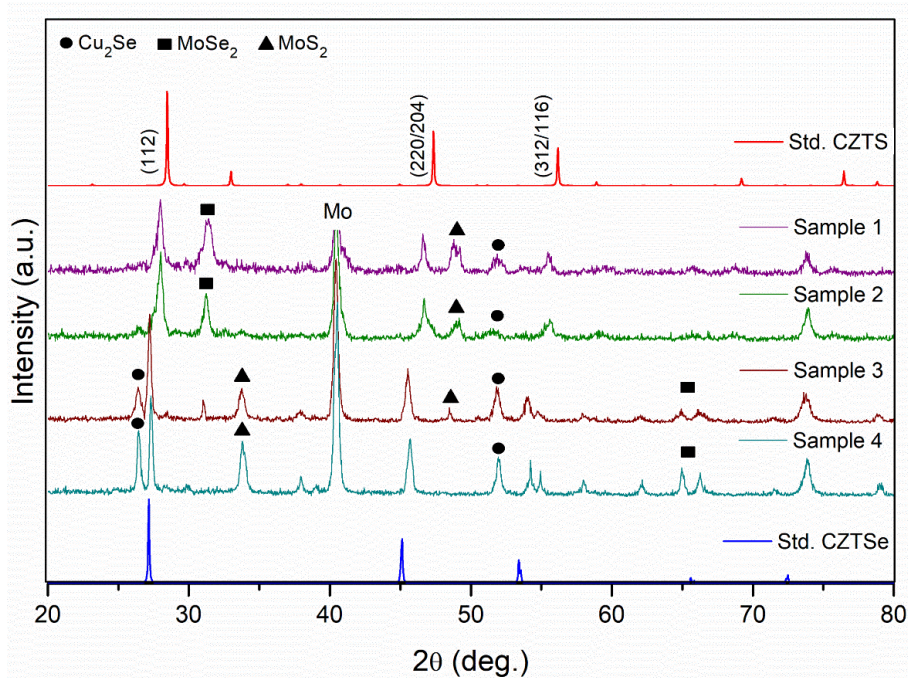


Figure 3.3: XRD diffractograms for Samples 1-4 of CZTSSe. Resulting secondary phases and defects are summarized in the legend within the figure.

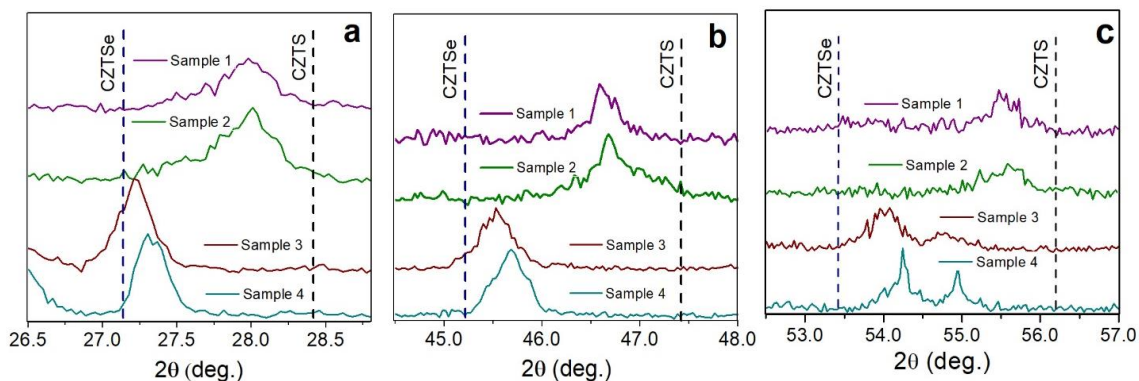


Figure 3.4: XRD diffractograms for Samples 1-4 centered at a) (112) reflection kesterite peak ranging from 26.5° – 28.8° , b) (220/204) reflection kesterite peak ranging from 44.5° – 48.0° and c) (312/116) reflection kesterite peak ranging from 53.5° – 57.0° . The dashed lines in each figure represent the standard CZTSe and CZTS peaks.

Therefore, to confirm the presence of CZTSe (JCPDS # 00-052-0868) and CZTS (JCPDS # 00-026-0575) phases, the three major crystallographic reflection peaks at (112), (220/204) and (312/116) were studied. Considering these reflections are located at 27 – 28.5°, 44 – 47.5° and 52 – 57° respectively, Samples 1 – 4 show several intermediate peaks between the standard CZTSe and CZTS phases indicating the presence of kesterite $\text{Cu}_2\text{ZnSn}(\text{S},\text{Se})_4$ (CZTSSe) in the samples.^{25, 30, 31} The intermediate peaks are most prominent for the reflection at (112) but are also present for the reflections at (220/204) and (312/116).

Figure 3.4 showcases a zoom of the full diffractogram centered around a) the (112) reflection peak, b) the (220/204) reflection peak and c) the (312/116) reflection peak. In all the inlays, the intermediate peaks tend to be between the known CZTSe and CZTS peaks yet shift towards the CZTSe peak at higher temperatures. Assuming that this shift is linear from CZTS towards CZTSe as S replaces Se, the intermediate peak position can be used to determine the S/(S+Se) content.^{30, 31} The linear interpolation was done using the (112) peak in Figure 3.4a as it has the highest intensity, thus, being easy to calculate. The content can then be estimated using the following formula, where x is the intermediate peak position and A is the linear factor. The linear factor equates to 1.28 as it is the difference between the standard (112) peaks of CZTSe (27.16°) and CZTS (28.44°).

$$\frac{[S]}{([\text{Se}]+[S])} = \frac{x-27.16}{A} \quad (3.1)$$

The resulting S/(Se+S) contents are summarized as percentages in Table 3.3 with the smallest percentage signifying the highest amount of selenium in the CZTSSe phase. Studies where CZTS was sputtered then selenized at various temperatures demonstrated that this ratio tends to decrease with increasing temperatures and that higher S/(S+Se) ratios lead to easier formation of defects.^{32, 33} At lower temperatures for Samples 1 and 2, the selenium incorporation into the CZTSSe phase is low as the S/(Se+S) ratio is 62.0% and

57.0% respectively. For that reason, the selenium that is present in the film binds with the back contact to create more of the MoSe₂ impurity and the intermediate peak is situated closer to the CZTS standard peak.

As the temperature increases for Sample 3, the selenium incorporation into the kesterite CZTSSe phase is high as the S/(Se+S) content is reduced significantly to 4.70%. Excess sulfur that may remain in the system then binds with the back contact to create added MoS₂ impurities. Despite the added low-intensity secondary phases in Sample 3, the main kesterite reflection peak at (112) shifts towards the standard CZTSe phase, thus, forecasting a better performance than Sample 2. At a temperature of 525 °C for Sample 4, the intermediate peak starts to shift away from the standard CZTSe peak and acquires a S/(Se+S) percentage of 13.0%. Although higher temperatures imply a higher amount of selenium in the kesterite phase, the amount of impurities in the diffractogram of Sample 4 indicate that there is excess selenium binding with the surface impurities.

The intermediate peaks for reflections at (220/204) and (312/116) follow the same trend between the standard peaks as they shift towards the CZTSe phase at higher temperatures, with the exception of Sample 4. Another reason for the shift may occur due to the x-ray incident angle. As the incident angle becomes larger, more of the bulk film will be measured and the closer the measurements will be to the CZTSSe/Mo interface.⁵ A narrower incident x-ray angle will strike towards the surface of the film and away from the film/substrate interface. It can then be presumed that all four samples had a larger x-ray incident angle as the powder patterns all have a strong Mo (110) peak at 40.5°, with Sample 4 having the largest incident angle since the intensity of the Mo peak in Sample 4 is the strongest.

The intermediate peaks can also be used to calculate the average grain size among these samples by using Debye Scherrer's formula expressed in *equation 3.2* where D is the crystallite or grain size, λ is the wavelength of the x-ray source (CuK α $\lambda = 1.5046$ Å), β is the FWHM of the (112) peak determined by gaussian fitting and θ is the Bragg angle of the intermediate (112) peak.^{4, 34} The grain size along with other XRD parameters determined through the (112) reflection peak are summarized in Table 3.3.

$$D = \frac{0.9\lambda}{\beta \cos\theta} \quad (3.2)$$

Table 3.3: XRD parameters evaluated for electrodeposited CZTSe Samples 1-4 through the (112) reflection for different selenization temperatures where standard CZTSe (112) peak is 27.16°.

	Selenization temperature	Bragg angle (2θ)	FWHM (rad)	Grain size (nm)	Lattice strain (ϵ) $\times 10^{-3}$	Dislocation density (δ) (nm^{-2}) $\times 10^{-3}$	$\frac{[S]}{([Se] + [S])}$ (%)
Sample 1	400 °C	27.95°	0.010	14.0	2.5	5.2	62.0
Sample 2	450 °C	27.95°	0.011	13.0	2.5	5.4	57.0
Sample 3	500 °C	27.22°	0.0047	30.0	1.1	1.1	4.70
Sample 4	525 °C	27.33°	0.0050	28.0	1.2	1.2	13.0

It is observed that the average crystallite size increases with the selenization temperature until 525 °C where the size decreases slightly but is still comparable. As the temperature increases, there is more available energy for atoms to acquire so that crystallites collide to form bigger particles. The trend of increase in grain size does not follow for Sample 4 at 525 °C as the grain size slightly decreases. This can once again be attributed to a possible change in the x-ray incident angle and demonstrating that for Sample 4, the grain size is possibly larger on the surface of the film rather than the bulk material where the other samples seem to be primarily measured.^{5, 35} Now as temperature increases, the FWHM of the intermediate peaks should decrease, giving way to a more crystalline film, ensuring that holes and gaps in the film do not disrupt current along the surface of the film.

This is a point of significance seeing as Sample 3 had the largest measured photocurrent, grain size and the smallest FWHM. Holes and gaps in the material can cause geometric dissimilarity at the boundaries between crystal lattices of the film and the substrate which can affect the structural properties of the film and cause lattice strain.³⁶ Once lattice stress transpires, lattice deformities or dislocations may occur. The dislocation density is then a measure of the number of dislocations in a unit volume of a crystalline material. The lattice strain and dislocation density can be calculated using *equations 3.3 and 3.4* respectively.^{4,34}

$$\varepsilon = \frac{\beta \cos \theta}{4} \quad (3.3)$$

$$\delta = \frac{1}{D^2} \quad (3.4)$$

The ε , β , θ , δ and D variables represent the lattice strain, FWHM through (112), Bragg angle, dislocation density and the grain size accordingly. Principally, the dislocation density will increase as the grain size decreases due to the increased number of potential gaps in the surface of the film. Out of all four samples, Sample 3 has the largest particle size and consequently has the smallest dislocation density and lattice strain, proving the selenization temperature of 500 °C ideal to fabricate the CZTSSe absorber layer for predictably higher photoresponse.

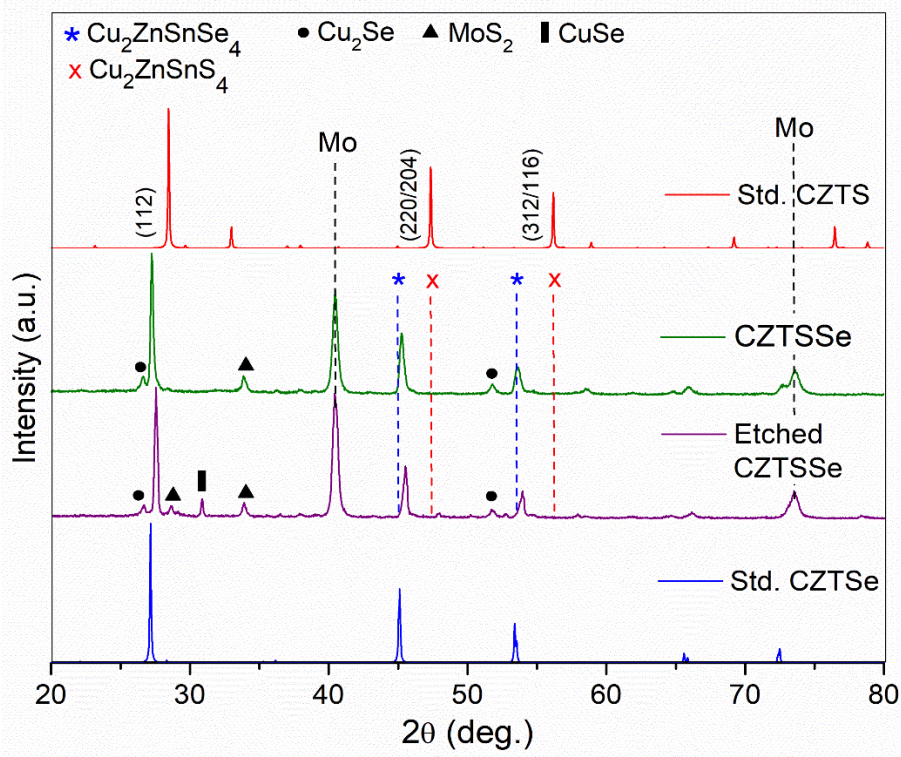


Figure 3.5: XRD diffractograms for CZTSSe in both NE and E scenarios. The blue and red dashed lines represent the standard CZTSe and CZTS peaks respectively. The secondary phases present are labeled in the legend while the three major crystallographic peaks are labeled on the standard CZTS spectrum.

Figure 3.5 shows XRD patterns for CZTSSe films produced at 500 °C in both E and NE scenarios. Analyzing the diffractograms may give some insight into the large difference in photocurrent produced by the films as per Table 3.2. Both experimental traces show the three main crystallographic peaks as expected and match well to the standard CZTSe phases. However, a small shift in peaks is mainly observed with the (112) peak but also for the (220/204) and (312/116) peaks. The three main peaks are shifted toward higher 2θ angles as the (112) peak shifted from 27.31° in the NE to 27.44° in the E film. After etching, an increase in MoS_2 and CuSe peaks are observed in the diffractogram, which opposes the belief that the etchant would remove these phases from the surface of the film.¹⁶ If the secondary phases segregated near the surface, it would have been etched by the acid easily as shown in *Section 2.3.1*. Since this was not the case, the defects must exist buried in the bulk material toward the back-contact of the film in these Cu poor conditions.

Another reason for the disparity in photoresponse along with the shift in peaks is as the etchant is removing selenium from the surface, sulfur is substituted in lieu of selenium in the crystal lattice.^{25, 31} By doing this, any Cu_xSe phases under the surface may be exposed and are likely to act as recombination centers for the photocurrent. The presence of MoS_2 growth in the E film indicates that the etching process revealed sulfur that has penetrated deeper into the film and bound with baring Mo substrate. The presence of the Mo-bound impurities and the small shift is not likely to account for a large disparity in performance between the films and so further characterization is required.

$$\frac{1}{D^2} = \frac{h^2+k^2}{a^2} + \frac{l^2}{c^2} \quad (3.5)$$

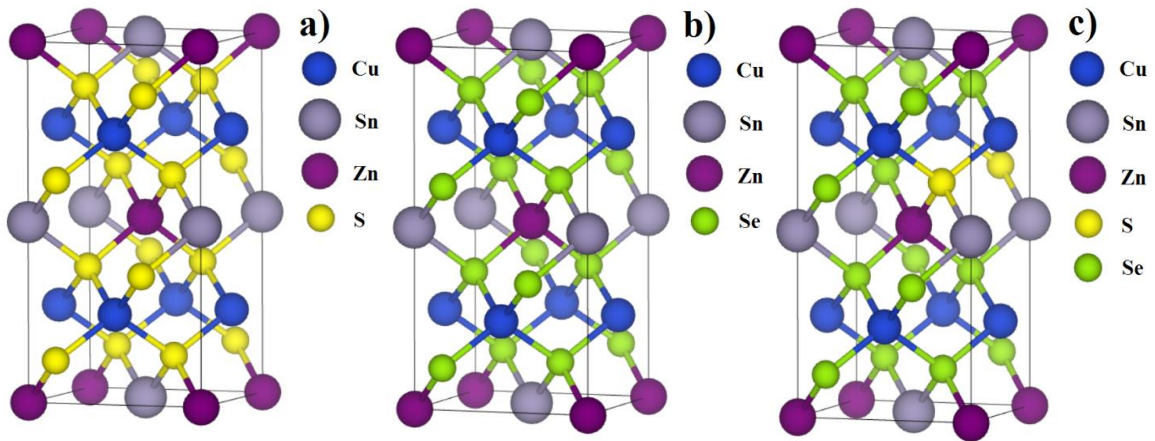


Figure 3.6: Crystal structures for: a) standard CZTS, b) standard CZTSe and c) an estimate of CZTSSe with 12.5% sulfur incorporation.

In a unit cell, the lattice constant is the length between two points on the corner of the cell and are designated by the letters a , b , and c . In a tetragonal structure, two sides are of the same length and so lattice constant a is equal to b .³⁷ The remaining lattice constants a and c can then be calculated by using *equation 3.5* where D is the d-spacing between two planes and h , k , and l are the miller indices of the peak position.^{34, 37} The lattice constants for both E and NE CZTSSe were evaluated using the (112) and (220/204) peaks. The resultant constant values along with the standards for CZTS and CZTSe are summarized in Table 3.4.

Standard crystal structures of CZTS and CZTSe along with an estimation of CZTSSe with a 12.5% sulfur incorporation is shown in Figure 3.6. The lattice constant a for both NE and E CZTSSe agree well to the standard CZTSe and work published by *Zoppi et al.*³⁸ The lattice constant c for the NE film agrees well to the standard however the c parameter for the E film is an intermediate value between standard CZTSe and CZTS.³⁹ This can be explained by the substitution of sulfur atoms in lieu of where selenium is expected to be. This substitution can greatly distort the chalcopyrite lattice as shown by constant c and can even alter the electronic properties of the material as exhibited by the photoresponse in Figure 3.2.¹ Since sulfur is a smaller atom than selenium, the crystal lattice is expected to distort further as more sulfur is incorporated into the film or as more selenium is etched off the film. In addition, the existence of Cu_xSe impurities can strain the lattice further and alter its lattice parameters.⁴⁰ Further compositional analysis is still required to explain the photoresponse reduction after the etching process.

Table 3.4: Experimental lattice constants compared to standards

	Lattice constants a & b	Lattice constant c
Std. CZTS	5.43 Å	10.84 Å
Std. CZTSe	5.68 Å	11.35 Å
CZTSSe	5.66 Å	11.31 Å
Etched CZTSSe	5.63 Å	11.13 Å

3.3.3 Composition and morphology

Surface morphology of CZTSSe in both NE and E scenarios were studied via SEM images shown in Figure 3.7. Low magnification of the images with the scale of 50 μm exhibits an overview while the high magnification inset with the scale of 10 μm exhibits a detailed view of the morphology. From the overview, the NE film is observed to have little surface details and more of a uniform surface; however, a change in film surface is noticed after

the etching process. After etching, the porosity and severity of cracks increased in the film both of which may lead to leakage current and degrade the performance of the full device.⁷

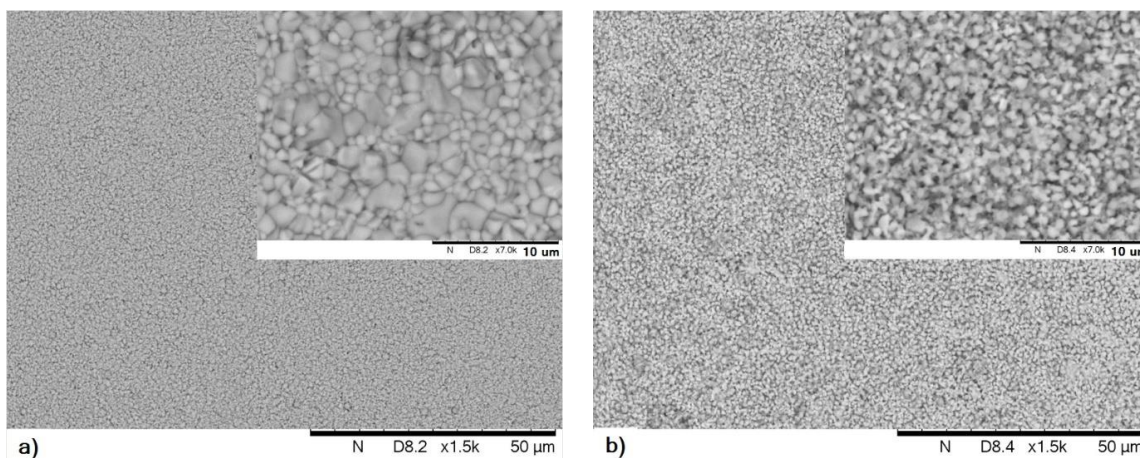


Figure 3.7: Surface morphology of a) a NE and b) an E CZTSSe film. In each figure, the larger image has a scale of 50 μm while the inset has a scale of 10 μm .

Upon higher magnification, the films demonstrate a great difference between morphology. In the inset of Figure 3.7a, it is observed that the film is tightly packed and comprised of grains that vary in size. In contrast, the E film in the inset of Figure 3.7b displays just the opposite as grain structures are more uniform in size and shape but appears to be loosely packed. This decrease in grain density after etching can account for the diminished photocurrent that is observed in Figure 3.2b for the E films. Loss of crystallinity hinders efficient electron flow across the surface of the film as charge must rely on granular edge contacts.²⁶ A decrease in performance may also result from grain boundaries rather than the formation of secondary phases as these boundaries tend to owe to defect clusters.^{41, 42} There were no alterations made to the fabrication process and so the disparity in surface roughness and density can be attributed to the etching process or at least the etchant itself. Identifying another etchant to improving surface treatments is however beyond the scope of this work and devices with the NE CZTSSe layer are expected to perform better.

Table 3.5: Elemental ratios determined through EDX for both NE and E circumstances.

	Cu/ (Zn+Sn)	Zn/Sn	Se/ (Cu+ Zn+ Sn+S)	S/ Se
CZTSSe	0.84	0.99	0.78	0.26
Etched CZTSSe	0.83	1.1	0.69	0.44

The composition of the film in both E and NE scenarios were determined by EDX and the resulting elemental ratios are summarized in Table 3.5. Both NE and E CZTSSe films agree well to earlier studies, in which devices were highly efficient, where the Cu/(Zn+Sn) ratio ranges from 0.8 – 0.85 and the Zn/Sn ratio is 1.0.^{1, 6, 14, 38} The films exhibit Cu-poor, Zn-rich and Sn-poor conditions compared to stoichiometric kesterite CZTSe or CZTS. These ratios have been adopted in literature to produce devices with higher efficiency than those with stoichiometric ratios.^{43, 44} Having Cu-poor films discourages pronounced formation of Cu-rich or Sn-rich secondary phases and increases the growth of Cu-vacancies in the film which are beneficial acceptors for charge. Previous research has also demonstrated an optimal Se/(Cu+Zn+Sn) value of 1.1 which both films agree with.³ The foremost variance between the ratios is the sulfur content between the E and NE films displayed in the last two columns of Table 3.5. The Se/(Cu+Zn+Sn+S) content is reduced from 0.78 to 0.69 after the etching process which corresponds well to the increase in S/Se content from 0.26 to 0.44 after etching. Thus, it is suggested that this surface treatment etches selenium from the surface to expose sulfur that has permeated deeper into the film.

3.3.4 Band gap energy analysis

The optical property of a NE CZTSSe film is evaluated by a Tauc plot conversion of an absorption spectra; the resultant band gap energy is illustrated in Figure 3.8. The band gap of CZTSSe ranges from 1.0 eV to 1.5 eV dependent on the S/Se ratio.^{37, 45, 46} Lower ratios indicate higher selenium content and a bandgap closer to 1.0 eV whereas higher ratios indicate higher sulfur content and a bandgap closer to 1.5 eV.³³ Band gap analyses are not straightforward as the exact value of pure-phase CZTSe is still debated in literature.³¹

However, band tuning of the material is possible by adjusting the elemental composition of the film in addition to the deposition methods used and can range between 0.94 eV and 1.3 eV.^{6, 15, 38, 45, 47} The Tauc plot demonstrates that the NE CZTSSe film has a band gap of 1.22 eV which is an intermediate value between the standards of CZTS and CZTSe. As this material has a bandgap energy closer to the optimal range for photon absorption along with a high absorption coefficient, the device is then expected to have a high efficiency.

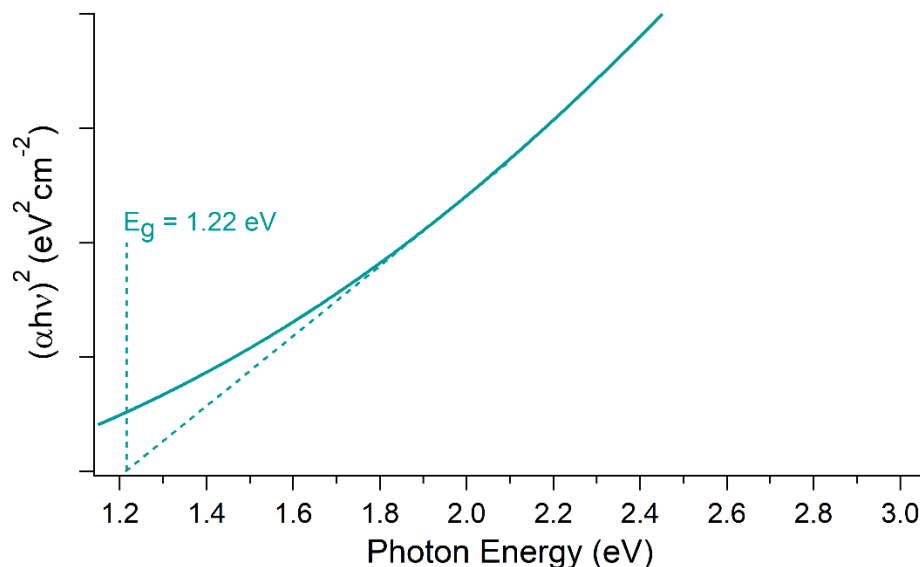


Figure 3.8: Tauc plot of an UV-VIS absorbance measurement. Linear extrapolation to the photon energy illustrates the band gap energy of NE CZTSSe.

3.3.5 Inclusion of buffer layer and full device analysis

A buffer CdS layer is added to the NE CZTSSe to enhance the performance of the film for the full device as demonstrated in *Section 2.3.1*. By the addition of this *n*-type semiconductor, recombination is expected to decrease as a strong p-n junction is created to protect the film and aid in electron transfer. The reactions in solution are explained in *Sections 3.3.1* and *2.3.1*. Figure 3.9 exhibits the PECMs for a NE CZTSSe film before and after the addition of the CdS buffer layer. As the light is turned on, both samples demonstrate an instantaneous increase in current density indicating electron transfer to the methyl viologen. After the addition of CdS, the current density of the film increases nearly four-fold validating the benefit of the buffer layer. For the film without the buffer layer,

the current density is also seen to continuously increase throughout the scan as a charge imbalance is present as discussed previously in *Section 3.3.1*. In contrast, the addition of the CdS layer enables generation of consistent current throughout the scan, suggesting the restoration of charge balance. Also, during the light-on scenarios, recombination is noticeably reduced for the film with the buffer layer which once again establishes that the n-type CdS layer is adept to protecting the film.

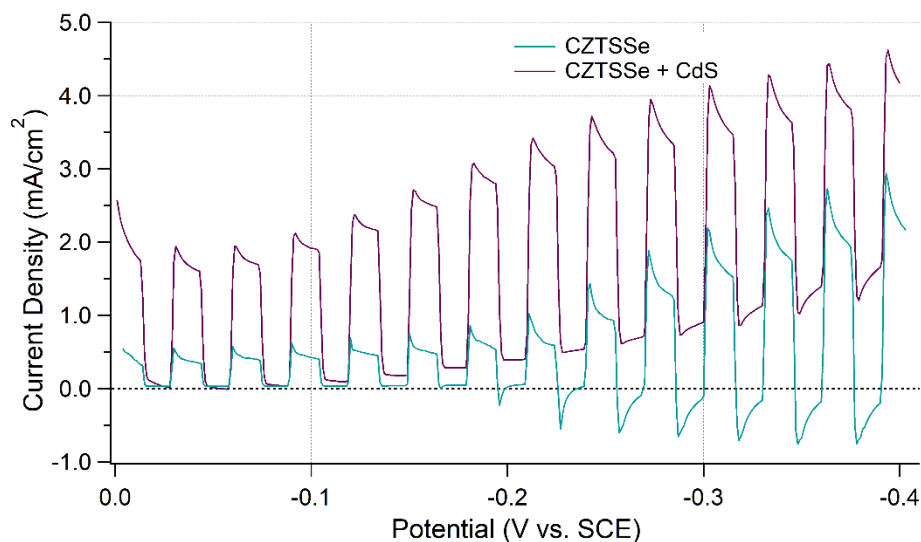


Figure 3.9: PECMs of NE CZTSSe with and without the inclusion of the CdS buffer layer.

When the light is turned off, the current density is expected to promptly drop down to zero current. However, for the CZTSSe film, negative overshoots are observed from -0.20 V onwards implying a continued product separation of charges. Upon the addition of the CdS layer the negative spikes are greatly diminished as the current is held steady in the absence of light. Despite this improvement, the presence of dark current is observed to increase throughout the scan. Dark current refers to unwanted leakage current from the p-n junction in the absence of light which can stem from defects in the film itself. These defects can be intrinsic or at any impurities present in the film potentially due to high temperature fabrication.⁴⁸ If these defects are located in or close to the SCR, recombination in the SCR will increase and generate electron-hole pairs without the assistance of photons thus increasing the dark current.⁴⁸ Solutions to decrease dark current may involve decreasing

the annealing temperature of films before and after the CdS layer or alter surface treatments to refine the absorber layer and better the p-n junction. Nonetheless, the CdS layer provides an enhancement of photocurrent as an increase from 2.80 mA/cm^2 to 3.40 mA/cm^2 is observed after the addition of the buffer layer. This is comparable to resultant CZTS/CdS PECMs attained in *Section 2.3.1*.

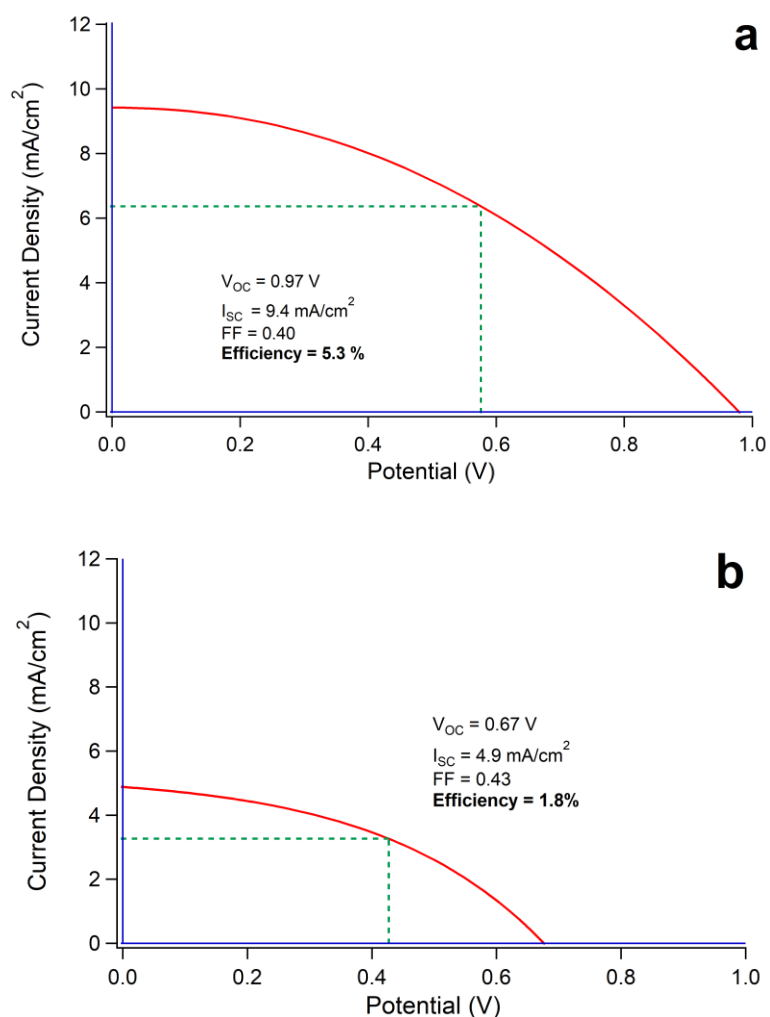


Figure 3.10: J-V curve for champion full devices of a) a NE CZTSSe film and b) an E CZTSSe film. The voltage and current density at maximum power, indicated by the dashed lines highlighted in green, are used to calculate the Fill Factor (FF).

Solar devices were built with both E and NE CZTSSe layers to establish the disparity in performance. Figure 3.10 displays champion devices fabricated with E and NE films. Etching the impurities and altering the composition of the sample could have altered the

E_g and in turn the band offset between the layers. If the offset had decreased, the V_{OC} was expected to decrease along with it.⁴⁹ The J-V curves were measured on an area of 0.20 cm^2 scribed by a razor for both devices. The full device with the NE CZTSSe film shows a high V_{OC} and I_{SC} of 0.97 V and 9.4 mA/cm^2 respectively with a fill factor of 0.40 leading to an efficiency of 5.3%. In contrast, the device with the E film shows an V_{OC} and I_{SC} of only 0.67 V and 4.9 mA/cm^2 respectively with a fill factor of 0.43 leading to an efficiency of 1.8%. The green dashed lines represent the voltage and current density at P_{max} where the maximum power is the point at which the lines meet. The slope in the curve that leads from the I_{SC} to the P_{max} demonstrates shunt resistance and as the slope increases the shunt resistance decreases.

A low shunt resistance allows electrons to flow through alternative pathways causing the current to bleed and in turn lowering the short-circuit current. However, a lower shunt resistance is observed for the NE device suggesting that a high series resistance is the main cause for the loss of power in the E device. Series resistance can be observed by the slope from the P_{max} to the V_{OC} with larger slopes indicative of higher series resistance. Higher series resistance can branch from improper metal back-contact during device fabrication and can in turn lead to a decrease in the conductive properties of the device.⁴⁶ As seen in *Section 3.3.3*, the surface morphology after etching the CZTSSe film was revealed to be highly porous. This increase in porosity is the cause for the decrease in conductive properties and thus poorer photocurrent shown in Figure 3.2. This is also cause for higher series resistance which in turn reduced the V_{OC} .⁵⁰

Table 3.6: Range of characteristic J-V curve parameters, measured over ten working devices for non-etched CZTSSe and etched CZTSSe.

	Efficiency (%)	V_{oc} (V)	FF	J_{sc} (mA/cm^2)
CZTSSe	1.5 – 5.3	0.75 – 1.2	0.35 – 0.47	2.4 – 10.0
Etched CZTSSe	0.53 – 1.8	0.38 – 0.75	0.35 – 0.43	0.46 – 5.8

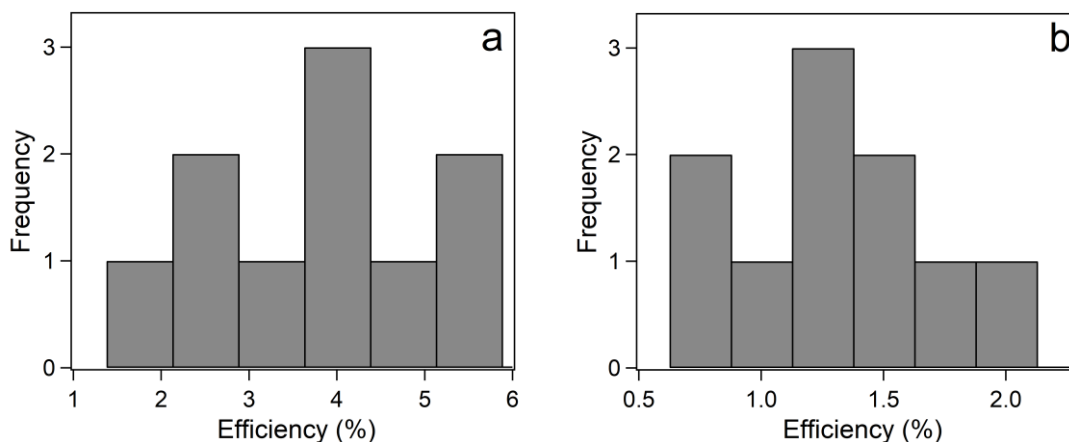


Figure 3.11: Device efficiency histograms for: a) NE CZTSSe and b) E CZTSSe.

Ten full devices for both NE and E scenarios were measured and the statistics for the characteristic parameters are summarized in Table 3.6 and Figure 3.11. The performance of both E and NE CZTSSe devices were lower than average laboratory efficiencies for CZTSe or CZTSSe devices due to the discrepancy in deposition techniques. Many studies analyze films that have been either DC or magnetron sputtered.^{1, 10, 38, 47, 51} This study used multi-step electrodeposition, a technique not widely used, but advantageous as it is an easily controlled technique to alter precursor layers for modifications in elemental composition or surface morphology. The champion NE device is not significantly lower than studies that have achieved efficiencies of 7.0% and 6.2% through DC sputtering and is higher than efficiencies of 3.4% obtained by chemical spraying.^{10, 14, 38, 47} Thus, speaking well to the potential of CZTSSe film produced by a multi-step electrodeposition technique.

For both E and NE devices, the range of efficiencies are illustrated as a histogram in Figure 3.11. The range is narrower than that determined for CZTS NCs in *Section 2.3.6*. Although this material has a lower maximum device efficiency, the narrow range suggests higher potential for higher efficiencies along with an increase in reproducibility of devices. The E devices have an even more narrow range for the measurement parameters, which indicates consistency. However, the reach of the maximum efficiency is much lower than its nanocrystal counterpart. Thus, to improve the possibility or potential of a highly efficient, E CZTSSe device, modifications to the etchant or surface treatments must be investigated.

3.4 Conclusions

In conclusion, CZTSe films were fabricated by electrodeposition of metallic layers followed by high temperature. Electrodeposition followed an earlier procedure that ensured the optimal ratio of Cu/(Zn+Sn) of 0.85 and Zn/Sn of 1.0. Selenization parameters were thereby investigated. Films that were selenized at a temperature of 500 °C with 5 mg/cm² of selenium produced the greatest photoresponse determined by PECMs. It was also discovered that unlike for the CZTS NCs, post-process etching with acetic acid did not enhance the charge carrier flow in the film. The addition of CdS proved to be adept to protecting the film as it improved photoresponse and reduced recombination on the non-etched film.

Through analysis of x-ray diffractograms, it was revealed that contamination from tube furnace had allowed for the substitution of sulfur in lieu of selenium to form CZTSSe layers. The sulfur substitutions happened beneath the surface of the film as etching the surface appeared to remove selenium to expose sulfur. This was confirmed through lattice constants where substitution of sulfur shortened lattice constant *c*. Surface morphology of the films exhibited a porous, disconnected film after post-process etching which in turn would lead to current losses and an increase in recombination sites.

Due to the presence of sulfur, the bandgap energy was shifted towards higher energies at 1.22 eV. The E CZTSSe device attained a V_{OC} , I_{SC} , and efficiency of 0.67 V, 4.9 mA/cm² and 1.8% respectively. The NE device was greatly enhanced to a V_{OC} , I_{SC} , and efficiency of 0.97 V, 9.4 mA/cm² and 5.3% respectively. The NE device had parameters that were within the wide range of efficiencies for laboratory devices, but discrepancies lay within the deposition techniques and surface treatments used in literature. The range of V_{OC} and efficiencies for NE and E CZTSSe devices is narrower than that of CZTS NCs which demonstrates higher reproducibility upon further fabrication enhancements.

3.5 References

1. Márquez, J.; Neuschitzer, M.; Dimitrievska, M.; Gunder, R.; Haass, S.; Werner, M.; Romanyuk, Y. E.; Schorr, S.; Pearsall, N. M.; Forbes, I., Systematic Compositional Changes and Their Influence on Lattice and Optoelectronic Properties of Cu₂ZnSnSe₄ Kesterite Solar Cells, *Sol. Energy Mater. Sol. Cells*, **2016**, *144*, 579-585.

2. Todorov, T.; Hillhouse, H. W.; Aazou, S.; Sekkat, Z.; Vigil-Galán, O.; Deshmukh, S. D.; Agrawal, R.; Bourdais, S.; Valdés, M.; Arnou, P.; Mitzi, D. B.; Dale, P. J., Solution-Based Synthesis of Kesterite Thin Film Semiconductors, *J. Phys. Energy*, **2020**, *2*, 1-21.
3. Chen, Z.; Han, L.; Wan, L.; Zhang, C.; Niu, H.; Xu, J., Cu₂ZnSnSe₄ Thin Films Prepared by Selenization of Co-Electroplated Cu–Zn–Sn Precursors, *Appl. Surf. Sci.*, **2011**, *257*, 8490-8492.
4. Henry, J.; Mohanraj, K.; Sivakumar, G., XRD, AFM, DRS and Photosensitivity of CZTSe Thin Films Prepared by Vacuum Evaporation Method, *Iran. J. Sci. Technol. Trans. A. Sci.*, **2019**, *43*, 1535-1544.
5. Kumar, V.; Singh, U. P., Effect of Selenization Temperature on the Formation of CZTSe Absorber Layer, *Appl. Phys. A*, **2019**, *125*, 1-8.
6. Wang, W.; Winkler, M. T.; Gunawan, O.; Gokmen, T.; Todorov, T. K.; Zhu, Y.; Mitzi, D. B., Device Characteristics of CZTSSe Thin-Film Solar Cells with 12.6% Efficiency, *Adv. Energy Mater.*, **2014**, *4*, 1-5.
7. Li, X.; Zhuang, D.; Zhang, N.; Zhao, M.; Yu, X.; Liu, P.; Weiab, Y.; Renab, G., Achieving 11.95% Efficient Cu₂ZnSnSe₄ Solar Cells Fabricated by Sputtering Cu-Zn-Sn-Se Quaternary Compound Target with Selenization Process, *J. Mater. Chem.*, **2019**, *7*, 1-10.
8. Li, J.; Wang, D.; Li, X.; Zeng, Y.; Zhang, Y., Cation Substitution in Earth-Abundant Kesterite Photovoltaic Materials, *Adv. Sci.*, **2018**, *5*, 1-21.
9. Liu, F.; Wu, S.; Zhang, Y.; Hao, X.; Ding, L., Advances in Kesterite Cu₂ZnSn(S,Se)₄ Solar Cells, *Sci. Bull.*, **2020**, *65*, 698-701.
10. Sahayaraj, S.; Brammertz, G.; Buffière, M.; Meuris, M.; Vleugels, J.; Poortmans, J., Effect of Cu Content and Temperature on the Properties of Cu₂ZnSnSe₄ Solar Cells, *EPJ Photovolt.*, **2016**, *7*, 1-9.
11. Nisika; Kaur, K.; Kumar, M., Progress and Prospects of CZTSSe/CdS Interface Engineering to Combat High Open-Circuit Voltage Deficit of Kesterite Photovoltaics: A Critical Review, *J. Mater. Chem. A*, **2020**, *8*, 21547-21584.
12. Pinto, A.; Shin, S. W.; Aydil, E.; Penn, R. L., Submission of Selective Removal of Cu_{2-x}(S,Se) Phases from Cu₂ZnSn(S,Se)₄ Thin Films, *Green Chem.*, **2016**, *18*, 5814-5821.
13. Wang, K.; Gunawan, O.; Todorov, T.; Shin, B.; Chey, S. J.; Bojarczuk, N. A.; D., M.; Guha, S., Thermally Evaporated CZTSSe Solar Cells, *Appl. Phys. Lett.*, **2010**, *97*, 1-3.
14. Cooper, C. S.; Arnou, P.; Wright, L. D.; Uličná, S.; Walls, J. M.; Malkov, A. V.; Bowers, J. W., An Innovative Approach for Fabrication of Cu₂ZnSnSe₄ Absorber Layers Using Solutions of Elemental Metal Powders, *Thin Solid Films*, **2017**, *633*, 151-155.
15. Simya, O. K.; Geetha Priyadarshini, B.; Balachander, K.; Ashok, A. M., Formation of a Phase Pure Kesterite CZTSe Thin Films Using Multisource Hybrid Physical Vapour Deposition, *Mater. Res. Express.*, **2020**, *7*, 1-12.
16. Turnbull, M. J. Layer-by-Layer Construction Strategies toward Efficient CZTS Solar Cells. University of Western Ontario, Electronic Thesis and Dissertation Repository, 2018.

17. Momma, K.; Izumi, F., Vesta 3 for Three-Dimensional Visualization of Crystal, Volumetric and Morphology Data, *J. Appl. Crystallogr.*, **2011**, *44*, 1272-1276.
18. McDonnell, S.; Addou, R.; Buie, C.; Wallace, R. M.; Hinkle, C. L., Defect-Dominated Doping and Contact Resistance in MoS₂, *ACS Nano*, **2014**, *8*, 2880-2888.
19. Saha, S. K.; Guchhait, A.; Pal, A. J., Cu₂ZnSnS₄ (CZTS) Nanoparticle Based Nontoxic and Earth-Abundant Hybrid Pn-Junction Solar Cells, *Phys. Chem. Chem. Phys.*, **2012**, *14*, 8090-8096.
20. Khoshmashrab, S. Optimization of Cu₂ZnSnS₄ Nanocrystal Composition and Thin Film Fabrication for Photovoltaic Applications. University of Western Ontario, Electronic Thesis and Dissertation Repository, 2015.
21. Ye, H.; Park, H. S.; Akhavan, V. A.; Goodfellow, B. W.; Panthani, M. G.; Korgel, B. A.; Bard, A. J., Photoelectrochemical Characterization of CuInSe₂ and Cu(In_{1-x}Ga_x)Se₂ Thin Films for Solar Cells, *J. Phys. Chem. C*, **2011**, *115*, 234-240.
22. Licht, S.; Bard, A.; Stratmann, M., *Encyclopedia of Electrochemistry, Vol. 6: Semiconductor Electrodes and Photoelectrochemistry*, Wiley - VCH, 2002.
23. Tapley, A. R. Fabrication and Characterization of CuInS₂ and CuInSe₂ Light-Absorbing Thin Films for Use in Solar Cells. University of Western Ontario, Electronic Thesis and Dissertation Repository, 2017.
24. Lai, F. I.; Yang, J.; Y., L.; Kuo, W. S., High Quality Sustainable Cu₂ZnSnSe₄ (CZTSe) Absorber Layers in Highly Efficient CZTSe Solar Cells, *Green Chem.*, **2017**, *19*, 795-802.
25. Park, J. Y., Hong, C.W, Moon, J.H, Gwak, J.H, Kim, J.H, Kim, J.H, Effects of Se/(S+Se) Ratio on Cu₂ZnSn(S_xSe_{1-x})₄ (CZTSSe) Thin Film Solar Cells Fabricated by Sputtering, *CPVR*, **2015**, *3*, 75-79.
26. Vaccarello, D. Fabricating and Characterizing Chalcogenide Thin Films as Light Absorbing Layers in Solar Cells University of Western Ontario, Electronic Thesis and Dissertation Repository, 2016.
27. Lopez-Garcia, J.; Xie, H.; Sylla, D.; Fontané, X.; Blanes-Guardia, M.; Ramos, F.; Espindola, M.; López-Marino, S.; Izquierdo-Roca, V.; Saucedo, E.; Pérez-Rodríguez, A., Influence of the Sulfurization-Selenization Process on CuIn(S,Se)₂ Thin Film Solar Cells from Screen Printing of Oxide Nanoparticle Based Inks, *Mater. Chem. Phys.*, **2013**, *160*, 237-243.
28. Ko, B.-S.; Kim, D.-H.; Hwang, D.-K.; Lee, S.-J.; Kim, J. S., Effects of the Annealing Temperature on the Properties of Sulfur-Graded Cu₂ZnSn(S,Se)₄ Thin Films Grown by a Modified Two-Step Process, *J. Ind. Eng. Chem.*, **2020**, *82*, 406-412.
29. Kim, S.-Y.; Kim, S.-H.; Hong, S.; Son, D.-H.; Kim, Y.-I.; Kim, S.; Ahn, K.; Yang, K.-J.; Kim, D.-H.; Kang, J.-K., Secondary Phase Formation Mechanism in the Mo-Back Contact Region During Sulfo-Selenization Using a Metal Precursor: Effect of Wettability between a Liquid Metal and Substrate on Secondary Phase Formation, *ACS Appl. Mater. Interfaces*, **2019**, *11*, 23160-23167.

30. Ren, G.; Zhuang, D.; Zhao, M.; Wei, Y.; Wu, Y.; Li, X.; Lyu, X.; Wang, C.; Li, Y., CZTSSe Solar Cell with an Efficiency of 10.19% Based on Absorbers with Homogeneous Composition and Structure Using a Novel Two-Step Annealing Process, *Sol. Energy*, **2020**, *207*, 651-658.
31. Salomé, P. M. P.; Malaquias, J.; Fernandes, P. A.; Ferreira, M. S.; da Cunha, A. F.; Leitão, J. P.; González, J. C.; Matinaga, F. M., Growth and Characterization of $\text{Cu}_2\text{ZnSn}(\text{S},\text{Se})_4$ Thin Films for Solar Cells, *Sol. Energy Mater. Sol. Cells*, **2012**, *101*, 147-153.
32. Sun, R.; Zhuang, D.; Zhao, M.; Zhang, N.; Gong, Q.; Wei, Y.; Ren, G.; Wu, Y.; Wei, J., Efficient $\text{Cu}_2\text{ZnSn}(\text{S},\text{Se})_4$ Solar Cells with 79% Fill Factor Using Two-Step Annealing, *Sol. Energy Mater. Sol. Cells*, **2020**, *215*, 1-8.
33. Zeng, C.; Liang, Y.; Zeng, L.; Zhang, L.; Zhou, J.; Huang, P.; Hong, R., Effect of S/(S+Se) Ratio During the Annealing Process on the Performance of $\text{Cu}_2\text{ZnSn}(\text{S},\text{Se})_4$ Solar Cells Prepared by Sputtering from a Quaternary Target, *Sol. Energy Mater. Sol. Cells*, **2019**, *203*, 1-10.
34. Saidi, H.; Boujmil, M. F.; Durand, B.; Bouaïcha, M., Physical Properties of Highly Crystalline Cis Layer Prepared Using Single Phase Electrodeposition and Low Temperature Rtp Annealing, *J. Alloys Compd.*, **2017**, *695*, 779-786.
35. Dimitrievska, M.; Fairbrother, A.; Gunder, R.; Gurieva, G.; Xie, H.; Saucedo, E.; Pérez-Rodríguez, A.; Izquierdo-Roca, V.; Schorr, S., Role of S and Se Atoms on the Microstructural Properties of Kesterite $\text{Cu}_2\text{ZnSn}(\text{S}_x\text{Se}_{1-x})_4$ Thin Film Solar Cells, *Phys. Chem. Chem. Phys.*, **2016**, *18*, 8692-8700.
36. Fouad, S. S.; El Radaf, I. M.; Sharma, P.; El-Bana, M. S., Multifunctional CZTS Thin Films: Structural, Optoelectrical, Electrical and Photovoltaic Properties, *J. Alloys Compd.*, **2018**, *757*, 124-133.
37. Engman, J. Experimental Study of $\text{Cu}_2\text{ZnSn}(\text{Se},\text{S})_4$ Thin Films for Solar Cell Applications. Student Thesis, Uppsala University, 2011.
38. Zoppi, G.; Forbes, I.; Miles, R. W.; Dale, P. J.; Scragg, J. J.; Peter, L. M., $\text{Cu}_2\text{ZnSnSe}_4$ Thin Film Solar Cells Produced by Selenisation of Magnetron Sputtered Precursors, *Prog. Photovolt.*, **2009**, *17*, 315-319.
39. Khare, A.; Himmetoglu, B.; Johnson, M.; Norris, D.; Cococcioni, M.; Aydil, E., "Calculation of the Lattice Dynamics and Raman Spectra of Copper Zinc Tin Chalcogenides and Comparison to Experiments, *J. Appl. Phys.*, **2012**, *111*, 1-9.
40. Lai, F.-I.; Yang, J.-F.; Hsu, Y.-C.; Kuo, S.-Y., Sustainable $\text{Cu}_2\text{ZnSnSe}_4$ Photovoltaic Cells Fabricated with a Sputtered CdS Buffer Layer, *Prog. Photovolt.*, **2020**, *28*, 1012-1023.
41. Kim, S.-Y.; Son, D.-H.; Kim, Y.-I.; Kim, S.-H.; Kim, S.; Ahn, K.; Sung, S.-J.; Hwang, D.-K.; Yang, K.-J.; Kang, J.-K.; Kim, D.-H., Void and Secondary Phase Formation Mechanisms of CZTSSe Using Sn/Cu/Zn/Mo Stacked Elemental Precursors, *Nano Energy*, **2019**, *59*, 399-411.
42. Kim, J.; Kim, J.; Ko, E.; Yoon, S.; Sim, J. H.; Yang, K. J.; Kim, D.-H.; Kang, J.-K.; Song, Y.; Jeon, C.-W.; Jo, W., Carrier Transport and Surface Potential over Phase Variations in the Surface and Bulk of Highly Efficient $\text{Cu}_2\text{ZnSn}(\text{S},\text{Se})_4$ Solar Cells, *Prog. Photovolt.: Res. Appl.*, **2020**, *28*, 1-11.

43. Hsu, W.-C.; Zhou, H.; Luo, S.; Song, T.-B.; Hsieh, Y.-T.; Duan, H.-S.; Ye, S.; Yang, W.; Hsu, C.-J.; Jiang, C.; Bob, B.; Yang, Y., Spatial Element Distribution Control in a Fully Solution-Processed Nanocrystals-Based 8.6% $\text{Cu}_2\text{ZnSn}(\text{S},\text{Se})_4$ Device, *ACS Nano*, **2014**, *8*, 9164-9172.
44. Franckevičius, M.; Pakštas, V.; Grincienė, G.; Kamarauskas, E.; Giraitis, R.; Nekrasovas, J.; Selskis, A.; Juškėnas, R.; Niaura, G., Efficiency Improvement of Superstrate CZTSSe Solar Cells Processed by Spray Pyrolysis Approach, *Sol. Energy*, **2019**, *185*, 283-289.
45. Neuwirth, M.; Seydel, E.; Seeger, J.; Welle, A.; Kalt, H.; Hetterich, M., Band-Gap Tuning of $\text{Cu}_2\text{ZnSn}(\text{S},\text{Se})_4$ Solar Cell Absorbers Via Defined Incorporation of Sulphur Based on a Post-Sulphurization Process, *Sol. Energy Mater. Sol. Cells*, **2018**, *182*, 158-165.
46. Shi Z, A. D.; Jayatissa, A. H., Kesterite-Based Next Generation High Performance Thin Film Solar Cell: Current Progress and Future Prospects, *J. Mater. Sci., Mater. Electron.*, **2017**, *28*, 2290-2306.
47. Kim, Y.-C.; Jeong, H.-J.; Lee, S. K.; Kim, S.-T.; Jang, J.-H., The Effect of S/(S+Se) Ratios on the Formation of Secondary Phases in the Band Gap Graded $\text{Cu}_2\text{ZnSn}(\text{S},\text{Se})_4$ Thin Film Solar Cells, *J. Alloys Compd.*, **2019**, *793*, 289-294.
48. Virmontois, C.; Goiffon, V.; Magnan, P.; Girard, S.; Inguibert, C.; Petit, S.; Rolland, G.; Saint-Pe, O., Displacement Damage Effect Due to Neutron and Proton Irradiations on Cmos Image Sensor Manufactured in Deep Sub-Micron Technology, *IEEE Trans. Nucl. Sci.*, **2011**, *57*, 3101-3108.
49. Yamada, A.; Matsubara, K.; Sakurai, K.; Ishizuka, S.; Tampo, H.; Fons, P. J.; Iwata, K.; Niki, S., Effect of Band Offset on the Open Circuit Voltage of Heterojunction $\text{CuIn}_{1-x}\text{Ga}_x\text{Se}_2$ Solar Cells, *Appl. Phys. Lett.*, **2004**, *85*, 5607-5609.
50. Fella, C. M.; Uhl, A. R.; Hammond, C.; Hermans, I.; Romanyuk, Y. E.; Tiwari, A. N., Formation Mechanism of $\text{Cu}_2\text{ZnSnSe}_4$ Absorber Layers During Selenization of Solution Deposited Metal Precursors, *J. Alloys Compd.*, **2013**, *567*, 102-106.
51. Oueslati, S.; Brammertz, G.; Buffière, M.; ElAnzeery, H.; Touayar, O.; Köble, C.; Bekaert, J.; Meuris, M.; Poortmans, J., Physical and Electrical Characterization of High-Performance $\text{Cu}_2\text{ZnSnSe}_4$ Based Thin Film Solar Cells, *Thin Solid Films*, **2015**, *582*, 224-228.

Chapter 4

4 Fabricating and characterizing electrodeposited $\text{CuIn}(\text{S},\text{Se})_2$ thin film solar cells

This chapter focuses on optimizing $\text{CuIn}(\text{S},\text{Se})_2$ (CISSe) films in order to enhance the photoresponse of the film and full device efficiencies. CISSe was fabricated using galvanostatic electrodeposition followed by selenization. The temperatures for selenization were varied and resultant films were etched with acetic acid for impurity removal. Photoelectrochemical measurements (PECMs) were used to evaluate the photocatalytic ability of the light-absorber-layer and optimize it for later use in full devices. The effect of post-process etching was structurally and compositionally analyzed using XRD and EDX among other conventional characterization techniques. Devices were made with the optimized CISSe film and its efficiencies, before and after etching, were compared to those of the CZTSSe based devices in Chapter 3 and CZTS NC based devices in Chapter 2.

4.1 Introduction

Fossil fuel consumption and greenhouse gas emissions have become an international concern as the environment becomes progressively damaged. Global efforts have been devoted towards renewable resources to lessen the need for fossil fuels. Photovoltaic solar devices are one of the most convenient ways to generate electricity as solar energy is a readily abundant source of energy. In this field, thin films for use in solar cells have become of increasing interest to harvest solar energy although the caveat being the photoconversion efficiency.

Polycrystalline $\text{CuIn}_x\text{Ga}_{(1-x)}\text{Se}_2$ (CIGS) has been a leading material in thin film solar cells due to its highly effective photocoverion with a maximum efficiency recorded as 22.6% in laboratory scale.¹ However, CIGS cells are generally produced with vacuum deposition techniques which are expensive due to high-cost equipment and source materials. Therefore, other thin film materials have been sought out to fit the goals of a low-cost, environmentally friendly candidate for highly efficient devices.

A promising alternative to CIGS is CuInSe₂ (CISe) as it has great optoelectronic properties such as a direct band gap and high light absorption coefficient. Many studies produce CISe films using vacuum deposition or co-evaporation techniques with a maximum efficiency reaching to 17%.² Its related alloy CuIn(S,Se)₂ (CISSe) is also an interesting substitute as the relative content of S/(S+Se) allows for band gap tuning from 1.0 eV to 1.5 eV.^{3,4,5} The *Hillhouse* group has reported the highest CISSe device efficiency of over 13% by drop-casting and spin coating solution-processed CISSe.^{6,7} However, to keep aligned with low-cost goals, an inexpensive and scalable deposition technique is required to commercialize solar cells. Electrodeposition might meet these requirements and be advantageous for many reasons including good control of film composition and morphology based on one-pot electrochemical deposition during a potentiodynamic course.⁸

Maximum efficiency for a CISe and CISSe solar cell fabricated with electrodeposition has been reported to be 8.7% and 11.3%, respectively.^{9,10} Laboratory research explores one step electrodeposition of aqueous baths but is inherently difficult as there is a large difference in reduction potentials for copper, indium and selenium. In this way, sequential electrodeposition of a Cu/In bilayer followed by a selenization process is beneficial in controlling composition.¹¹ In addition, characterization of the photoresponse is one of the essential requirements to determine the effectiveness of the light-absorbing layer. Evaluating the charge-carrier efficiency in the film before production of a full device leads to lowered costs and an insured high photovoltaic efficiency. Photoelectrochemical measurements (PECMs) are a valuable technique to do this by measuring the catalytic conversion of MV²⁺ to MV⁺.^{12, 13, 14, 15}

In this chapter, sequential electrodeposition of Cu/In was used and succeeding selenization parameters were optimized using PECMs. Results were obtained for CISSe samples annealed with selenium and lingering sulfur from the furnace tube during the fabrication process. Variance in selenization temperature as well as post-process surface etching were investigated to corroborate the formation of CISSe and change in relative S/Se content. The effect of these aspects on morphological, optical, structural and compositional properties were analyzed. Full solar devices were manufactured to understand the extent of reproducible, highly efficient CISSe films fabricated by electrochemical deposition.

Unless stated otherwise, procedures were conducted in an open-air environment to aid in low-cost fabrication.

4.2 Experimental

4.2.1 Sequential electrodeposition, selenization & fabrication of full devices

CISSe films were fabricated by sequential galvanostatic electrodeposition of metallic precursors using a Solartron 1287 Potentiostat, succeeded by a selenization process. Molybdenum-coated soda-lime glass (SLG) was purchased from University Wafer (Boston, MA) with a 0.5 μm thickness of Mo and 500 μm thickness of SLG. This Mo-coated glass was used as the back contact in film fabrication. A three-electrode system similar to that mentioned in *Section 3.2.1* was used to deposit the precursors, with the continued use of Mo-coated glass and platinum mesh as the working and counter electrodes respectively. The only modification to the system in this case was the use of the SCE as the reference electrode for all electrochemical baths.

The copper precursor bath was made and deposited exactly following the procedure outlined in *Section 3.2.1*. In brief, the bath, consisting of 25 g/L $\text{CuSO}_4 \cdot 5\text{H}_2\text{O}$, 120 g/L NaOH and, 37.5 g/L D-sorbitol, was deposited onto the Mo-coated glass using a constant current density of 2.5 mA/cm^2 for 90 seconds. An indium sulfamate plating bath was purchased from the Indium Corporation (Clinton, NY) and deposited onto the copper layer using a constant current density of 11.0 mA/cm^2 for 48 seconds. Using Faraday's law, this was calculated to provide an initial Cu/In ratio of 0.6 which was proven to be beneficial to the photoresponse in an earlier study.¹⁶

The film samples then underwent an annealing/selenization procedure similar to the fabrication of CZTSe films. This was done in a Thermo Scientific Lindberg Blue M Tube Furnace with a quartz tube for vacuum and argon purges to -100 kPa and 40 kPa respectively. In summary, the annealing temperature was held at 275 $^\circ\text{C}$ for 20 minutes and selenization temperatures were varied from 400 $^\circ\text{C}$ to 500 $^\circ\text{C}$ in 50 $^\circ\text{C}$ increments with a final temperature of 525 $^\circ\text{C}$. The starting ratio of selenium powder to total surface area was kept to 5 mg/cm^2 as it displayed the highest and most consistent photoresponse in a

previous CIS study.¹⁶ The final films were etched with concentrated acetic acid for 30 minutes to remove surface impurities. Further device fabrication used both non-etched (NE) and etched (E) films.

A buffer layer of cadmium sulfide (CdS) was deposited onto the films via chemical bath deposition as stated in previous chapters. The bath comprised of 103.5 mg cadmium acetate (Sigma-Aldrich, 99.99%), 4.5 mL ammonium hydroxide (Caledon, >99%), 3 mL of 1 M ammonia acetate and 1.5 mL of 0.5 M thiourea in 142.5 mL of MilliQ water at a temperature of 65 °C. The samples were submerged for 7.5 minutes to deposit 50 nm of CdS on the CISE films.

Resultant CISE/CdS films were then placed in the Ultratech/Cambridge NanoTech Savannah S200 Atomic Layer Deposition (ALD) workstation reaction chamber for 10 minutes at 200 °C under vacuum to remove water intercalation. To finish fabricating the full devices, the deposition of both 50 nm ZnO and 250 nm AZO window layers followed a procedure detailed elsewhere.¹⁷

4.2.2 Characterization

The films were characterized by PECMs once again. These were carried out in a solution of 0.05 M MV^{2+} and 0.1 M KCl as previously described in *Section 2.2.2* for selenized CISE and for the half-device following CdS deposition.

After selenization, films were removed from the Mo-coated substrate through physical abrasion and dispersed in isopropanol to 0.5 g/L for absorbance measurements. The band gap energy was obtained using a Cary 50 UV-VIS instrument for absorption spectra, which were then underwent a Tauc plot conversion. Further characterization of both types of CISE films involved examining their elemental composition and crystal structures via SEM (Hitachi TM 3030 Plus Tabletop microscope with an EDX system at 15.0 kV) and P-XRD (Inel CPS Powder Diffractometer with an Inel XRG 3000 Cu X-ray generator and an Inel CPS 120 detector), respectively, using the exact methods described in *Section 3.2.2*. XRD patterns were compared to standards using the ICDD Database and the PDF4+ software (ICDD, PA). Crystal structures were produced using VESTA ver. 3.5.5.¹⁸ Final

device J-V curves were attained with the 150 W Newport lamp with AM 1.5 D filter and collected with the IVIUM CompactStat. Using a power meter, the initial input power from the lamp with the filter was measured to be 0.69 “suns”. All procedures were conducted in an open-air environment, unless stated otherwise, in order to keep fabrication costs low.

4.3 Results and Discussion

4.3.1 Refining conditions for selenization via PECMs

PECMs were used once again to investigate the quality of the film based on its photocatalytic conversion of incident photons into useful photocurrent. Selenization temperatures of 400 °C, 450 °C, 500 °C and 525 °C were tested and the corresponding PECMs are shown in Figure 4.1 with the range of photocurrents summarized in Table 4.1. Temperatures under 400 °C were not tested due to the lack of photoresponse and the inability to effectively deposit selenium powder on the Cu/In stacks. Principally, the photoresponse increases with temperature apart from Sample 8 in Figure 4.1d. All samples also display a higher photoresponse than those achieved in Chapter 3 for CZTSe films. Sample 5 in Figure 4.1a and Sample 6 in Figure 4.1b have comparable photoresponse, as the maximum current densities achieved were 0.70 and 1.0 mA/cm², respectively. Both measurements retain a near square wave at near zero potentials. However, as the bias becomes increasingly negative, current transients in both the light-on and light-off scenarios are observed.

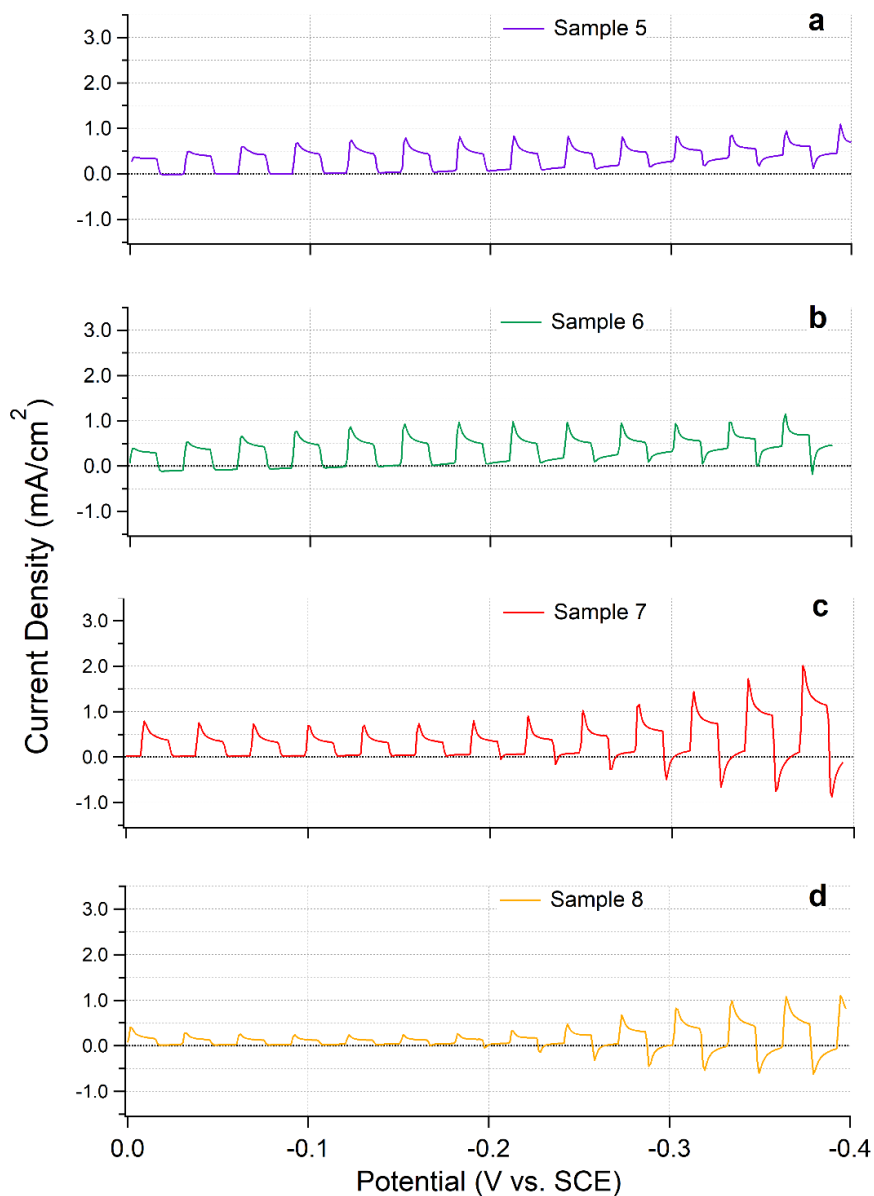


Figure 4.1: Photoelectrochemical measurements for CISE films fabricated with 5 mg/cm² of selenium at selenization temperatures of a) 400 °C, b) 450 °C, c) 500 °C and d) 525 °C.

In general, *p*-type semiconductors such as CISE have electrons that are transferred from their conduction band to the solution-phase oxidant MV^{2+} , and thus the observed current is reductive.⁴ The exponential decay observed immediately after the light-on scenario indicates surface recombination processes and anodic current as MV^+ is re-oxidized at the surface.¹² The ongoing reactions in the electrolyte solution upon illumination have been

conferred extensively in the previous chapters. At a potential of -0.27 V, both Sample 5 and 6 start to experience cathodic current transients at the light-off scenarios. This is due to reduction of the photogenerated MV^{2+} to MV^+ at any exposed Mo substrate or impurities in the film.^{12, 16} A concept discussed in Chapter 3 is the increase in photoresponse with increasingly negative biases. As both Samples 5 and 6 have consistent photoresponse throughout the scan, it is assumed that both of these films are already saturated with electrons and there is no need to restore the charge balance in solution.¹⁹

Figure 4.1c showcases the PECM for a CISE film fabricated at 500 °C and demonstrates the highest maximum photocurrent achieved of the four samples at 2.35 mA/cm². The photocurrent increases drastically with increasingly negative applied biases until -0.37 V where it decreases slightly, suggesting that this is the point at which the film is perfectly saturated with electrons. Sample 7 also exhibits anodic current transients at most potentials, suggesting surface recombination, as well as dark anodic spikes and cathodic currents from -0.30 V onwards. The negative spikes at light-off scenarios signify that more MV^+ was produced upon illumination resulting in continued production of MV^{2+} during light-off scenarios at any exposed Mo substrate or impurities in the film.¹² At potentials lower than -0.30 V, there is reduced surface recombination which correlates well to the point of electron saturation in the film. The restoration in a near square wave along with the high photoresponse are indicative of higher quality and a stable film.

Table 4.1: Range of photocurrent as a function of selenization temperature determined by PECMs in Figure 4.1.

	Selenization temperature	Photocurrent range
a): Sample 5	400 °C for 30 min.	0.45 - 0.70 mA/cm ²
b): Sample 6	450 °C for 30 min.	0.50 - 1.00 mA/cm ²
c): Sample 7	500 °C for 30 min.	0.75 - 2.35 mA/cm ²
d): Sample 8	525 °C for 30 min.	0.35 - 1.05 mA/cm ²

Sample 8 in Figure 4.1d decreases in photoresponse from Sample 7 and reaches a maximum photocurrent value nearly identical to that of Sample 6 at 1.05 mA/cm^2 . The trace of Sample 8 closely mimics that of Sample 7 but at a lower magnitude. The PECM illustrates an increase in photocurrent with more negative bias and does not become saturated with electrons until -0.35 V . Throughout the scan, Sample 8 displays surface recombination at the light-on scenarios and begins to show continued product separation at the light-off scenarios at -0.25 V . The reason for the decrease in photocurrent may be due to the selenization temperature. Commonly with increasing temperature, crystallization of the film could increase to protect the film from current loss.²⁰ However, *Yeranyan et al.* studied CIS films fabricated via magnetron sputtering and established that at higher temperatures the potential growth for secondary phases such as Cu_xSe was increased.²¹ These secondary phases can inhibit the photoresponse of the film and in turn negatively affect the efficiency of a device. As Sample 7 had the highest overall photoresponse, $500 \text{ }^\circ\text{C}$ was used as the selenization temperature for further film fabrication.

The ideal selenium concentration for a CISE film have been explored in previous studies; however, the temperatures used to fabricate those films have been found to be too high which can cause indium levels in the film to decrease throughout the selenization process.²² Low levels of indium produce a Cu-rich film which in turn leads to poorly performing films. Therefore, in a similar fashion to that in Chapter 3, films were tested at various selenization temperatures along with post-process etching to determine the best conditions to improve the film. The starting ratio of Cu/In deposition was kept at 0.6 as higher starting Cu/In ratios had binary copper selenide phases that remained in the film, and lower starting Cu/In ratios had unreacted binary indium selenide phases.^{16, 22} The starting mass-to-area ratio of selenium was kept at 5 mg/cm^2 as this was previously proven to yield the maximum photoresponse and have good adherence to the back contact.¹⁶

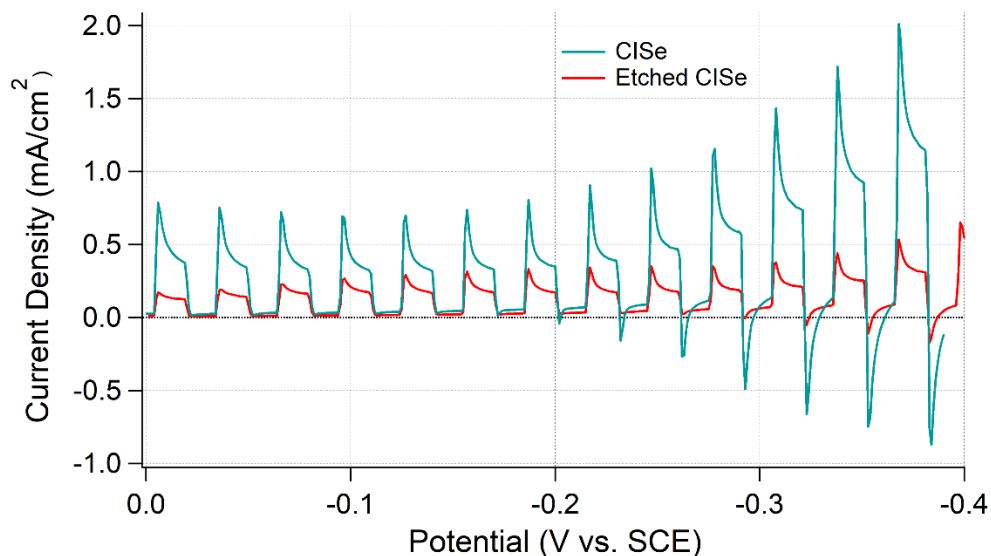


Figure 4.2: Photoelectrochemical measurements of CISe films fabricated with 5 mg/cm² selenium at 500 °C in E and NE scenarios.

As the selenium concentration has already been explored and optimized in previous work, the effect of etching to remove possible Cu_xSe secondary phases was studied. Figure 4.2 features PECMs of CISe films fabricated at 500 °C and exhibits both post-process and no post-process etching. Both traces show similarities in shape, with the E trace showing more of a square wave at near zero potentials, whereas the NE trace displays more surface recombination. In both cases, the photoresponse increases with more negative bias and does not become saturated with electrons by the end of the scan; this is more prominent in the NE trace. The reactions and the rates at which they occur have been examined extensively in previous chapters. Surface recombination largely dominates at the light-on scenarios, and the cathodic transients at light-off scenarios imply continued product separation at the exposed Mo substrate.^{12, 16, 23}

While both anodic and cathodic transients are more prominent in the NE film, the greatest disparity between the two traces is the maximum photocurrent achieved, as the NE CISe film attains 2.35 mA/cm² while the E CISe film only reaches 0.70 mA/cm². This is consistent with the results in *Chapter 3* for the CZTSe film but in contrast to the results in *Chapter 2* for the CZTS NCs. *Colombara et al.* studied the effect of etching on Cu-poor versus Cu-rich films and determined that Cu-rich films were more susceptible to reap the

benefits of etching compared to Cu-poor films upon etching, which showed photocurrent decrease.²⁴

An argument discussed in *Chapter 3* for the reduction in photoresponse is that selenium on the surface is removed by the etchant. With the argument from *Colombara et al.*, this is more probable due to the Cu-poor nature of the electrodeposited film. Another rationale is that the Cu_xSe is being etched off; however, this secondary phase is very conductive and by its removal, the current through the film is diminished.²¹ Additional testing and characterization of the film was required to conclude elemental and electrical changes in the film for various temperatures and post-process etching. For further device fabrication, CISe films were made with 5 mg/cm^2 of selenium at a temperature of $500 \text{ }^\circ\text{C}$ with no post-process etching.

4.3.2 Structure of CISe film via x-ray diffraction

X-ray diffraction was utilized to determine the structure of the CISe films at each selenization temperature. Thermal annealing that precedes the selenization process ensures good crystallinity and sharper peaks in the diffractograms.^{25, 26, 27} The diffractograms displayed in Figure 4.3 also give insight into crystal size and the crystallinity of the film at temperatures from $400 \text{ }^\circ\text{C}$ to $525 \text{ }^\circ\text{C}$. In Figure 4.3, the standard diffractograms for CIS (JCPDS# 01-085-1575) and CISe (JCPDS# 00-040-1487) are also included for clarification. The characteristic chalcopyrite peaks corresponding to the planes (112), (220) and (312) for the standards are at 26.67° , 44.17° , and 52.38° for CISe and 27.91° , 46.33° , and 55.08° for CIS. Samples 5 – 8 all display the presence of Mo (JCPDS# 00-004-0809), a chalcopyrite structure, and no other peaks attributed to common secondary phases such as Cu_xSe or In_2Se_3 , suggesting a pure phase film. With materials in previous chapters, the construction of the film not only included a two-step fabrication process but also multi-step electrodeposition, whereas for CISe, there is one less electrodeposition step involved. This benefit in the fabrication process allows for a more refined film, as can be seen in the diffractograms below.

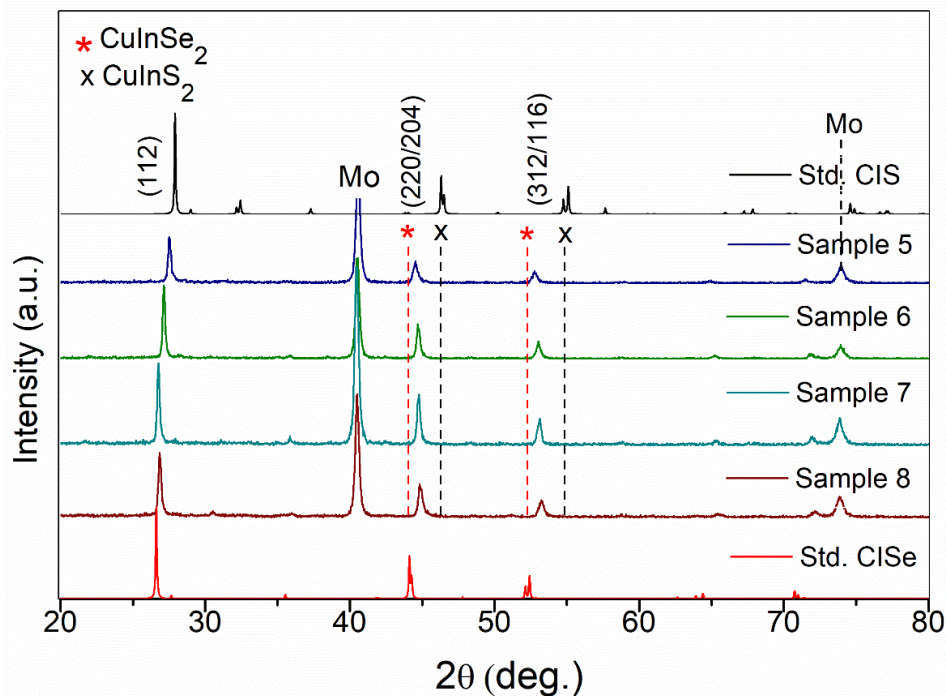


Figure 4.3: XRD diffractograms for CISe Samples 5 – 8. The three most characteristic peaks are labeled with a colour legend included within the figure. Red dashed lines indicate standard peaks for CISe and black dashed lines indicate standard peaks for CIS.

Akin to the CZTSe films in *Section 3.3.2*, there is a shift amongst the three major crystallographic reflection peaks as the temperatures increased due to possible sulfur contamination during the selenization process.^{28, 29} Samples 5 – 8 demonstrate intermediate peaks between the standard CIS and CISE phases which indicate the existence of kesterite $\text{CuIn}(\text{S},\text{Se})_2$ or CISSe in the samples. This is easily seen with the (112) peak but is also observed for the (220/204) and (312/116) reflection peaks. Apart from Sample 8, the most intense peak at (112) shifts toward the CISE phase as the standard peaks for CIS are at larger angles. Absence of distinct (211) and (101) peaks in the diffractograms are indicative of non-stoichiometric compositions in the films.³⁰

The lack of dual peaks for both selenium and sulfur suggest that sulfur atoms are interposed into the film by sulfur substitution at selenium sites.^{5, 16} Substitution of selenium by sulfur is reliant on the stability of the film at a certain selenization temperature. The substitution

of sulfur appears thermally favoured while the substitution of selenium is dependent on temperature. Thus, at lower temperatures, the CISe compound is not stable and so selenium atoms can easily be replaced by sulfur, whereas at higher temperatures, the compound is more stable, allowing a more Se-rich compound to exist. This can provide a selenium-rich back but a sulfur-rich surface.^{5, 10}

The relative S/(S+Se) content can be determined from the (112) intermediate peak using *equation 3.1*.³¹ The linear factor *A* in the equation for this material equates to 1.24, as it is the difference between the standard (112) reflection peaks of CIS (27.91°) and CISe (26.67°). The resultant values are summarized as percentages in Table 4.2 with the smallest percentage indicative of the highest selenium content in the sample. These values show that at lower temperatures, selenium is easily replaced by sulfur, since at 400 °C the relative S/(S+Se) content is at its highest at 69.0%. At 500 °C, the CISe layer has the greatest stability to prevent sulfur substitution as the relative S/(S+Se) content is reduced significantly to 8.0%. The intermediate (112) peak angle of every sample was also used to estimate the average grain size, lattice strain and dislocation density using *equations 3.2 – 3.4* expressed in *Section 3.3.2*.^{32, 33}

Table 4.2: XRD parameters for Samples 5 – 8 through the (112) reflection peak for various selenization temperatures where the standard (112) peak for CISE is at 26.67°.

	Selenization temperature	Bragg angle (2θ)	FWHM (rad)	Grain size (nm)	Lattice strain (ϵ) $\times 10^{-3}$	Dislocation density (δ) (nm^{-2}) $\times 10^{-3}$	$\frac{[S]}{([Se] + [S])}$ (%)
Sample 5	400 °C	27.53°	0.0046	31.0	1.1	1.0	69.0
Sample 6	450 °C	27.14°	0.0039	36.0	0.96	0.77	38.0
Sample 7	500 °C	26.77°	0.0037	39.0	0.90	0.68	8.0
Sample 8	525 °C	26.86°	0.0047	31.0	1.1	1.1	15.0

The grain size follows the trend of increasing with temperature, with the exception of Sample 8 once again. This decrease in grain size can be attributed either to the increase in sulfur content, as sulfur is a smaller atom than selenium, or to high temperatures causing damage to the cell.³⁴ The Sample 8 exclusion holds true for the FWHM decreasing with increasing temperature as well. As the crystallite size decreases, the peak width increases due to Scherrer broadening, this can be seen from correlating the FWHM to the grain size.³⁵ Narrowing of the FWHM with increasing temperature indicates a crystalline nature of the films which corresponds well to the increase in grain size to ensure fewer breaks in the film are present. Dependent on the Bragg angle and grain size, are the lattice strain and dislocation density. As the grain size increases, the number of holes and breaks in the film should theoretically reduce, allowing for less lattice strain and lattice deformities or dislocations.³² This is seen with Sample 7 as it has the highest grain size and lowest

S/(S+Se) content, permitting less sulfur substitutions or dislocations in the crystal lattice as well as the least amount of lattice strain in the film. These parameters provide an explanation as to why Sample 7 had an increase in PECM photoresponse.

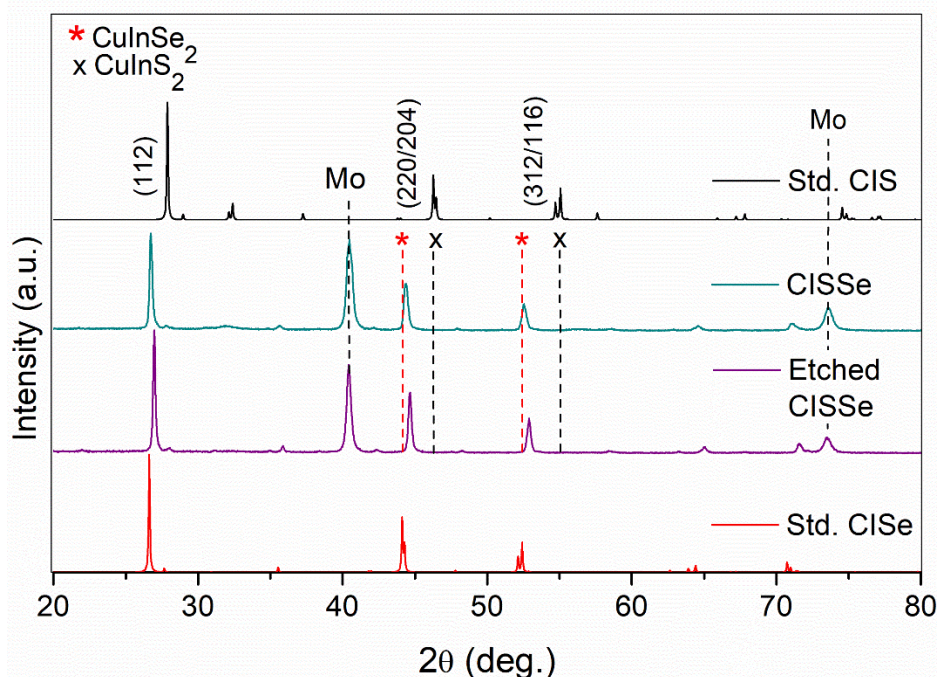


Figure 4.4: XRD diffractograms for CISSe in both NE and E scenarios. The red and black dashed lines represent the standard CISe and CIS peaks, respectively, while the three major crystallographic peaks are labeled.

Figure 4.4 displays XRD patterns for CISSe films in both NE and E scenarios that were analyzed to explain the disparity in performance. Both traces show the three characteristic chalcopyrite peaks corresponding to the (112), (220/204) and (312/116) planes. Interestingly, both traces also show good agreement to the standard CISe phases in comparison to the standard CIS phases with no other secondary phase peaks. From Table 4.2, both traces should have minimal sulfur substitution and larger grain size as the samples were derived from Sample 7. The major dissimilarity between the NE and E diffractograms is a right-shift of the (112) peak from 26.76° in the NE film to 26.94° in the E film. The etching process was speculated to etch off any impurities or secondary phases such as Cu_xSe or In_2Se_3 residing on the surface to produce a refined and crystalline film. Instead what is seen is a shift toward higher 2θ , potentially due to selenium on the surface being

etched off and exposing sulfur that has penetrated deeper into the CISSe layer. With a copper stoichiometric films, grains may grow from top-down resulting in higher sulfur concentration near the back of the film.³⁶

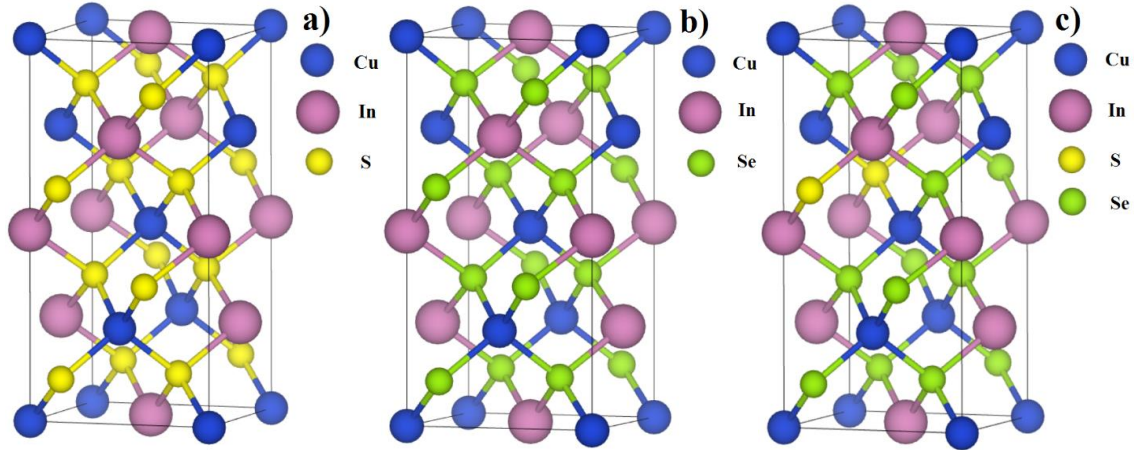


Figure 4.5: Crystal structures for: a) standard CIS, b) standard CISE and c) an estimate of CISSe with 12.5% sulfur incorporation.

Table 4.3: Chalcopyrite lattice constants for standard CIS, CISE and experimental CISSe films in both E and NE scenarios.

	Lattice constants a & b	Lattice constant c
Std. CIS	5.52 Å	11.13 Å
Std. CISE	5.78 Å	11.62 Å
CISSe	5.78 Å	11.48 Å
Etched CISSe	5.73 Å	11.44 Å

In chalcopyrite structures, the lattice constants a and b are equal while c is different, and so lattice constants a and c can be calculated using *equation 3.5* expressed in *Section 3.3.2*.³³ The resultant constants in comparison to the standards are summarized in Table

4.3. Crystal structures for standard CIS, CISE and an estimation of CISSe are illustrated in Figure 4.5. For the NE CISSe film, the lattice parameter a matched well to the standard CISE, while for the E film, the lattice constant a is more of an intermediate value between the CIS and CISE standard values.^{37, 38} In both scenarios for the film, the lattice constant c is smaller than its theoretical counterpart and is once again an intermediate value. This is directly related to the shift in the (112) reflection of the film and may be due to localized distortion, proving once again that with smaller lattice constants, the more sulfur substitutions there are, as sulfur is a smaller atom than selenium.^{39,40} This increase in sulfur contamination could explain the reduction in photoresponse by the E films, but further compositional analysis is required to conclude this.

4.3.3 Composition and morphology via SEM/EDX

Figure 4.6 showcases SEM images taken before and after etching with acetic acid to give insight into the surface morphology of the films. Additionally, the composition of the films before and after etching was evaluated by EDX to assist in explaining the diffractogram shifts seen in Figure 4.4. The larger images with a scale of 50 μm provide an overview of the film surface while the insets with a 10 μm scale display the surface morphology in greater detail. On the surface of the overview, the NE film shows a smoother surface with less void formation in comparison to the E film. A smoother surface is generally needed for well performing light-absorber-layer in solar cell applications as it promotes efficient charge transfer across the surface.^{26, 36}

Upon magnification in Figure 4.6a it is observed that the NE film is comprised of tightly packed granular structures largely varying in size. Figure 4.6b showcases the E film in which the overview looks rougher and contains more pinholes than the NE film. The decrease in selenium content can attribute to the surface roughness and grain size in the E film.⁴¹ Once magnified, the E film appears to be significantly more porous and loosely packed. As the deposition and selenization conditions were kept constant, this change between the packing of granular structures in the films can be attributed to the etching process. The difference in photoresponse between the NE and E films can then be traced back to the quality of the film and the electrical connectivity on the surface, as loosely packed or porous films will see a decline in efficient current being generated.^{16, 42}

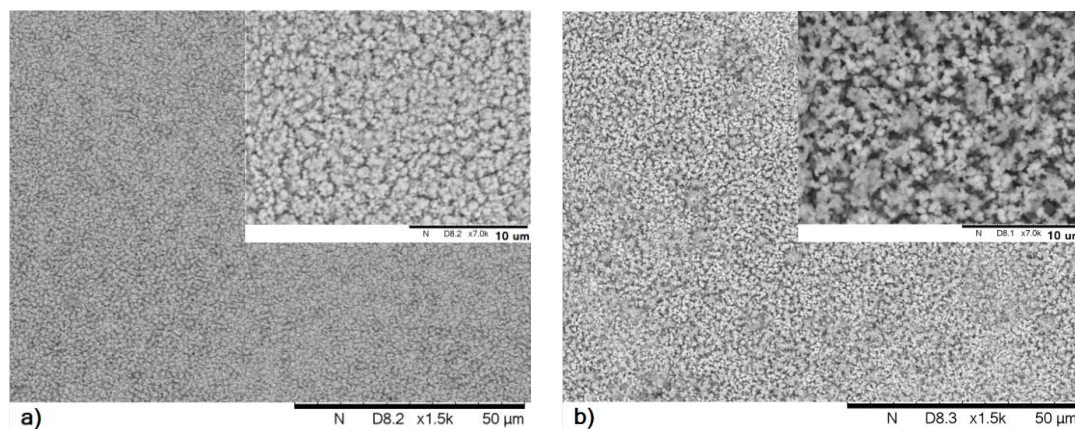


Figure 4.6: Surface SEM images of a) a NE and b) an E CISSe film. The larger image has a scale of 50 μm whereas the inset has a scale of 10 μm .

Table 4.4: Relative molar ratios of NE and E CISSe films measured by EDX.

	Cu	In	Se	S
CISSe	0.62	1.00	2.3	0.12
Etched CISSe	0.71	1.00	2.1	0.24

The elemental composition of the CISSe films were estimated from EDX and expressed in Table 4.4. In previous studies, it was determined that films with a Cu/In ratio of 0.6 had the best performance in comparison to higher Cu/In ratios that suggested a more copper-rich film.¹⁶ In literature, it has been suggested that the reduction of copper content in CIS films improves the optical properties as it results in fewer defects that inhibit recombination.⁴³ The NE film displays an optimal ratio of Cu/In at 0.62 and corroborates previous findings. It also shows a higher-than-stoichiometric selenium content but with two-step fabrication processes, stoichiometric values are harder to obtain and may not necessarily be the best for the performance of the film.²³ In contrast, the E film shows a higher Cu/In ratio at 0.71 due to the etching process and the potential loss of indium at high

temperatures. The relative molar ratios for the E CISSe are closer to stoichiometric values; however, the sulfur content is seen to increase as the selenium content decreases after the etching process. This corroborates the speculation that selenium on the surface is etched off to expose sulfur that has congregated deeper into the film.

4.3.4 Band gap energy analysis

The optical property of the NE CISSe film was studied the conversion of a UV-VIS absorption spectrum to a Tauc plot at room temperature. The band gap energy is obtained from this graph by extrapolating the linear portion of $(\alpha h\nu)^2$ to intercept the x-axis. The linear behaviour of the Tauc plot indicates that the film has a direct band gap and it was determined to be 1.17 eV. This is in between the standards of CIS and CISE which are generally around 1.49 eV and 1.02 eV, respectively.¹⁰ While the experimental value is bowed toward standard CISE, many factors can change or shift the band gap energy, such as temperature and grain size. Deviations from stoichiometric compositions may also account for a lower E_g .⁴⁴ Previous studies have shown that the deposition methods, electrodeposition parameters and the sulfur content can also drastically change the band gap energy.^{10, 28, 33, 40, 45, 46} Selenization at high temperatures has been shown to increase the grain size in the film and shift the band gap to higher energies. Larger band gaps are, however, beneficial as they are closer to the optimal region for photocoverion of solar devices.

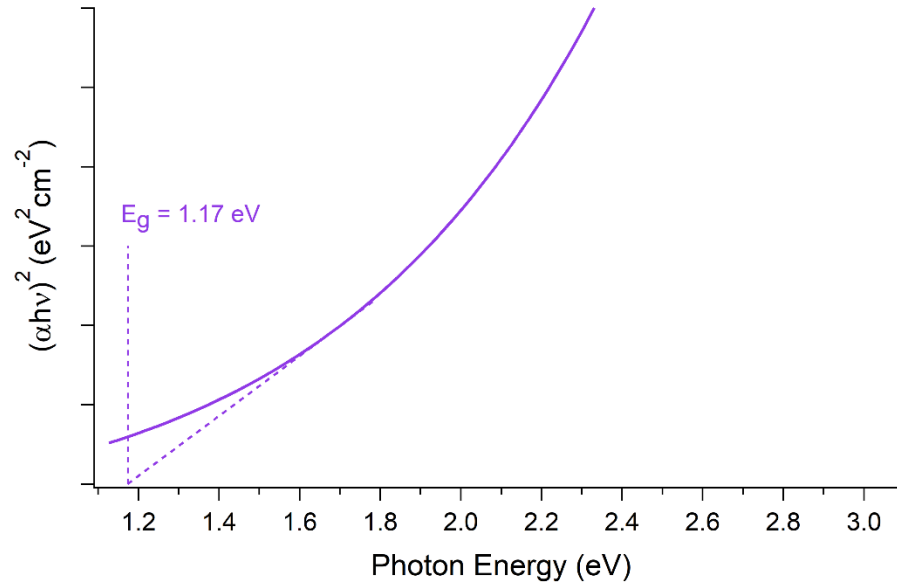


Figure 4.7: Tauc plot of the UV-VIS absorbance measurement showing the band gap for NE CISSe.

4.3.5 Full device completion and analysis

After film fabrication, the next step in solar device manufacturing is the addition of the CdS buffer layer. The purpose of adding an n-type buffer layer is to facilitate electron transfer between layers to enhance the photocurrent produced. This improvement by the CdS has been shown in *Sections 2.3.1* and *3.3.5* and is expected to protect the absorber layer from further degradation or oxidization that may reduce the photoresponse. Figure 4.8 exhibits the PECM for a NE CISSe film along with the addition of CdS on top of the NE film. Throughout the scan, the current density increases with progressively negative bias for both samples due to the imbalance of charge in the solution. Recombination and continued product separation are demonstrated by the spikes and negative overshoots during the light-on and light-off scenarios, respectively. The reactions that occur in solution have been discussed extensively in *Sections 4.3.1* and *2.3.1*. The maximum current density that the NE CISSe film produces is 2.35 mA/cm^2 . In addition to the photocurrent enhancement, a reduction in recombination was observed after CdS was added, as expected. At potentials closer to zero, there is minimal recombination during the light-on scenarios. As the scan progresses toward more negative potentials, the recombination does grow, but at a reduced rate. However, negative overshoots indicating continued product

separation begin at -0.25 V at a higher rate than the film without the CdS layer. This corresponds with the slight increase in dark current observed from -0.25 V onwards. Nevertheless, the photocurrent increases to 3.30 mA/cm² upon the addition of the buffer layer and is comparable to the results obtained in *Sections 2.3.1* and *3.3.5*.

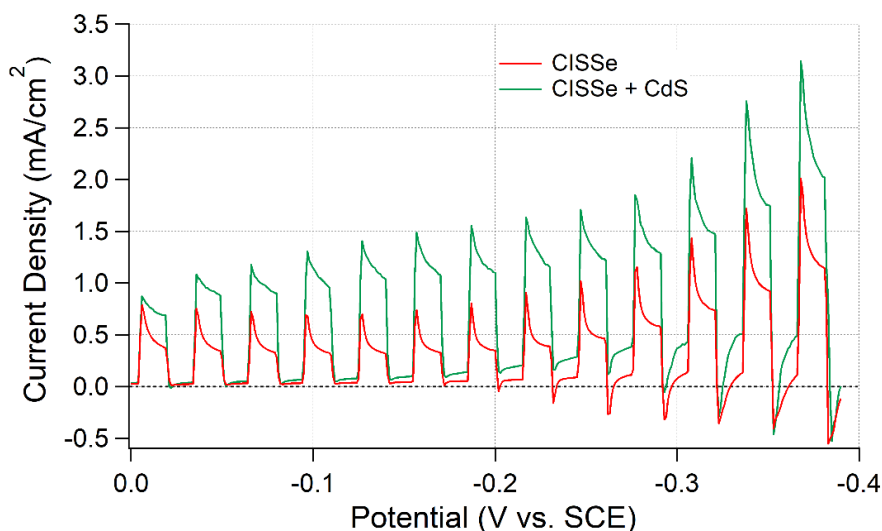


Figure 4.8: PECMs of NE CISSe with and without the addition of the CdS layer.

As proof of concept, full solar cells were built with both E and NE CISSe films. The champion devices for each scenario are showcased in Figure 4.9 where the area measured for both devices is 0.15 cm². Similar to the CZTSSe, the change in composition after etching could have enhanced the E_g and in turn the lower band offset between the layers. Thus, as the electric field relaxes with decreasing band offset, the V_{OC} is predicted to decrease after etching.⁴⁷ The NE champion device achieved a maximum efficiency of 2.1% with an open-circuit potential of 0.93 V and short circuit current of 3.9 mA/cm². The E champion device achieved a maximum efficiency, open-circuit potential and short circuit current of 0.88%, 0.52 V and 3.4 mA/cm², respectively. On the J-V curve, the maximum current and voltage at maximum power are represented by the dashed green lines, where the maximum power is the point at which the lines meet. Both Figures 4.9a and b display low shunt resistance as seen by the slope of the curve from the short-circuit current to the maximum power point. This low shunt resistance can provide additional alternative pathways for current which in turn accounts for lower photocoverion efficiency. This

feature is more prominent in the E device where particle size is smaller in the film, and the compactness of grains was a concern.

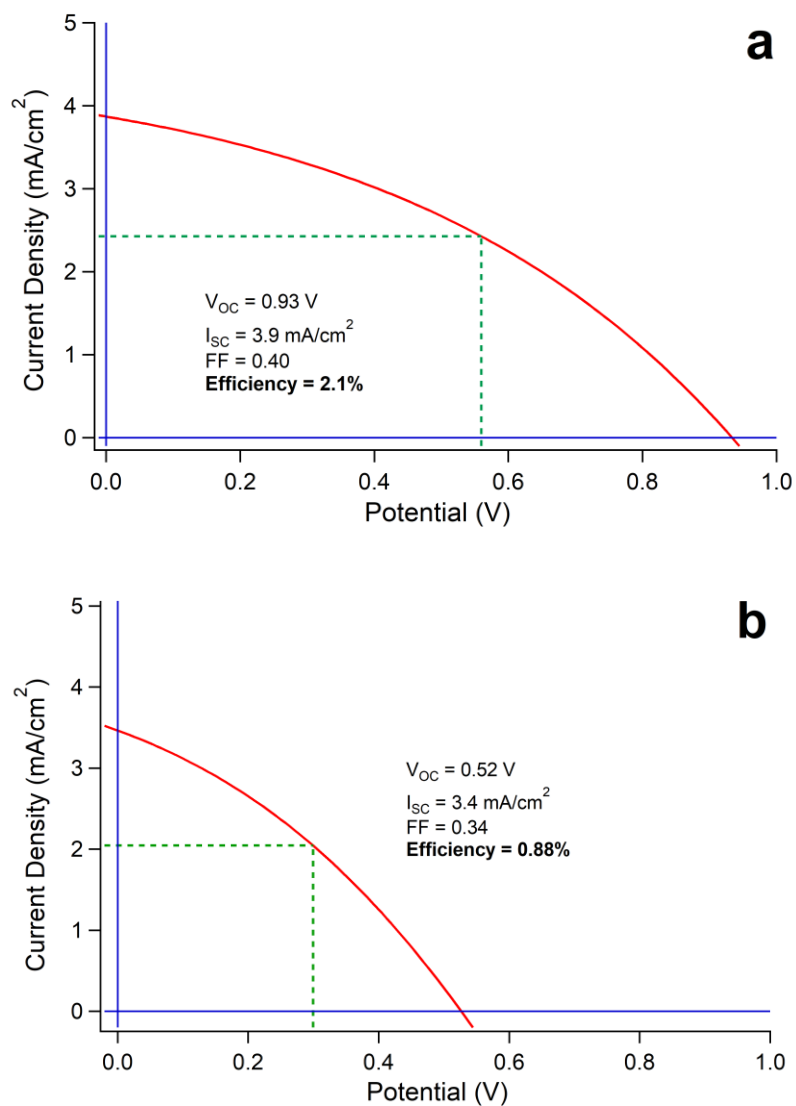


Figure 4.9: J-V curve of the a) champion NE CISSe full device and b) champion E CISSe full device. The current density and voltage at maximum power are indicated by the green dashed lines used to calculate the Fill Factor.

As illustrated in Figure 4.6, the film became more porous and less compact once etched which can lead to degradation of the CISSe attachment to the back contact. The worse back contact the device has, the more likely the efficiency of the device is below 1%, as it is indicative of high series resistance.⁵ Since the series resistance and short-circuit current

appear to be similar in both champion devices, the decrease in efficiency is then mainly associated with the decrease in open-circuit potential and fill factor. Both parameters are negatively impacted by poor crystalline quality, film roughness and degradation of the back contact.^{5, 42, 48} There are many other factors that can contribute to the reduction of device efficiency; however, smaller grain size invites increased recombination on the grain boundaries and leads to a poor heterojunction between layers due to the roughness of the individual layers.⁴⁹ The E device can testify to this fact as the E film displayed increased porosity that could have led to electrical losses on the absorber/buffer interface. Device efficiency could be improved with optimization of surface treatment conditions and procedures.

Table 4.5: Measurement statistics of J-V curve parameters for ten working devices of both non-etched CISSe and etched CISSe.

	Efficiency (%)	Voc (V)	FF	Jsc (mA/cm ²)
CISSe	1.1 – 2.1	0.70 – 0.93	0.36 – 0.42	2.7 – 3.9
Etched CISSe	0.71 – 0.88	0.42 – 0.57	0.31 – 0.38	2.7 – 4.8

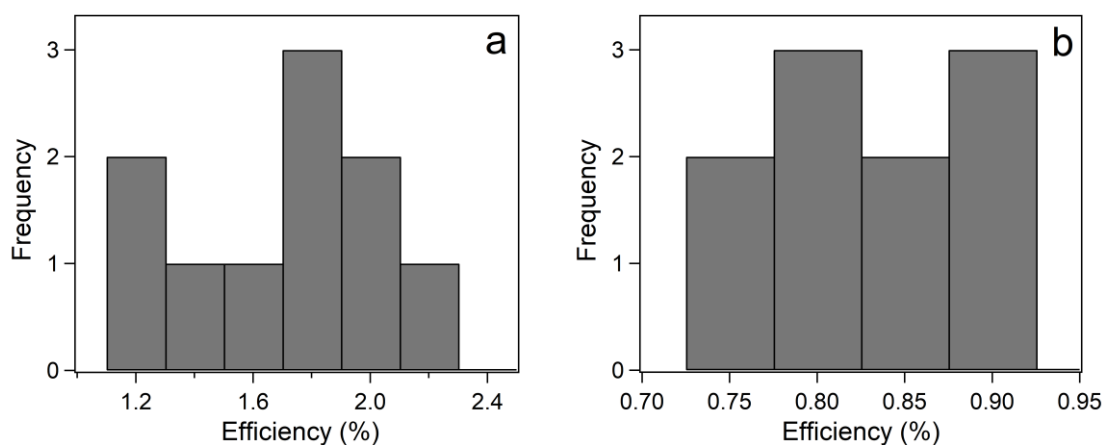


Figure 4.10: Final device efficiency histograms of: a) NE CISSe and b) E CISSe.

The statistics for measurement parameters from ten full devices for both non-etched and etched cases can be seen in Table 4.5 and Figure 4.10. The overall performance of the CISSe devices is lower than the average research efficiencies; however, the deposition techniques in studies vary considerably from quantum dots to spin coating.^{5, 40, 50, 51} The reported range of efficiencies in the table is also lower in magnitude compared to devices made by means of electrodeposition.^{11, 42, 49} A possible reason for this is that many studies involve one-pot electrodeposition wherein all of the precursors are added into the same bath. The difficulty with this lies in optimizing the deposition current or potential, as reduction potentials vary between additives.⁵²

Multi-step electrodeposition can bypass this problem as its advantage is the ability to easily control the deposition and elemental ratios.⁵³ The caveat with this technique is an increased probability of layer segregation which can lead to poorer photocurrent and device efficiency. From the histograms presented in Figure 4.10, CISSe devices have a narrow range of efficiencies which speaks well to its reproducibility. In contrast, the CZTS NCs in *Section 2.3.6* exhibited a much larger range for efficiency which shows good potential but poor reproducibility. With high reproducibility, the CISSe film carries a great deal of potential to achieve scalable and efficient devices in comparison to the materials discussed in earlier chapters.

4.4 Conclusions

The selenization process and post-process etching were investigated. The objective of varying selenization parameters was to prevent indium losses and increase photoresponse of the films. Utilizing PECMs, it was determined that non-etched CISE films selenized at a temperature of 500 °C with 5 mg/cm² of selenium obtained the greatest photoresponse. Addition of the buffer layer demonstrated an improvement in PECMs for the non-etched film. Degradation of the film is continued to be seen as recombination was present at both light-on and light-off scenarios.

Structural determination via XRD confirmed that sulfur contamination had occurred, and the resultant films were CISSe. Intermediate peaks between the standard CIS and CISE ascertained the amount of sulfur incorporation. It was established that films produced at

lower selenization temperatures incorporated more sulfur substitutions. This increase in sulfur content held true for films that were etched with acetic acid. Compositional analysis via EDX corroborated selenium loss after post-process etching while non-etched CISSe films maintained an optimal Cu/In ratio of 0.6. Morphology exposed a porous surface of the film after etching displaying a poor quality of the film, causing a decline in electrical connectivity.

As a result of sulfur substitutions in the film, a higher than average band gap energy of 1.17 eV was established. The champion NE CISSe device attained a V_{OC} , I_{SC} , and efficiency of 0.93 V, 3.9 mA/cm² and 2.1%, respectively, whereas the champion E device parameters were diminished to a V_{OC} , I_{SC} , and efficiency of 0.52 V, 3.4 mA/cm² and 0.88% respectively. The range of device efficiencies is lower than that of average laboratory devices due to variations in deposition techniques. The increase in porosity of the films also contributed to degradation of the back contact and reduction in series resistance which lowered the efficiency. The range of V_{OC} and efficiencies for both NE and E CISSe devices is however narrower than that of the materials discussed in earlier chapters. This advocates for higher reproducibility thus, further enhancements should focus on reducing interactions with the back contact and improving the homogeneity of the film to reduce series resistance in the device.

4.5 References

1. Green, M. A.; Dunlop, E. D.; Hohl-Ebinger, J.; Yoshita, M.; Kopidakis, N.; Hao, X., Solar Cell Efficiency Tables (Version 56), *Prog. Photovolt.*, **2020**, 28, 629-638.
2. Adurodija, F.; Carter, M. J.; Hill, R., Novel Method of Synthesizing P-CuInSe₂ Thin Films from the Stacked Elemental Layers Using a Closed Graphite Box, *IEEE Photovoltaic Specialists Conference (PVSC)*, **1995**, 1, 186-189
3. Rohom, A. B.; Londhe, P. U.; Bhand, G. R.; Lakhe, M. G.; Chaure, N. B., Study of Electrochemically Grown Copper Indium Diselenide (CIS) Thin Films for Photovoltaic Applications, *J. Mater. Sci.: Mater. Electron.*, **2016**, 27, 12374-12384.
4. Rohom, A. B.; Londhe, P. U.; Chaure, N. B., The Effect of Citric Acid and Selenization onto Electrochemically Deposited Copper-Indium Thin Films for Solar Cell Applications, *Thin Solid Films*, **2017**, 642, 303-310.
5. Lopez-Garcia, J.; Xie, H.; Sylla, D.; Fontané, X.; Blanes-Guardia, M.; Ramos, F.; Espindola, M.; López-Marino, S.; Izquierdo-Roca, V.; Saucedo, E.; Pérez-Rodríguez, A., Influence of the

Sulfurization-Selenization Process on $\text{CuIn}(\text{S},\text{Se})_2$ Thin Film Solar Cells from Screen Printing of Oxide Nanoparticle Based Inks, *Mater. Chem. Phys.*, **2013**, *160*, 237-243.

6. Uhl, A.; Katahara, J.; Hillhouse, H., Molecular-Ink Route to 13.0% Efficient Low-Bandgap $\text{CuIn}(\text{S},\text{Se})_2$ and 14.7% Efficient $\text{Cu}(\text{In},\text{Ga})(\text{S},\text{Se})_2$ Solar Cells, *Energy Environ. Sci.*, **2015**, *9*, 130-134.

7. Clark, J. A.; Murray, A.; Lee, J.-m.; Autrey, T. S.; Collord, A. D.; Hillhouse, H. W., Complexation Chemistry in N,N-Dimethylformamide-Based Molecular Inks for Chalcogenide Semiconductors and Photovoltaic Devices, *J. Am. Chem. Soc.*, **2019**, *141*, 298-308.

8. Haddad, Y.; Satour, F.; Bouima, H.; Hassam, A.; Zouaoui, A.; Zegadi, A., A Study on the Electrochemical Synthesis and Characterization of CuInSe_2 Thin Films on Mo and Si Substrates, *Arab. J. Sci. Eng.*, **2020**, 1-8.

9. Cheng, Y.-S.; Wang, N.-F.; Tsai, Y.-Z.; Lin, J.-J.; Houng, M.-P., Investigation of CuInSe_2 Nanowire Arrays with Core-Shell Structure Electrodeposited at Various Duty Cycles into Anodic Alumina Templates, *Appl. Surf. Sci.*, **2017**, *396*, 631-636.

10. Li, W.; Wang, M.; Pan, Y.; Han, L.; Lai, Y.; Jiang, Y.; jiang, L.; Zhang, K.; Liu, F., Effect of Sulfurization Temperature on the Properties of $\text{CuIn}(\text{S},\text{Se})_2$ Thin Films Fabricated from Electrodeposited CuInSe_2 Precursors, *Superlattices Microstruct.*, **2018**, *122*, 614-623.

11. Londhe, P. U.; Rohom, A. B.; Chaure, N. B., CuInSe_2 Thin Film Solar Cells Prepared by Low-Cost Electrodeposition Techniques from a Non-Aqueous Bath, *RSC Adv.*, **2015**, *5*, 89635-89643.

12. Ye, H.; Park, H. S.; Akhavan, V. A.; Goodfellow, B. W.; Panthani, M. G.; Korgel, B. A.; Bard, A. J., Photoelectrochemical Characterization of CuInSe_2 and $\text{Cu}(\text{In}_{1-x}\text{Ga}_x)\text{Se}_2$ Thin Films for Solar Cells, *J. Phys. Chem. C*, **2011**, *115*, 234-240.

13. Tapley, A.; Vaccarello, D.; Hedges, J.; Jia, F.; Love, D. A.; Ding, Z., Preparation and Characterization of CuInS_2 Nanocrystals for Photovoltaic Materials, *Phys. Chem. Chem. Phys.*, **2013**, *15*, 1431-1436.

14. Tapley, A.; Hart, C.; Vaccarello, D.; Love, D. A.; Ding, Z., Effect of Annealing on the Photoelectrochemical Behavior of CuInS_2 Nanocrystal Films, *J. Electrochem. Soc.*, **2014**, *161*, H725-H729.

15. Tapley, A.; Liu, L.; Cui, X.; Zuin, L.; Love, D. A.; Zhou, J.; Sham, T.-K.; Ding, Z., Assessing the Band Structure of CuInS_2 Nanocrystals and Their Bonding with the Capping Ligand, *J. Phys. Chem. C*, **2015**, *119*, 20967-20974.

16. Tapley, A. R. Fabrication and Characterization of CuInS_2 and CuInSe_2 Light-Absorbing Thin Films for Use in Solar Cells. University of Western Ontario, Electronic Thesis and Dissertation Repository, 2017.

17. Turnbull, M. J. Layer-by-Layer Construction Strategies toward Efficient CZTS Solar Cells. University of Western Ontario, Electronic Thesis and Dissertation Repository, 2018.

18. Momma, K.; Izumi, F., Vesta 3 for Three-Dimensional Visualization of Crystal, Volumetric and Morphology Data, *J. Appl. Crystallogr.*, **2011**, *44*, 1272-1276.

19. Riha, S. C.; Fredrick, S. J.; Sambur, J. B.; Liu, Y.; Prieto, A. L.; Parkinson, B. A., Photoelectrochemical Characterization of Nanocrystalline Thin-Film $\text{Cu}_2\text{ZnSnS}_4$ Photocathodes, *ACS Appl. Mater. Int.*, **2011**, *3*, 58-66.
20. Esmaeili-Zare, M.; Behpour, M., Influence of Deposition Parameters on Surface Morphology and Application of CuInS_2 Thin Films in Solar Cell and Photocatalysis, *Int. J. Hydrogen Energy*, **2020**, *45*, 16169-16182.
21. Yeranyan, N. S.; Petrosyan, S.; Musayelyan, A. S.; Arutiunyan, L.; Avdjyan, K., Investigation of the Impact of the Selenization Temperature on Parameters of CIS Thin Films, *Armen. J. Phys.*, **2017**, *10*, 1-8.
22. Bhattacharyya, D.; Forbes, I.; Adurodija, F.; Carter, M., Formation of CuInSe_2 by the Selenization of Sputtered Cu/In Layers, *J. Mater. Sci.*, **1997**, *32*, 1889-1894.
23. Vaccarello, D. Fabricating and Characterizing Chalcogenide Thin Films as Light Absorbing Layers in Solar Cells University of Western Ontario, Electronic Thesis and Dissertation Repository, 2016.
24. Colombara, D.; Elanzeery, H.; Nicoara, N.; Sharma, D.; Claro, M.; Schwarz, T.; Koprek, A.; Wolter, M. H.; Melchiorre, M.; Sood, M.; Valle, N.; Bondarchuk, O.; Babbe, F.; Spindler, C.; Cojocaru-Miredin, O.; Raabe, D.; Dale, P. J.; Sadewasser, S.; Siebentritt, S., Chemical Instability at Chalcogenide Surfaces Impacts Chalcopyrite Devices Well Beyond the Surface, *Nat. Commun.*, **2020**, *11*, 1-14.
25. Saber, S.; Mollar, M.; Elnahrawy, A.; Khattab, N.; Eid, A.; Aboaly, M.; Marí Soucase, B., Annealing Study of Electrodeposited CuInSe_2 and CuInS_2 Thin Films, *Opt. Quantum Electron.*, **2018**, *50*, 1-13.
26. Manallah, K.; Satour, F.; Zouaoui, A.; Zegadi, A., Structural, Sem and Nucleation Characterization of Electrochemically Synthesized CuInSe_2 Thin Films, *J. Electron. Mater.*, **2020**, *49*, 3956-3963.
27. Bouima, H.; Zegadi, A.; Satour, F.; Zouaoui, A.; Hassam, A., $\text{CuIn}(\text{Se},\text{S})_2$ Thin Films Synthesis and Characterization from a Single-Bath Electrodeposition Method, *J. Electron. Mater.*, **2019**, *48*, 4099-4106.
28. Hashemi, M.; Ghorashi, S. M. B.; Tajabadi, F.; Taghavinia, N., Investigation of Precursors Concentration in Spray Solution on the Optoelectronic Properties of CuInSe_2 Thin Films Deposited by Spray Pyrolysis Method, *J. Mater. Sci.: Mater. Electron.*, **2020**, 1-10.
29. Khavari, F.; Keller, J.; Larsen, J. K.; Sopiha, K. V.; Törndahl, T.; Edoff, M., Comparison of Sulfur Incorporation into CuInSe_2 and CuGaSe_2 Thin-Film Solar Absorbers, *Phys. Status Solidi A*, **2020**, *217*, 1-12.
30. Houck, D. W.; Assaf, E. I.; Shin, H.; Greene, R. M.; Pernik, D. R.; Korgel, B. A., Pervasive Cation Vacancies and Antisite Defects in Copper Indium Diselenide (CuInSe_2) Nanocrystals, *J. Phys. Chem. C*, **2019**, *123*, 9544-9551.

31. Salomé, P. M. P.; Malaquias, J.; Fernandes, P. A.; Ferreira, M. S.; da Cunha, A. F.; Leitão, J. P.; González, J. C.; Matinaga, F. M., Growth and Characterization of $\text{Cu}_2\text{ZnSn}(\text{S},\text{Se})_4$ Thin Films for Solar Cells, *Sol. Energy Mater. Sol. Cells*, **2012**, *101*, 147-153.
32. Henry, J.; Mohanraj, K.; Sivakumar, G., XRD, AFM, DRS and Photosensitivity of CZTSe Thin Films Prepared by Vacuum Evaporation Method, *Iran. J. Sci. Technol. Trans. A. Sci.*, **2019**, *43*, 1535-1544.
33. Saidi, H.; Boujmil, M. F.; Durand, B.; Bouaïcha, M., Physical Properties of Highly Crystalline CIS Layer Prepared Using Single Phase Electrodeposition and Low Temperature RTP Annealing, *J. Alloys Compd.*, **2017**, *695*, 779-786.
34. Bhatia, A.; Karmarkar, M. A.; Meadows, H.; Hymas, M.; Smith, E. M.; Dale, P.; Scarpulla, M., Effects of Annealing in Sulfur Vapor on Electrodeposited CuInSe_2 Films, *IEEE Photovoltaic Specialists Conference (PVSC)*, **2012**, 000879-000883.
35. Harvey, S. M.; Houck, D. W.; Kirschner, M. S.; Flanders, N. C.; Brumberg, A.; Leonard, A. A.; Watkins, N. E.; Chen, L. X.; Dichtel, W. R.; Zhang, X.; Korgel, B. A.; Wasielewski, M. R.; Schaller, R. D., Transient Lattice Response Upon Photoexcitation in CuInSe_2 Nanocrystals with Organic or Inorganic Surface Passivation, *ACS Nano*, **2020**, *14*, 13548-13556.
36. Jiang, J.; Giridharagopal, R.; Jedlicka, E.; Sun, K.; Yu, S.; Wu, S.; Gong, Y.; Yan, W.; Ginger, D. S.; Green, M. A.; Hao, X.; Huang, W.; Xin, H., Highly Efficient Copper-Rich Chalcopyrite Solar Cells from DMF Molecular Solution, *Nano Energy*, **2020**, *69*, 104438 - 104449.
37. Stanbery, B. J., Copper Indium Selenides and Related Materials for Photovoltaic Devices, *Crit. Rev. Solid State Mater. Sci.*, **2002**, *27*, 73-117.
38. Madelung, O., I-III-VI₂ Compounds. In *Semiconductors: Data Handbook*, 3rd ed.; Springer Berlin Heidelberg: 2004; pp 289-328.
39. Lai, Y.; Kuang, S.; Liu, F.; Yuan, Z.; Zhang, Z.; Li, Y.; Liu, J.; Wang, B.; Tang, D.; Li, J.; Liu, Y., Effects of Cu/In Ratio of Electrodeposited Precursor on Post-Sulfurization Process in Fabricating Quaternary $\text{CuIn}(\text{S},\text{Se})_2$ Thin Films, *Appl. Surf. Sci.*, **2011**, *257*, 8360-8365.
40. Yang, J.; Jae-Yup, K.; Yu, J.; Ahn, T.-Y.; Lee, H.; Choi, T.-S.; Kim, Y.-W.; Joo, J.; Ko, M.; Hyeon, T., Copper-Indium-Selenide Quantum Dot-Sensitized Solar Cells, *Phys. Chem. Chem. Phys.*, **2013**, *15*, 20517-20525.
41. Peng, X.; Zhao, M.; Zhuang, D.; Sun, R.; Zhang, L.; Wei, Y.; Lv, X.; Wu, Y.; Ren, G., Study on How the Content of Selenium in the Precursors Influences the Properties of CuInSe_2 Thin Films, *Appl. Surf. Sci.*, **2018**, *434*, 452-455.
42. Saifullah, M.; Gwak, J.; Park, J. H.; Ahn, S.; Kim, K.; Eo, Y. J.; Yun, J. H., Effect of Substrate Temperature During the Three-Stage Process on the CuInSe_2 Solar Cell Characteristics, *Curr. Appl. Phys.*, **2017**, *17*, 1194-1201.
43. Li, H.; Li, W.; Li, W.; Chen, M.; Snyders, R.; Bittencourt, C.; Yuan, Z., Engineering Crystal Phase of Polytypic CuInS_2 Nanosheets for Enhanced Photocatalytic and Photoelectrochemical Performance, *Nano Res.*, **2020**, *13*, 583-590.

44. Félix, R.; Weber, A.; Zander, O.; Rodriguez-Álvarez, H.; Schubert, B.-A.; Klaer, J.; Wilks, R. G.; Schock, H.-W.; Mainz, R.; Bär, M., Selenization of CuInS₂ by Rapid Thermal Processing – an Alternative Approach to Induce a Band Gap Grading in Chalcopyrite Thin-Film Solar Cell Absorbers?, *J. Mater. Chem. A*, **2019**, *7*, 2087-2094.
45. Shi, J.-B.; Chen, Y.-C.; Chen, C.-J.; Wu, P.-F., Optical Properties and Synthesis of CuInSe₂ Thin Films by Selenization of Cu/In Layers, *Cryst. Res. Technol.*, **2012**, *47*, 183-186.
46. Wu, S.; Jiang, J.; Yu, S.; Gong, Y.; Yan, W.; Xin, H.; Huang, W., Over 12% Efficient Low-Bandgap CuIn(S,Se)₂ Solar Cells with the Absorber Processed from Aqueous Metal Complexes Solution in Air, *Nano Energy*, **2019**, *62*, 818-822.
47. Yamada, A.; Matsubara, K.; Sakurai, K.; Ishizuka, S.; Tampono, H.; Fons, P. J.; Iwata, K.; Niki, S., Effect of Band Offset on the Open Circuit Voltage of Heterojunction CuIn_{1-x}Ga_xSe₂ Solar Cells, *Appl. Phys. Lett.*, **2004**, *85*, 5607-5609.
48. Mandati, S.; Misra, P.; Boosagulla, D.; Rao, T. N.; Sarada, B. V., Economic Pulse Electrodeposition for Flexible CuInSe₂ Solar Cells, *Mater. Renew. Sustain. Energy*, **2020**, *9*, 1-6.
49. Lee, S.; Ikeda, S.; Yagi, T.; Harada, T.; Ennaoui, A.; Matsumura, M., Fabrication of CuInS₂ Films from Electrodeposited Cu/In Bilayers: Effects of Preheat Treatment on Their Structural, Photoelectrochemical and Solar Cell Properties, *Phys. Chem. Chem. Phys.*, **2011**, *13*, 6662-6669.
50. Tiwari, D.; Koehler, T.; Lin, X.; Sarua, A.; Harniman, R.; Wang, L.; Klenk, R.; Fermin, D. J., Single Molecular Precursor Solution for CuIn(S,Se)₂ Thin Films Photovoltaic Cells: Structure and Device Characteristics, *ACS Appl. Mater. Interfaces*, **2017**, *9*, 2301-2308.
51. Jeong, C.; Kim, J. H., Fabrication of CuInSe₂ Thin Film Solar Cell with Selenization of Double Layered Precursors from Cu₂Se and In₂Se₃ Binary, *Thin Solid Films*, **2014**, *550*, 660-664.
52. Chandran, R.; Behera, A. K.; Mallik, A., An Attempt to Co-Deposit Photovoltaic Quality CuInSe₂ Thin Films: Effect of Surfactant and Deposition Potential, *J. Mater. Sci.: Mater. Electron.*, **2019**, *30*, 15460-15468.
53. Saha, S.; Johnson, M.; Altayaran, F.; Wang, Y.; Wang, D.; Zhang, Q., Electrodeposition Fabrication of Chalcogenide Thin Films for Photovoltaic Applications, *Electrochem.*, **2020**, *1*, 286-321.

Chapter 5

5 Concluding remarks and future work

5.1 Concluding remarks

The objectives of my thesis have been to determine the most remunerative deal for thin-film solar cells from three chalcogenide materials: CZTS, CZTSSe and CISSe, as the light-absorption and conversion layers. They were investigated throughout this thesis as they all show to be promising candidates for use in solar cells. My research focused on fabricating the light-absorbing films using two distinct low-cost methods: 1. electrochemical deposition of metallic layers followed by a sulfurization/selenization process and 2. nanocrystal synthesis and electrophoretic deposition. The photocurrent produced in photoelectrochemical measurements (PECMs) was employed as a quantitative measure of the film quality. Utilizing this technique, each material was optimized to produce the greatest amount of photocurrent toward the most efficient final device.

Chapter 2 investigates the p-n heterojunction of an efficient solar device employing CZTS nanocrystals for the light-absorber-layer. Fabrication involved solvothermal synthesis of CZTS nanocrystals along with post-process etching with acetic acid. By means of PECMs, the film produced the most photoresponse after post-process etching and the addition of the CdS buffer layer as hypothesized. Altered crystal structures due to the etching procedure was examined via XAFS, which displayed an increase in *p*-type character and decrease in porosity in the nanocrystals after etching, leading to higher efficiencies. The barrier at the p-n heterojunction was determined using band gap and valence band energy values determined from UV-VIS and SR-XPS.

Both spike-like and cliff-like barriers were possible, with the former valuable to efficient current flow and prevention of current loss. For both scenarios of etched and non-etched nanocrystals, a spike-like barrier was determined deeming beneficial use of nanocrystals for the absorber layer. The etched device attained a higher device efficiency and open circuit potential of 6.5% and 0.85 V, respectively. Chapter 2 also touched on the

development of CZTS by electrodeposition (ED) of stacked metallic layers. Preliminary results of an ED CZTS layer yielded low photoresponse and required further optimization.

This led into the motivation for Chapter 3 where electrodeposition alongside selenization was used to create a CZTSSe film as selenium proved to increase photocurrent. Optimization of the selenization conditions lead to the highest photoresponse produced by a film fabricated at 500 °C with 5 mg/cm² of selenium. In contrast to the previous chapter, photoresponse decreased upon etching of the absorber layer. PECMs also displayed an increase in photoresponse when the CdS buffer layer was added. Upon composition analysis, it was determined that sulfur substitutions occurred due to contamination and that the etching process removed selenium residing on the surface. Both facts led to an increase in sulfur and in turn a decrease in photoresponse when the film was etched. Surface morphology of the CZTSSe layer before and after etching gave insight into another basis for poor performance. After post-process etching, the porosity in the film increased which resulted in a rise of recombination sites and inefficient charge flow throughout the film. As hypothesized from the PECMs, the non-etched device attained the higher efficiency and open-circuit potential of 5.3% and 0.97 V, respectively.

Considering selenium enhanced photocurrent, the same rationale was applied in Chapter 4 where the performance of CISSe devices were investigated. The CISSe film was fabricated by electrodeposition of a Cu/In bilayer followed by high temperature selenization. Electrodeposition parameters were kept constant however selenization parameters were modified to achieve highest photocurrent without indium losses. PECMs concluded that a film fabricated at 500 °C with 5 mg/cm² of selenium produced the highest photocurrent. Similar to Chapter 3, post-process etching with acetic acid resulted in a diminished photoresponse yet an increase when the CdS layer was added. X-ray diffractograms revealed sulfur incorporation possibly due to contamination and thus the absorber layer was concluded to be CISSe. At lower temperatures and after etching, more sulfur was present. This argues that the etchant aids in the removal of selenium from the surface, exposing sulfur that penetrated deeper into the film. Surface morphology confirmed this conjecture as etched CISSe films displayed an increase in cracks which drives current loss

throughout the film. As expected, non-etched CISSe devices achieved the higher device efficiency and open circuit potential of 2.1% and 0.93 V, respectively.

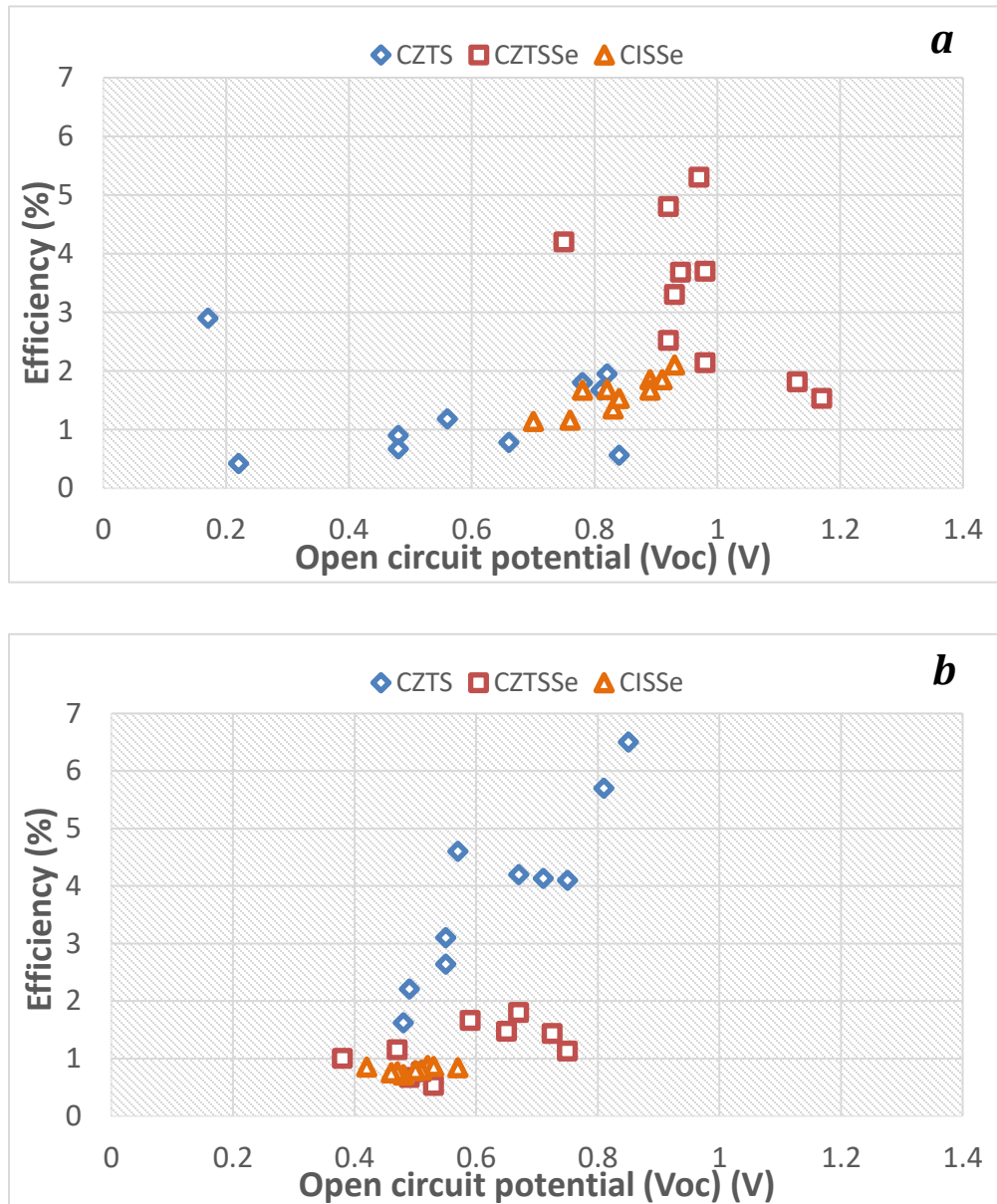


Figure 5.1: Range of device efficiencies of CZTS, CZTSSe and CISSe as a function of open-circuit potential in a) ten non-etched devices and b) ten etched devices.

The most efficient device using the three chalcogenide materials as the light-absorbing layer was concluded to be the etched CZTS NC one with the least efficient being the etched CISSe device. Figure 5.1 graphically exhibits the range of device efficiencies as a function

of open-circuit potential for all materials in both etched and non-etched cases. When determining the most remunerative deal for solar cells, cost and reproducibility become the greatest influential factors. While CZTS NC devices achieve a higher maximum efficiency, the range across ten devices in both etched and non-etched cases is vast in comparison to the other materials. This wide range in device efficiency demonstrates poor reproducibility for the synthesis and deposition of the nanocrystals. Both film fabrication techniques are low-cost, however electrodeposition is deemed to be the stronger and more reproducible technique for its cost.

Conversely, CISSe devices have the narrowest range for efficiency in both etched and non-etched cases yet the maximum efficiency is much lower than its CZTS and CZTSSe counterparts. In addition, indium is more expensive than other elements used. Thus, the CISSe film should have been within or above the range of laboratory efficiencies to justify the cost. The narrow range of efficiency does advocate for the reproducibility of the film however many improvements must be made to upkeep the promise of being a highly efficient material. Finally, the scope of CZTSSe devices separates that of the other two materials. The range of device efficiencies and open circuit potentials is narrower than that of the nanocrystals which endorses the reproducibility of the film. Furthermore, the reach of efficiency is higher than that of CISSe as the maximum obtained was 5.3%, showing promise. In addition, the CZTSSe film utilizes cheaper, earth abundant materials.

Considering reproducibility and cost factors, the CZTSSe absorber layer is the most remunerative deal of the three materials for highly efficient solar devices. The electrochemical deposition technique used is also an advantage as it is a low-cost and easily scalable method for future fabrication. Further improvement to this deposition technique is still required as the reduction of secondary phases and porosity have the greatest impact on increasing device performance.

5.2 Future work

Long term goals of solar devices focus on low-cost methods involving environmentally friendly aspects. The electrochemical deposition technique is reproducible and has more promise over a nanocrystal approach. However, the selenization step involves a high-

temperature process which is expensive and harmful to the film surface. Therefore, we should move towards fabricating a light-absorber-layer with all the components electrodeposited as it could lower manufacturing costs even further and yield in more replicable devices. Electrodeposition of thin films is also considered one of the most promising deposition techniques due to the ability to control film thickness. Thus, good future work is to use this technique to incorporate selenium into the film without needing high temperature atmospheres. Many studies have utilized electrodeposition of selenium while analyzing the morphology and formation mechanisms of the selenium deposit.^{1, 2} Following the work of *Dilmi et al.*, selenium deposition on a Mo-coated glass substrate was tried and the resulting photoresponse was investigated.³ The recipe of the selenium plating bath is detailed in their study; however, Mo-coated substrates were not explored in their work and so the deposition parameters were modified.

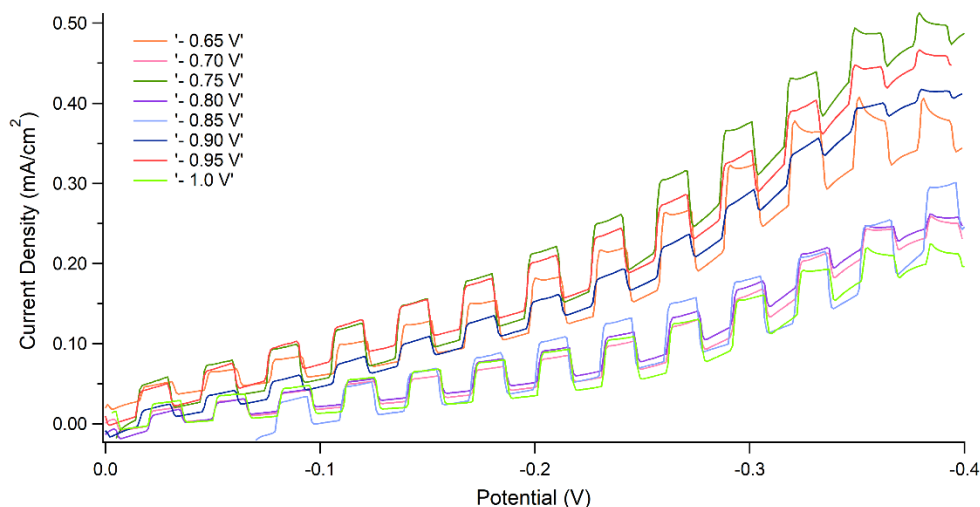


Figure 5.2: PECMs of electrodeposited selenium on Mo-coated glass at various deposition potentials. Each deposition was held for 20 seconds.

Figure 5.2 demonstrates the photoresponse of electrochemically deposited selenium on Mo-coated glass at different deposition potentials. As Mo-coated glass provides no photoresponse under illumination, it is established that the resulting photocurrent is from the selenium. Further research is required into the growth mechanism of the electrochemically deposited selenium on stacked metallic layers and the yielding photoresponse. Nevertheless, these preliminary results show promising grounds for future

elimination of high temperature selenization and towards an entirely electrodeposited light-absorbing layer. The solar industry faces many struggles with the cost of manufacturing solar devices.⁴ Yet the use of electrodeposited CZTSSe, given more improvements, may be effective for low-cost, large scale implementation.

In addition, future research should explore the replacement of the subsequent CdS layer. It is often used in literature and laboratory work for the *n*-type buffer layer. However, to meet environmental concerns, it should be modified or omitted due to its toxicity. Alternative materials to replace CdS include zinc/cadmium hybrids, In₂S₃ and Zn(O,S).^{5, 6, 7} Out of which, Zn(O,S) in recent literature has shown to be beneficial to the overall device efficiency due to its large and tunable E_g in comparison to CdS.^{6, 8} Deposition of the Zn(O,S) buffer layer could be easily done via CBD or an ALD. The ALD technique while precise, requires the use of toxic H₂S and long processing times.⁸ Conversely, the CBD technique is a simple method that is widely used but necessitates more control over the uniformity and thickness of the deposited layer. Nonetheless, alternative buffer layer materials and deposition techniques also need further optimization to produce efficient devices for commercialization.

5.3 References

1. Zein El Abedin, S.; Saad, A. Y.; Farag, H. K.; Borisenko, N.; Liu, Q. X.; Endres, F., Electrodeposition of Selenium, Indium and Copper in an Air- and Water-Stable Ionic Liquid at Variable Temperatures. *Electrochim. Acta* **2007**, *52*, 2746-2754.
2. Aal, A. A.; Voigts, F.; Chakarov, D.; Endres, F., Electrodeposition of Selenium from 1-Butyl-1-Methylpyrrolidinium Trifluoromethylsulfonate. *Electrochim. Acta* **2012**, *59*, 228-236.
3. Dilmi, O.; Benaicha, M., Electrodeposition and Characterization of Red Selenium Thin Film—Effect of the Substrate on the Nucleation Mechanism. *Russ. J. Electrochem.* **2017**, *53*, 140-146.
4. Perez, R.; Zweibel, K.; Hoff, T., Solar Power Generation in the US: Too Expensive, or a Bargain? *Energy Policy*. **2011**, *39*, 7290-7297.
5. Tripathi, S.; Sadanand; Lohia, P.; Dwivedi, D. K., Contribution to Sustainable and Environmental Friendly Non-Toxic CZTS Solar Cell with an Innovative Hybrid Buffer Layer. *Solar Energy* **2020**, *204*, 748-760.
6. Khemiri, N.; Chamekh, S.; Kanzari, M., Properties of Thermally Evaporated CZTS Thin Films and Numerical Simulation of Earth Abundant and Non Toxic CZTS/Zn(S,O) Based Solar Cells. *Solar Energy* **2020**, *207*, 496-502.

7. Yan, C.; Liu, F.; Sun, K.; Song, N.; Stride, J. A.; Zhou, F.; Hao, X.; Green, M., Boosting the Efficiency of Pure Sulfide CZTS Solar Cells Using the In/Cd-Based Hybrid Buffers. *Sol. Energy Mater. Sol. Cells* **2016**, *144*, 700-706.
8. Huang, L.; Li, J.; Wang, S.; Zhong, L.; Xiao, X., Forming an Ultrathin SnS Layer on Cu₂ZnSnS₄ Surface to Achieve Highly Efficient Solar Cells with Zn(O,S) Buffer. *Solar RRL* **2020**, *4*, 1-6.

Curriculum Vitae

Name:	Vaishnavi Raja
Post-secondary Education and Degrees:	<p>University of Toronto Toronto, Ontario, Canada 2014 – 2018 Honours B.Sc.</p> <p>The University of Western Ontario London, Ontario, Canada 2018 – 2020 M.Sc.</p>
Related Work Experience	<p>Teaching Assistant The University of Western Ontario 2018-2020</p>
Volunteer Experience	<p>Volunteer Let's Talk Science – Western University 2018-2020</p>
Conference Contributions: Oral Presentations	<p>Electrochemical Society Research Symposium (2018) London, Ontario, Canada <u>Raja, V.</u>, Turnbull, M.J., Ding, Z. (2018) Photoelectrochemical optimization of $\text{Cu}_2\text{ZnSnS}_4$ (CZTS) Nanocrystals for the construction of low-cost solar devices.</p> <p>7th Georgian Bay International Conference on Bioinorganic Chemistry (2019) Parry Sound, Ontario, Canada <u>Raja, V.</u>, Turnbull, M.J., Ding, Z. (2019) Optimizing $\text{Cu}_2\text{ZnSnS}_4$ Nanocrystals and CdS films for the construction of low-cost, efficient solar cells</p> <p>102nd Canadian Chemistry Conference and Exhibition (2019) Québec City, Quebec, Canada <u>Raja, V.</u>, Turnbull, M.J., Ding, Z. (2019) Optimizing $\text{Cu}_2\text{ZnSnS}_4$ Nanocrystals and CdS films for the construction of low-cost, efficient solar cells</p>